1-1-2015

# Earthen levee slide detection via automated analysis of synthetic aperture radar imagery

Lalitha Dabbiru

Recommended Citation
Dabbiru, Lalitha, "Earthen levee slide detection via automated analysis of synthetic aperture radar imagery" (2015). *Theses and Dissertations*. 1605.
https://scholarsjunction.msstate.edu/td/1605

# Earthen levee slide detection via automated analysis of synthetic aperture radar imagery

By

Lalitha Dabbiru

A Dissertation
Submitted to the Faculty of
Mississippi State University
in Partial Fulfillment of the Requirements
for the Degree of Doctor of Philosophy
in Electrical Engineering
in the Department of Electrical and Computer Engineering

Mississippi State, Mississippi

May 2015

# Earthen levee slide detection via automated analysis of synthetic aperture radar imagery

By

Lalitha Dabbiru

Approved:

Nicolas H. Younan
(Major Professor)

James V. Aanstoos
(Committee Member)

Lori M. Bruce
(Committee Member)

Farshid Vahedifard
(Committee Member)

James E. Fowler
(Graduate Coordinator)

Jason Keith
Interim Dean
Bagley College of Engineering

Name: Lalitha Dabbiru

Date of Degree: May 8, 2015

Institution: Mississippi State University

Major Field: Electrical Engineering

Major Professor: Nicolas H. Younan

Title of Study: Earthen levee slide detection via automated analysis of synthetic aperture radar imagery

Pages in Study: 111

Candidate for Degree of Doctor of Philosophy

The main focus of this research is to detect vulnerabilities on the Mississippi river levees using remotely sensed Synthetic Aperture Radar (SAR) imagery. Unstable slope conditions can lead to slump slides, which weaken the levees and increase the likelihood of failure during floods. On-site inspection of levees is expensive and time-consuming, so there is a need to develop efficient automated techniques based on remote sensing technologies to identify levees that are more vulnerable to failure under flood loading. Synthetic Aperture Radar technology, due to its high spatial resolution and potential soil penetration capability, is a good choice to identify problem areas along the levee so that they can be treated to avoid possible catastrophic failure. This research analyzes the ability of detecting the slump slides on the levee with different frequency bands of SAR data. The two SAR datasets used in this study are: (1) the L-band airborne radar data from NASA JPL's Uninhabited Aerial Vehicle Synthetic Aperture Radar (UAVSAR), and (2) the X-band satellite-based radar data from DLR's TerraSAR-X (TSX). The main contribution of this research is the development of a machine learning framework to 1) provide improved knowledge of the status of the levees, 2) detect anomalies on the levee

sections, and 3) provide early warning of impending levee failures. Polarimetric and textural features have been computed and utilized in the classification tasks to achieve efficient levee characterization. Various approaches of image analysis methods for characterizing levee segments within the study area have been implemented and tested. The RX anomaly detector, a training-free unsupervised classification algorithm, detected the active slump slides on the levee at the time of image acquisition and also flagged some areas as "anomalous", where new slides appeared at a later date. This technique is very fast and does not depend on ground truth information, so these results guide levee managers to investigate the areas shown as anomalies in the classification map. The support vector machine (SVM) supervised learning algorithm with grey level co-occurrence matrix (GLCM) features provided excellent results in identifying slump slides on the levee.

# DEDICATION

I would like to dedicate this research to my father, Ganapathy Rao, and my mother, Janaki Devi, for their relentless support of my pursuance of academic excellence, and my sisters and brother for their continuous encouragement.

# ACKNOWLEDGEMENTS

I would like to thank my advisor Dr. Nicolas H. Younan for providing his valuable guidance and feedback. I would like to express my deepest gratitude to my committee member and my dissertation director Dr. James V. Aanstoos, who not only served as my supervisor but also encouraged me throughout my academic program. I enjoyed working as a member of his research team, and this dissertation could not have been written without his excellent guidance and support. He has been a great mentor with a pleasing personality, and I am indebted to him forever. I would like to thank my committee member Dr. Lori M. Bruce, who has always encouraged me to achieve my goals. I also thank my committee member Dr. Farshid Vahedifard for his valuable suggestions. I thank my project team members for the interesting project discussions and fun-filled field trips we had in these years.

Finally, I would like to thank Geosystems Research Institute (GRI) for providing the computing facilities and NASA and SERRI for providing financial support to conduct this research.

# TABLE OF CONTENTS

CHAPTER

LIST OF TABLES

## LIST OF FIGURES

# CHAPTER I

# INTRODUCTION

## 1.1 Background

Levees are the embankments built along the side of a stream or river channel to prevent flooding of the adjacent land. Major levee systems have been built along the Mississippi River and Sacramento River in the United States. The Mississippi levee system represents one of the largest levee systems in the world, comprising over 3500 miles of levees, extending over 620 miles along the Mississippi, stretching from Cape Girardeau, Missouri to the Mississippi Delta [1] [2]. The levee system is constructed of compacted soil and clay and protects more than 4 million citizens and 33,000 farms from destructive floods [1]. Monitoring the physical condition of levees is vital in order to protect them from flooding. The dynamics of subsurface water events can cause damage on levee structures. The alignment of the levee is usually based on the flood protection requirements [3]. The levee is constructed from borrow pits adjacent to the levee, which produce the fill material that is often heterogeneous. Existing levee assessment systems require manual inspections, which are very expensive and time consuming. Over the last decade, there have been several studies on the use of remote sensing for levee monitoring and assessment.

## 1.2 Causes of Levee Failure

Levees typically are earthen embankments constructed from a variety of materials ranging from cohesive to cohesion-less soils to prevent flooding (Figure 1.1). Man-made levee failures can occur due to overtopping, surface erosion, internal erosion (sand boils), and by slope failures [4] [5]. A schematic representation of levee failures is shown in Figure 1.2. Levee failures can occur by any of these mechanisms due to natural or man-made hazards such as floods, hurricanes, earthquakes or poor maintenance. Changes in channel roughness and addition of structures such as bridges, etc. may significantly alter the channel capacity, which could lead to overtopping of the levee structure. Overtopping of levees is a function of flood height and the elevation that the levee was built to protect from flooding. Seepage through levees occurs due to cracks in the levee or because of coarse grained soil used to construct the levee. Grass or some other mat-like vegetation is planted on the top of the levees so that its erosion will be kept to a minimum. Two types of problems that occur along the levees which can be a precursor to complete failure during a high water event are: slough (or slump) slides which occur due to slope failures and sand boils caused due to internal erosion.

Figure 1.1 Earthen Levee on the banks of Albemarle Lake, MS, a Mississippi River oxbow.

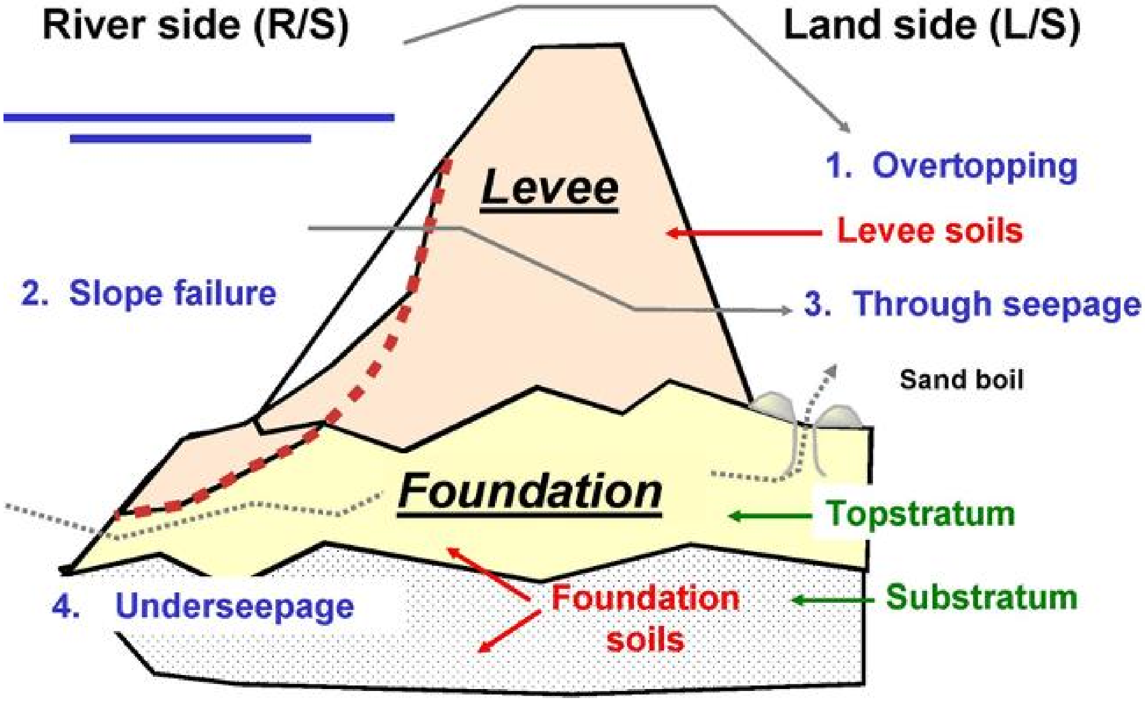

Figure 1.2 A schematic representation of levee failure mechanisms (after Joe Dunbar, 2011)

### 1.2.1 Slough slides

If the underlying foundation materials that support the levee are weak, or become destabilized, a slope failure can develop and result in a catastrophic failure of the levee. These slope failures can form as slough / slump slides along a levee and are vulnerable to levee failure. Usually, the slough slides appear on the river side of the levee and may cause seepage during high water events. The clay soil on the levees shrink during dry weather period and gain moisture during wet season, resulting a loss in shear strength and cause a failure. Figure 1.3 is a photo of a slough slide adjacent to Chotard Lake, MS, taken during one of the field data collection trips.

Figure 1.3 Primary levee failure mechanisms: A slough slide on the levee adjacent to Chotard Lake, MS

### 1.2.2 Sand Boils

Sand boils are springs that form on the land side of a levee containing a river at extremely high flood stage. Hydrostatic pressure generated by the column of river water exerts a downward force that is too great for the wall material of the river channel to contain, and thus water is forced through the wall material of the channel [5] [6]. This underseepage resurfaces on the land side in the form of a cone of sand which may lead to erosion of the levee toe and foundation. Figure 1.4 is a photo of a sand boil in the Eagle Lake area near Vicksburg, MS, taken during one of the field data collection trips. Seepage berms are located adjacent to the landside slope of the levee to reduce the hydraulic pressure of water passing through the sand layers under the levee. Usually, seepage berms are very wide and require tremendous amount of borrow material. So when there is limited landside area, the engineers install relief wells (Figure 1.5) at the levee toe instead of constructing berms to reduce the water pressure. However, the major disadvantage of relief wells is they require periodic maintenance.

Figure 1.4 Primary levee failure mechanisms: Bagged sand boil near Eagle Lake, MS

Figure 1.5 Relief wells installed on the landside of the levee at Francis, MS.

## 1.3 Synthetic Aperture Radar (SAR) for Levee Monitoring

Synthetic Aperture Radar (SAR) is mostly a space-borne or airborne side-looking radar system which utilizes the flight path of the platform to synthesize a long aperture. SAR is the only practical technique to achieve high spatial resolution remote sensing imagery even from space platforms [8]. SAR data has been widely used in disaster management. Polarimetric and interferometric radar data can provide surface and subsidence information for a levee monitoring system [9]. Polarimetric SAR helps classify and quantify ground conditions, while differential SAR interferometry detects small surface displacements over time.

Polarimetric SAR data is very effective for classification as it contains information about different scattering characteristics for each target. Synthetic Aperture Radar technology, due to its high spatial resolution and potential soil penetration capability, is a good choice to identify problem areas on earthen levees so that they can be treated to avoid possible catastrophic failure. The radar backscatter data is capable of identifying variations in soil properties of the areas that might cause levee failure. This research is mainly focused on analyzing different algorithms to assess the condition of levee structure using multi-polarized SAR images.

## 1.4 Motivation

Over the entire US, there are over 100,000 miles of dam and levee structures of varying designs and conditions [3]. Currently, there are limited processes to monitor these structures and predict potential risk to communities. Dam and levee failures can cause catastrophic damage and loss of life. Levee breach is a common levee failure mechanism caused either by surface erosion or subsurface weakness or under-seepage.

The catastrophe caused by hurricane Katrina in 2005 emphasizes the importance of examination of levees to improve the condition of those that are prone to failure during floods. On-site inspection of levees is costly and time-consuming, so there is a need to develop efficient techniques based on remote sensing technologies to identify levees that are more vulnerable to failure under flood loading. Techniques using remote sensing imagery to detect problem areas on the levee will assist levee managers to prioritize their tasks to inspect, test and repair them in a timely manner to avoid complete failures.

## 1.5 Contributions

The main contribution of this research is the development of a machine learning framework to 1) provide improved knowledge of the status of the levees, 2) detect anomalies on the levee sections, and 3) provide early warning of impending levee failures.

The tasks to meet this objective include:

(a) Design and implement experiments using airborne and satellite-based radar imagery to detect anomalies on the levee;

(b) Collect ground truth data and take in-situ measurements at various slump slide and healthy locations on the levee: create polygons at various healthy and slide areas on the levee with a GPS instrument, and use them as training masks in the classification tasks;

(c) Analyze polarimetric and textural features of the image which include:

  1) per-pixel features such as radar backscatter intensities from each polarization channel (HH, HV, and VV)

    2) Computation of polarimetric decomposition features such as entropy, anisotropy, and scattering angle
    3) Derivation of textural features, which include features based on the wavelet transformation and grey level co-occurrence matrix

(d) Develop and compare various machine learning algorithms to classify the SAR imagery for detecting the anomalies on the levees

This contribution will enable the development of a new model for levee slide detection through automated analysis of synthetic aperture radar imagery supplemented by this cost effective method of monitoring a levee system.

## 1.6 References

1. United States Army Corps of Engineers, Mississippi River and Tributaries Project, Levee system evaluation report for the national flood insurance program, April, 2014. http://www.mvd.usace.army.mil/Portals/52/docs/MRC/LeveeSystem/MRT_levee_system_eval_report_for_NFIP.pdf

2. Andrew Flor, Nicholas Pinter, Jonathan W.F. Remo, “Evaluating levee failure susceptibility on the Mississippi River using logistic regression analysis”, Elsevier, Engineering Geology, 2010.

3. United States Army Corps of Engineers, “Design and construction of levees”, EM 1110-2-1913, April 2000.

4. Corps of Engineers Water Resources Infrastructure, National Research Council, National Academies Press, ISBN 978-0-309-26476-1, 2012.

5. J. Dunbar, “The use of airborne geophysics for levee classification and assessment”, 2011.

6. Williams, J. G., “Sand boils: A modern analogue of ancient sand volcanos,” Arkansas Academy of Science Proceedings, vol. XXVI11, pp. 80–81, 1974.

7. Thomas F. Wolff, “Performance of levee underseepage controls: A critical review,” final report, 2002.

8. Y.K. Chan and V.C. Koo, “An introduction to synthetic aperture radar (SAR)”, Progress in Electromagnetics Research B, Vol. 2, 27 – 60, 2008.

9. Cathleen E. Jones, Gerald Bawden, Steven Deverel, Joel Dudas, Scott Hensley, Sang-Ho Yun, Study of movement and seepage along levees using DINSAR and the airborne UAVSAR instrument, , Proc. SPIE 8536, SAR Image Analysis Modeling, and Techniques XII, 85360E, November 2012.

# CHAPTER II

# LITERATURE REVIEW

## 2.1 Synthetic Aperture Radar Data (SAR) Applications

SAR data has been widely used in disaster management. Polarimetric and interferometric radar data can provide surface and subsidence information for a levee monitoring system. Polarimetric SAR helps classify and quantify ground conditions, while differential SAR interferometry detects small surface displacements over time. The polarimetric SAR data is very effective for classification as it contains different scattering characteristics for each target and hence contributes changes in the backscatter signal. Interferometric SAR (InSAR) is useful for measuring ground movements using the phase content of the radar signal.

Remote sensing studies in the last decade have largely focused on detection of deformation, slides, and seepage on levees and dikes. Synthetic aperture radar data has been investigated and widely used for deformation detection on levees and dykes. The German TerraSAR-X satellite and the Canadian RADARSAT satellite have been used to monitor and detect levee movements and subsidence associated with levee failures [1]. High resolution UAVSAR data has been used to detect deformation of the levees, subsidence along the levee toe, and seepage through the levees in California’s Sacramento-San Joaquin Delta by making use of polarimetric and interferometric SAR techniques [2]. Airborne UAVSAR and satellite-based TerraSAR-X polarimetric SAR imagery have been used for levee slide detection to aid the levee screening process [3] [4] [5] 6]. The type of vegetation that grows in a slide area differs from the surrounding levee vegetation, which can also be utilized in detecting slides [7]. Inspection of grass-covered dykes with remote sensing imagery obtained using hand-held sensors has been conducted with soil moisture and quality of the dyke cover as the two important criteria [8].

Radar polarization and incidence angle are important factors that affect the radar backscatter [9]. The radar backscatter is strong for lower incidence angles and decreases with increasing incidence angles. Also, the radar backscatter is influenced by the frequency of the radar wave and the penetration depths of different radar bands vary with its wavelengths; the longer the wavelength, the greater the penetration depth. A short wavelength (3 cm) is scattered by small objects on Earth, for example tree leaves. Lau's research focuses on using three different SAR imagery; ALOS PALSAR L-band, RADARSAT-1 C-band, and the TerraSAR-X X-band data and compared their performances in Earthquake damage assessment [10]. Battsengel et al. have used multi-frequency radar images for the classification of different urban land surface features [11]. The performance evaluation of levee anomaly detection using UAVSAR L-band and TerraSAR –X X-band SAR data was investigated and the results showed higher classification accuracies with L-band data compared to the X-band data [12] [13]. SAR data can also be used to delineate oil slicks which cause marine pollution. The high resolution, low-noise UAVSAR L-band data was used in the detection, migration, and impact of oil from the Deepwater Horizon oil spill [14] [15].

## 2.2 SAR Data - Machine Learning

In SAR images, texture and intensity are the two important parameters for the classification tasks. Statistical texture analysis is very important in SAR imagery since it allows better representation and segmentation of various objects on the levee. The radar Backscatter is affected by soil moisture, vegetation density, and surface roughness.

The discrete wavelet transform is a promising tool for texture analysis because it has the ability to examine the data at different scales [16]. Fukuda et al. applied the texture feature set derived from the wavelet decomposition to the classification of multi-frequency polarimetric NASA/JPL AIRSAR imagery [17]. Discrete wavelet transform feature extraction has been used for dimensionality reduction of hyperspectral data and various wavelet-based features were applied to the problem of automatic classification of ground vegetation from hyperspectral signatures [18]. The ability of wavelet analysis to decompose the image into different frequency sub-bands makes it suitable for image classification. The dependence between features from different sub-bands have been investigated and showed that dependence among features are effective for sub-band selection and achieved lower classification error rates with smaller number of sub-bands [19].

Grey level co-occurrence matrix (GLCM) features have been a popular method for textural extraction in remotely sensed images [20] [21]. Cui et al. [22] have implemented a multi-classifier decision fusion framework for levee health monitoring using texture features derived from the grey level co-occurrence matrix. Levee slump slide detection was performed by Omni-directional GLCM texture analysis which has been conducted on the re-sampled images using Rubber Band Straightening Transform

(RBST) and Spiral Straightening Transform (SST) [23]. GLCM textural features extracted from the ERS-1 synthetic radar imagery have been used to map sea ice texture [24].

Several supervised and unsupervised classification algorithms have been applied to SAR data for efficient land cover classification [25] [26]. Polarimetric decomposition parameters entropy (H), anisotropy (A), and alpha (α) derived from the coherency matrix calculated from the SAR data have been used to detect anomalies such as slough slides along the levee [27]. Melamed et al. [28] applied the Silverman-Totman-Caefer (SRC) algorithm and a classification algorithm by Cloud and Pottier [29] to polarimetric SAR data to detect anomalies. Texture classifying neural network algorithm can be applied to detect oil spills from Synthetic Aperture Radar (SAR) imagery [30]. Neural networks have been applied to the classification of polarimetric SAR data using features extracted from the Freeman decomposition model [31] and Cloud decomposition model [32] [33]. Ince et al. [34] proposed radial basis function (RBF) based classifier with entropy/alpha/anisotropy (H/α/A) decomposition features and GLCM texture features and stated that the overall classification performance has been significantly improved with RBF classifier. Chen et al. have used polarimetric classification algorithms for agricultural crop identification and achieved better accuracies by applying the coherency matrix features to the Wishart maximum likelihood (WML) classification method [35].

Recently anomaly detection algorithms have become an important application for target detection. These unsupervised classification techniques are very fast and do not depend on ground truth information. Reed and Yu developed a method referred to as the RX detector [36] which has shown success in anomaly detection of multispectral and hyperspectral data [37]. The SRC and RX algorithms were compared for detecting anomalous pixels in the hyperspectral imagery and stated that on average the SRC algorithm takes 1.3 times the amount of time the RX algorithm does [38]. Baghbidi et al. implemented anomaly detection algorithms on hyperspectral data using wavelet features as a pre-processing data reduction step [39]. The RX anomaly detection algorithm was implemented to detect anomalies on the Mississippi river levees and the classifier's output was further investigated by comparing with the in-situ soil properties like soil texture, moisture content, hydraulic conductivity, and penetration resistance [40].

Several supervised classification techniques have been used for the classification of polarimetric synthetic aperture radar data. The support vector machine (SVM) is a powerful supervised learning method for analyzing and recognizing patterns. It is a state-of-the-art classification method introduced by Vapnik [41]. SVM, a nonparametric classification method, has been used successfully in remote sensing studies [42]. Zhang et al. [43] implemented the SVM algorithm for the classification of polarimetric SAR images using scattering and textural features. Automatic classification of multi-temporal ERS-1 SAR images using radial basis function neural network classifier has been implemented for classifying different land-cover classes and achieved high accuracies [44]. A multilayer feed-forward neural network classifier with statistical features was applied to multi-temporal RADARSAT imagery for extracting landuse / landcover information and the results demonstrated better classification performance with a neural network classifier compared to the maximum likelihood classifier (MLC) [45].

## 2.3 SAR Data for Soil Moisture estimation

The estimation of soil moisture using synthetic aperture radar data has been studied by many researchers. Many empirical models for soil moisture estimation were developed for soils with no vegetation cover [46] [47] [48]. Oh et al. [46] developed an inversion technique to obtain surface roughness and dielectric constant from the co-polarization ratio p and the cross-polarization ratio q. However, the presence of vegetation changes the backscatter magnitudes and the estimation of soil moisture would be more complex. The model works over limited ranges of roughness and moisture. The co-polarization and cross-polarization ratios are defined as:

$$p = \sigma_{hh}^{0}/\sigma_{vv}^{0} \tag{2.1}$$

$$q = \sigma_{hv}^{0}/\sigma_{vv}^{0} \tag{2.2}$$

where $\sigma_{hh}^{0}$ is the HH polarized backscatter coefficient, $\sigma_{vv}^{0}$ is the VV polarized backscatter coefficient, and $\sigma_{hv}^{0}$ is the HV polarized backscatter coefficient. The dielectric constant is obtained by the following empirical equations: [16]

$$\left(\frac{2\theta}{\pi}\right)^{1/3\Gamma_0} . \left[1 - \frac{q}{0.23\sqrt{\Gamma_0}}\right] + \sqrt{p} - 1 = 0 \tag{2.3}$$

$$\Gamma_0 = \left|\frac{1-\sqrt{\varepsilon_r}}{1+\sqrt{\varepsilon_r}}\right|^2 \tag{2.4}$$

where θ is the incidence angle in radians, $\Gamma_0$ is the Fresnel reflectivity of the surface at nadir, and $\varepsilon_r$ is the real part of dialectic constant and the imaginary part is ignored.

## 2.4 Interferometric SAR (InSAR) for deformation measurement applications

Radar interferometry is an imagining technique for measuring topography changes of the Earth's surface over time. In this technique, SAR data was acquired from the same location at two different times. If there is no topography change, then the phase of the second-pass radar signals would be the same as that of the first-pass signal. Interferometric maps are generated by subtracting the phase value from one SAR data acquisition to that of the other, for the same point on the ground (Figure 2.1). The resulting phase difference is represented by interferometric fringes, which is directly related to the topographic height. A time-series of N single look complex (SLC) SAR images will be used to generate ground deformation fields and interpretation maps in the study area.

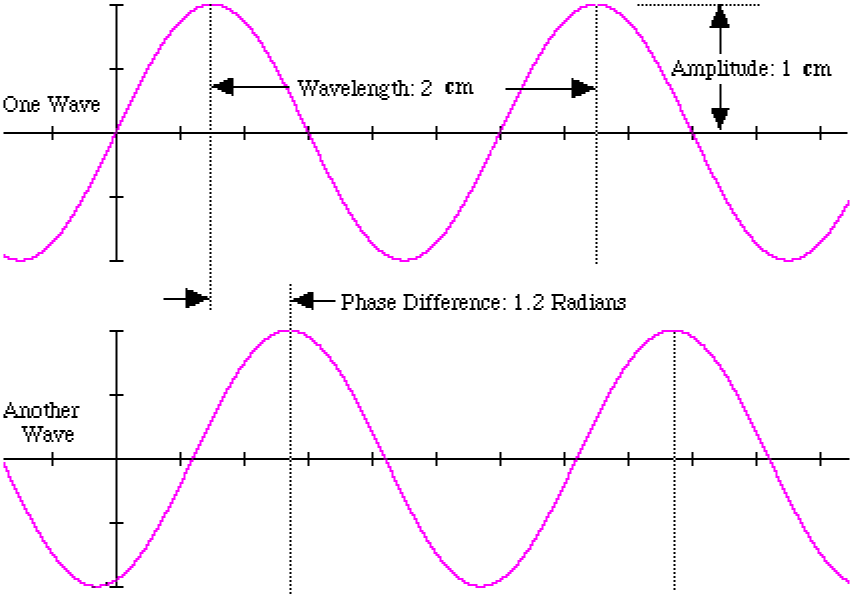

Figure 2.1 SAR phase shift between two images

Radar interferometry has proven to be an extremely reliable technique for measuring subtle deformations of man-made and natural structures. InSAR techniques are very useful in anticipating the behavior of many natural hazards such as volcanoes, earthquakes, landslide etc. [49]. Differential InSAR (DInSAR) has the capability of measuring displacement with millimeter accuracy and has been used by the scientific community for further study of ground deformation hazards [50]. The interferometric technique to detect terrain deformations require two SAR images to be taken from exactly the same position in space at two different times. Interferometric SAR was first applied to map the ground surface displacement caused by the 1992 Landers earthquake [51]. The differential interferometry (DInSAR) subtracts the topographic contribution using a Digital Elevation Model (DEM) from the differential phase values of two SAR images collected at different times over the same area of interest. In recent years, several advanced DInSAR techniques have been proposed including Persistent Scatterer Interferometric (PSI) analysis [52]. DInSAR techniques can be used to monitor short-term evolution of landslides, exploiting the information captured by Airborne UAVSAR instrument [53]. Monitoring the water protection systems is crucial for life especially for the low-lying countries like Netherlands as the majority of Dutch population is living on land reclaimed from the sea, rivers, and lakes. The persistent scatterer InSAR (PS-InSAR) technology has been used to monitor deformation of dams and dykes in the Netherlands to mitigate hazards [54]. TerraSAR imagery was used to map the deformation caused by the formation of slump slide on the levees of the Mississippi River during the great Mississippi river flooding in May 2011 [55].

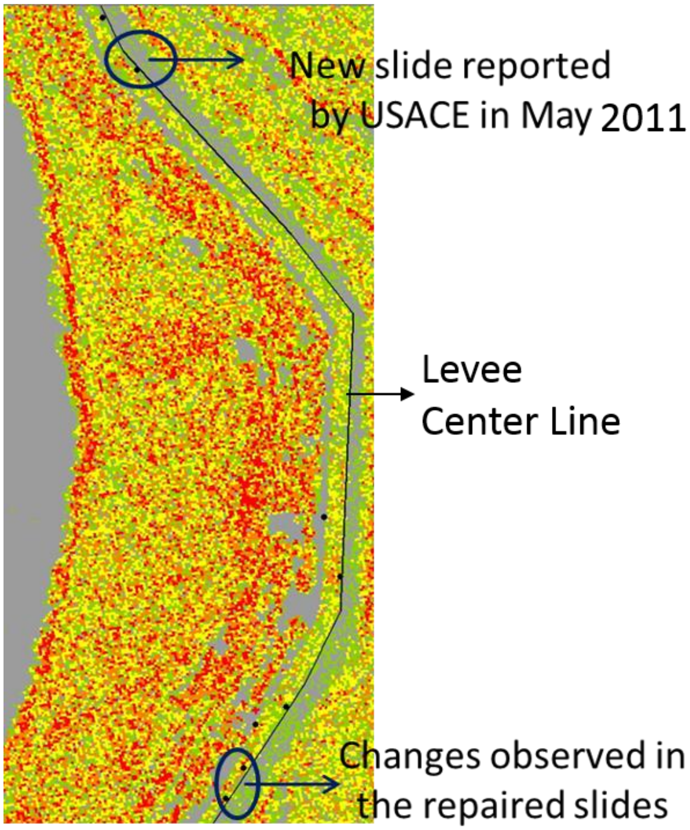

Figure 2.2 Interferogram deformation map of Mississippi river levees from March and April 2011 TerraSAR-X imagery [55].

## 2.5 References

1. Bonn, F. and Dixon, R. (2005). Monitoring flood extent and forecasting excess runoff risk with RADARSAT-1 data. *Natural Hazards* 35, 377–393.

2. Cathleen E. Jones, Gerald Bawden, Steven Deverel, Joel Dudas, Scott Hensley, Sang-Ho Yun, Study of movement and seepage along levees using DINSAR and the airborne UAVSAR instrument, , *Proc. SPIE 8536, SAR Image Analysis Modeling, and Techniques XII,* 85360E, November 2012.

3. J. V. Aanstoos, K. Hasan, C. G. O'Hara, L. Dabbiru, M. Mahrooghy, R. Nobrega, et al., "Detection of slump slides on earthen levees using polarimetric SAR imagery," in Proc. IEEE Applied Imagery Pattern Recognition Workshop (AIPR), Washington, DC, USA, 2012, pp. 1–7.

4. J. V. Aanstoos, K. Hasan, C. G. O'Hara, S. Prasad, L. Dabbiru, M. Mahrooghy, et al., "Earthen levee monitoring with synthetic aperture radar," in Proc. IEEE Applied Imagery Pattern Recognition Workshop (AIPR), Washington, DC, USA, 2011, pp. 1–6.

5. J. V. Aanstoos, K. Hasan, C. G. O'Hara, S. Prasad, L. Dabbiru, M. Mahrooghy, et al., "Use of remote sensing to screen earthen levees," in Proc. IEEE 39th Applied Imagery Pattern Recognition Workshop (AIPR), Washington, DC, USA, 2010, pp. 1–6.

6. L. Dabbiru, J. V. Aanstoos, M. Mahrooghy, W. Li, A. Shanker, and N. H. Younan, "Levee anomaly detection using polarimetric synthetic aperture radar data," in Proc. IGARSS 2012, Munich, Germany, Jul. 2012, pp. 5113–5116.

7. A. K. M. A. Hossain, G. Easson, K. Hasan, "Detection of Levee Slides Using Commercially Available Remotely Sensed Data", Environmental and Engineering Geoscience, v.12; no. 3; pp. 235 – 246, 2006.

8. Sharon L. Cundill, Mark van der Meijde, and H. Robert G. K. Hack, "Investigation of remote sensing for potential use in dike inspection," *IEEE Journal of selected topics in applied earth observations and remote sensing,* Vol. 7, No. 2, 2014.

9. Yousif A. Hussin, "Effect of polarization and incidence angle on radar return from urban features using L-band aircraft radar data," *IEEE*, 1995.

10. S. W. Lau, "Comparison and fusion of space borne L-, C-, and X-band SAR images for damage identification in the 2008 Sinchuan Earthquake," Royal Institute of Technology, June 2011.

11. V. Battsengel, D. Amarsaikhan, A. Munkh-Erdene, Ch. Bolorchuluun, and Ch. Narantsetseg, "Application of multi-frequency SAR images for knowledge acquisition," Advances in Remote Sensing, pp. 242 – 246, 2013.

12. Dabbiru, L., Aanstoos, J.V., & Younan, N. H. (2014). Comparison of L-Band and X-Band Polarimetric SAR Data Classification for Screening Earthen Levees. *IEEE Geoscience and Remote Sensing Society (IGARSS)*. Quebec, Canada: IEEE.

13. Dabbiru, L., Aanstoos, J.V., Hasan, K., Younan, N. H., & Li, W. (2013). Landslide Detection on Earthen Levees with X-band and L-band Radar Data. *2013 IEEE Applied Imagery Pattern Recognition Workshop*. Washington, DC: IEEE. DOI:10.1109/AIPR.2013.6749306.

14. Cathleen E. Jones, Brent Minchew, Benjamin Holt, and Scott Hensley, “Studies of the deepwater horizon oil spill with the UAVSAR radar,” *Monitoring and Modeling the Deepwater Horizon Oil Spill: A Record-Breaking Enterprise, American Geophysical Union,* 2011.

15. Brent Minchew, Cathleen E. Jones, and Benjamin Holt, “ Polarimetric analysis of backscatter from the deepwater horizon oil spill using L-band synthetic aperture radar”, *IEEE Transactions on Geoscience and Remote Sensing,* Vol. 50, No. 10, October 2012.

16. C. S. Lu, P. C. Chung, and C. F. Chen, “Unsupervised texture segmentation via wavelet transform,” Pattern Recognition, Vol. 30, No. 5, pp. 729 – 742, 1997.

17. S. Fukuda and H. Hirosawa, “A wavelet-based texture feature set applied to classification of multifrequency polarimetric SAR images,” IEEE Transactions on Geoscience and Remote Sensing, Vol. 37, No. 5, September 1999.

18. L. M. Bruce, C. F. Koger, and J. Li, “Dimensionality reduction of hyperspectral data using discrete wavelet transform feature extraction,” IEEE Transactions on Geoscience and Remote Sensing, vol. 40, no. 10, October 2002.

19. Huang, K., Aviyente, S., "Wavelet Feature Selection for Image Classification," *IEEE Transactions on Image Processing*, vol.17, no.9, pp. 1709-1720, Sept. 2008.

20. R. M. Haralick, K. Shanmugan, and I. H. Dinstein, “Textural features for image classification,” IEEE Trans. Syst., Man, Cybern., vol. SMC-3, pp. 610–621, May 1973.

21. Hassan Anys and Dong-Chen He, “Evaluation of textural and multipolarization radar features for crop classification,” IEEE Transactions on Geoscience and Remote Sensing, vol. 33, no. 5, September 1995.

22. Minshan Cui, Saurabh Prasad, Majid Mahrooghy, James V. Aanstoos, Matthew A. Lee , and Lori M. Bruce, “Decision fusion of textural features derived from polarimetric data for levee assessment”, *IEEE Journal of Selected Topics in Applied Earth Observations and Remote Sensing,* vol. *5*, no. *3*, June 2012.

23. M. A. Lee, J. V. Aanstoos, L. M. Bruce, and S. Prasad, “Application of omni-directional texture analysis to SAR images for levee landslide detection,” in Proc. IGARSS 2012, Munich, Germany, Jul. 2012, pp. 1805–1808.

24. Leen-Kiat Soh, and Costas Tsatsoulis, “Texture analysis of SAR sea ice imagery using gray level co-occurrence matrices”, *IEEE Transactions on Geoscience and Remote Sensing,* vol. 37, no. 2, March 1999.

25. Eric Rignot, Rama Chellappa, and Pascale Dubois, “Unsupervised segmentation of polarimetric SAR data using the covariance matrix”, *IEEE Transactions on Geoscience and Remote Sensing,* Vol. 30, No. 4, July 1992.

26. S. Fukuda, and H.Hirosawa, “Support vector machine classification of land cover: Application to polarimetric SAR data”, *IEEE,* 0-7803-7031-7/01, 2001.

27. Lalitha Dabbiru, James V. Aanstoos, and Nicolas H. Younan, “Classification of levees using polarimetric synthetic aperture radar imagery”, *39th IEEE Applied Imagery Pattern Recognition Workshop,* Proc. 2010.

28. Georgy Melamed, Stanley R. Rotman, Dan G. Blumberg, and Anthony J. Weiss, “Anomaly detection in multi-polarimetric radar images”, *IEEE,* 1-4244-2482-5/08, 2008.

29. E. Pottier, J. S. Lee, and L. Ferro-Famil, “Advanced concepts in polarimetric SAR image analysis – A Tutorial Review” *EUSAR 2004,* Neu-Ulm, Germany, May 2004.

30. Katmoko Ari Sambodo, Aniati Murni, and Mahdi Kartasasmita, “Classification of polarimetric-SAR data with neural network using combined features extracted from scattering models and texture analysis”, Remote Sensing and Earth Sciences, 2007, vol. 4.

31. Anthony Freeman and Stephen L. Durden, “A three-component scattering model for polarimetric SAR data”, IEEE Transactions on Geoscience and Remote Sensing, vol. 36, No. 3, May 1998.

32. Shane Robert Cloude and Eric Pottier, “A review of target decomposition theorems in radar polarimetry”, IEEE Transactions on Geoscience and Remote Sensing, vol. 34, No. 2, 1996.

33. Shane Robert Cloude and Eric Pottier, “An entropy based classification scheme for land applications of polarimetric SAR”, IEEE Transactions on Geoscience and Remote Sensing, vol. 35, No. 1, 1997.

34. Turker Ince, Serkan Kiranyaz, and Moncef Gabbouj, “Evolutionary RBF classifier for polarimetric SAR images,” Elsevier Expert Systems with Applications, 39, 4710 – 4717, 2012.

35. Erxue Chen, Zengyuan Li, Yong Pang, and Xin Tian, “Quantitative evaluation of polarimetric classification for agricultural crop mapping,” *Photogrammetric Engineering and Remote Sensing*, Vol. 73, No. 3, pp. 279 – 284, 2007.

36. X. Yu, L. E. Hoff, I. S. Reed, A. M. Chen, and L. B. Stotts, “Automatic target detection and recognition in multispectral imagery,” IEEE Transactions Image Processing, Vol. 6, pp. 143 – 156, January 1997.

37. Chein-I Chang, and Shao-Shan Chiang, “Anomaly detection and classification for hyperspectral imagery”, IEEE Transactions on Geoscience and Remote Sensing, Vol. 40, No. 6, June 2002.

38. E. Ohel, S. R. Rotman, and D. G. Blumberg, “Multipixel anomaly detection in noisy multispectral images,” *Optical Engineering,* Vol. 45, Issue 2, 023604, 2006.

39. M. Z. Baghbidi, K. Jamshidi, A. R. N. Nilchi, and S. Homayouni, “Improvement of anomaly detection algorithms in hyperspectral images using discrete wavelet transform,” Signal and Image Processing: An International Journal, vol. 2, no. 4, December 2011.

40. Sehat, S., Vahedifard, F., Aanstoos, J. V., Dabbiru L., Hasan, K., “Using In Situ Soil Measurements for Analysis of a Polarimetric SAR-Based Classification of Levee Slump Slides in the Lower Mississippi River.” *Engineering Geology*, 181, 157-168. doi: 10.1016/j.enggeo.2014.07.007, 2014.

41. V. Vapnik. *Statistical Learning Theory*. John Wiley and Sons, Inc., New York, 1998.

42. Bjorn Waske, and Jon Atli Benediktsson, “Fusion of support vector machined for classification of multisensor data”, *IEEE Transactions on Geoscience and Remote Sensing,* Vol. 45, No. 12, December 2007.

43. Lamei Zhang, Bin Zou, Junping Zhang, and Ye Zhang, “Classification of polarimetric SAR image based on support vector machine using multiple-component scattering model and texture features,” *EURASIP Journal on Advances in Signal Processing*, vol. 2010, doi:10.1155/2010/960831.

44. Lorenzo Bruzzone, Mattia Marconcini, Urs Wegmuller, and Andreas Wiesmann, “An advanced system for the automatic classification of multitemporal SAR images,” *IEEE transactions on geoscience and remote sensing,* Vol. 42, No. 6, 2004.

45. Yifang Ban, and Hongtao Hu, “RADARSAT fine-beam SAR data for land-cover mapping and change detection in the rural-urban fringe of the greater Toronto area,” *IEEE, Urban remote Sensing Joint Event,* 1-4244-0712-5, 2007.

46. Y. Oh, K. Sarabandi, and F. T. Ulaby, "An empirical model and an inversion technique for radar scattering from bare soil surfaces", *IEEE Trans. Geosci. Remote Sensing*, vol. 30, pp.370 -382 1992.

47. Y. Oh,, "Quantitative retrieval of soil moisture content and surface roughness from multipolarized radar observations of bare soil surfaces," *Geosciences and Remote Sensing, IEEE Transactions on*, vol.42, no.3, pp. 596- 601, March 2004.

48. P. C. Dubois, J. van Zyl, and E. T. Engman, “Measuring soil moisture with imaging radar”, *IEEE Trans. Geosci. Remote Sensing*, vol. 33, pp.916 -926, 1995.

49. Zhong Lu, Ohig Kwoun, and Russel Rykhus, “Interferomeric synthetic aperture radar (InSAR): Its past, present and future,” *Photogrammetric Engineering and Remote Sensing,”* March 2007.

50. Rosen, P. A., Hensley, S., Joughin, I. R., Li, F. K., Madsen, S. N., Rodriguez, E., and Goldstein, R. M. (2000). “Synthetic aperture radar interferometry”, *Proc IEEE* 88(3):333–382.

51. Massonnet, D., and K. Feigl, “Radar interferometry and its application to changes in the Earth’s surface,” Rev. Geophys., 36,441-500, 1998.

52. Ferretti, A., Prati, C., and Rocca, F. (2000). “Nonlinear subsidence rate estimation using permanent scatterers in differential SAR interferometry”, *IEEE Transactions on Geoscience and Remote Sensing*, vol.38, no.5.

53. Scott Hensely, Howard Zebker, Cathleen Jones, Thierry Michel, Ron Muellerschoen, and Bruce Chapman, “Use of airborne SAR interferometry for monitoring deformation of large-scale man-made features,” *International workshop Spatial Information Technologies,* 2010.

54. Ramon F. Hanssen, and Freek J. van Leijen, “Monitoring water defense structures using radar interferometry,” *Radar Conference, IEEE,* 2008.

55. James Aanstoos, Lalitha Dabbiru, Khaled Hasan, Matthew Lee, Majid Mahrooghy, Rodrigo Nobrega, Chales O’Hara, Saurabh Prasad, and Arjun Shankar, “Screening of levees by synthetic aperture radar,” *SERRI Report 90008-01,* 2012.

# CHAPTER III

# SYNTHETIC APERTURE RADAR (SAR)

## 3.1 Synthetic Aperture Radar (SAR) Data

Synthetic Aperture Radar (SAR) transmits electromagnetic waves at a wavelength that can range from a few millimeters to tens of centimeters and operates during day and night under all weather conditions. The intensity and phase of the backscattered (reflected) radar signal from each element on the ground can be put in the form of a complex valued SAR image. The intensity / magnitude of the SAR image depends primarily on terrain slope, surface roughness, and dielectric constants (soil moisture), whereas the phase of the radar image depends on the distance between the radar antenna and the ground targets.

Synthetic Aperture Radar technology, due to its high spatial resolution and potential soil penetration capability, is a good choice to identify problem areas on levee so that they can be treated to avoid possible catastrophic failure. The radar backscatter data is capable of identifying variations in soil properties of the areas that might cause levee failure. This research is mainly focused on analyzing different algorithms to assess the condition of levee structure using multi-polarized SAR images.

## 3.2 Radar Polarimetry

In polarimetric SAR, the transmitted signal is polarized and different polarizations of the backscatter signal are detected. The radar polarization describes the direction of the orientation of the electric field component of an electromagnetic wave, and imaging radars can have different polarization configurations. The electric and magnetic fields are perpendicular to each other. If the direction of the electric field wave crest is aligned along the horizontal axis it is called a horizontally polarized wave, and if the electric field wave crest is oriented / aligned in the vertical direction it is called a vertically polarized radar wave. Figure 3.1 depicts the horizontal and vertical polarized radar waves. There are many different ways to mix the horizontal and vertical pulses together in a transmission scheme. The transmitted radar waves can be horizontally (H) or vertically (V) polarized and can be received in both H and V. With different polarizations, HH (Horizontal transmit and Horizontal receive), HV (Horizontal transmit and Vertical receive), VH (Vertical transmit and Horizontal receive) and VV (Vertical transmit and Vertical receive), SAR imagery can be used to separate different causes contributing to changes in the backscatter signal.

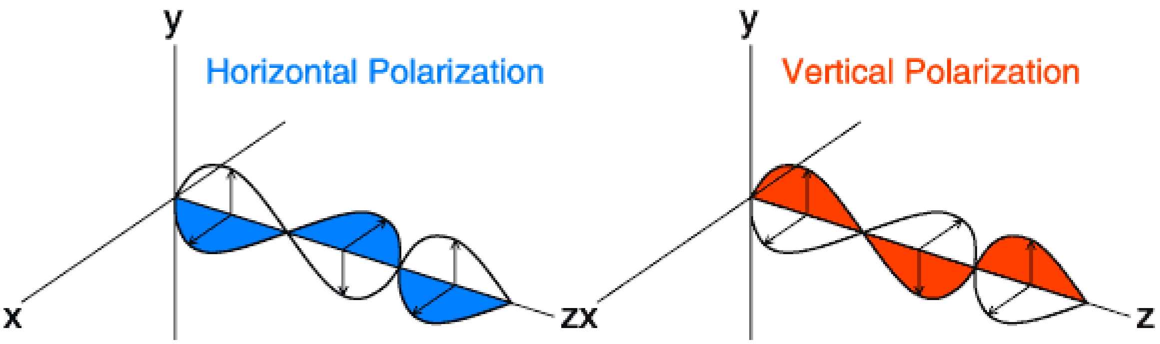

Figure 3.1 (a) Horizontally polarized radar wave: the electric field (blue) is aligned along the horizontal axis and the magnetic field is aligned along the vertical axis (white) (b) vertically polarized radar wave: the electric field (red) is aligned along the vertical axis and the magnetic field is aligned along the horizontal axis (white) [1].

### 3.3 Radar Data Formats

A SAR image is a 2-D array of pixels formed by columns and rows where each pixel is associated with a small area on the Earth's surface depending on the sensor's spatial resolution. Each pixel is represented as a complex number; has both magnitude and phase measures. The complex number is often represented by an equivalent pair of numbers, the real in-phase component and the imaginary quadrature component. One dimension of the image called "range" or "cross-track", which is a measure of the line-of-sight distance from the radar to the target. The other dimension is called "azimuth" or "along-track" and is perpendicular to the range. The surface reflectivity, which is expressed as a radar backscattering coefficient $\sigma^o$ ("sigma zero" or "sigma nought"), is a function of the radar frequency, polarization, incidence angle of the electromagnetic wave $\theta i$, and the surface parameters like topography, local incidence angle, surface roughness, and dielectric properties [2].

### 3.3.1 Single Look Complex (SLC) Image

The radar SLC is a single look complex, phase preserved, slant range image generated from the raw SAR data for each polarization (HH, HV, VH and VV) channel. Each pixel is represented as a complex number; has both magnitude and phase of the electromagnetic wave [3]. Apart from the amplitude data, the major advantage of this data is that it contains phase information and has the highest possible resolution. However, the single-look images are very speckled and in slant range, which makes visual interpretation and characterization very difficult.

In radar remote sensing, the concept of phase is usually applied to the oscillation of electromagnetic waves. The complex number format is given by:

$$A * (\cos(\omega t) + i * \sin(\omega t)) \tag{3.1}$$

where ω is the wave frequency, A is its amplitude and A*cos(ωt) is the cosine or the real component and A*sin(ωt) is the sine or imaginary component. When translated to real and imaginary axes complex format this wave is defined by I = Acos(θ) and Q= Asin(θ) and the amplitude A is defined as A = sqrt (I2 + Q2) (Figure 3.2) [4].

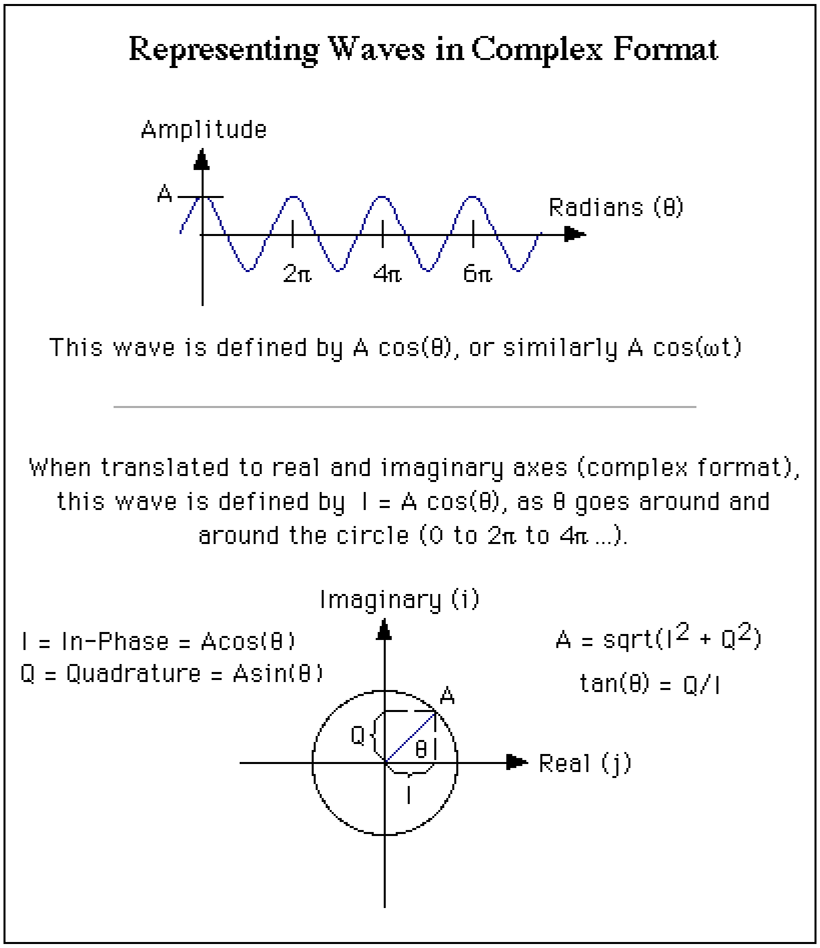

Figure 3.2 Representation of waves in complex format [4].

### 3.3.2 Multi-Look Cross Product (MLC) Image

The multi-look processing technique is widely used in radar applications due to speckle reduction by averaging single-look pixels. A multi-looking radar image not only improves the image quality by reducing the speckle noise but it can also be useful for correcting the geometric and radiometric distortions. These multi-look pixels are derived from the average of the product of each single-look pixel. These complex cross products preserve most of the important amplitude and phase information that are needed to analyze the data. Overall, the MLC images have improved radiometric resolution with less speckle noise but have degraded spatial resolution.

### 3.3.3 Ground Range Detected (GRD) Image

The ground range detected (GRD) product consists of multi-looked SAR data projected to the ground range using an Earth ellipsoid model. The resultant product has square pixels with reduced speckle and reduced geometric resolution.

## 3.4 Radar Frequency Bands

The radar systems work in a wide band of transmitted frequencies, from 1 GHz to 110 GHz. Radars with longer wavelength (lower transmission frequencies) are less affected by weather conditions such as rain and clouds. However, the higher the transmitted frequency, the better the potential resolution of the radar system is [5]. Table 3.1 shows the frequency bands used by radar systems [6]. For example, the X-band radars have higher penetration capability through clouds / rain / fog than the Ka band radars. This research uses the data from the L-band and X-band sensors.

Table 3.1 Frequency bands used by radar systems

| Frequency Band | Frequency Range (GHz) | Wavelength Range (cm) |
|---|---|---|
| P band | 0.3 - 1 | 30 – 100 |
| L band | 1 - 2 | 15 – 30 |
| S band | 2 - 4 | 7.5 – 15 |
| C band | 4 – 8 | 3.75 – 7.5 |
| X band | 8 – 12 | 2.5 – 3.75 |
| Ku band | 12 – 18 | 1.67 – 2.5 |
| K band | 18 – 27 | 1.11 – 1.67 |
| Ka band | 27 – 40 | 0.75 – 1.11 |
| V band | 40 – 75 | 0.4 – 0.75 |
| W band | 75 - 110 | 0.27 – 0.4 |

### 3.4.1 Surface roughness variation with different radar frequency bands

Surface roughness on the levee refers to multiple irregularities that relate either to textures or the objects on them such as vegetation or slump slides. A surface is characterized as “smooth” or “rough” depending on the wavelength of the radar and the height of an irregularity. For example, a Ka-band radar reflects the surface with moderate roughness as “rough” due to its lower wavelength ($\lambda = 0.85$ cm), whereas an L-band radar may reflect the same surface as “smooth” due to its higher wavelength ($\lambda = 24$ cm). Greater height variations compared with the wavelength will appear rough even to the L-band. Roughness is a relative concept depending upon the wavelength and incidence angle. According to the Rayleigh criterion [7], a surface is considered rough if:

$$h > \frac{\lambda}{4.4\cos\theta} \tag{3.2}$$

where h is the mean height of surface variations, $\lambda$ is the wavelength, and $\theta$ is the incidence angle.

### 3.4.2 Effect on ground penetration with different radar frequency bands

The radar backscatter is influenced by the frequency of the radar wave and the penetration depths of different radar bands vary with its wavelengths; the longer the wavelength, the greater the penetration depth. Therefore, the L-band radar penetrates deeper than the X-band sensor. In extremely dry conditions, the L-band SAR can penetrate up to a 1 meter in depth, but in most cases the radar penetration is typically only a few centimeters. The radar penetration can be valuable for detecting near-surface soil moisture; the backscatter strength increases as the soil moisture increases.

## 3.5 Airborne and Space-borne Polarimetric SAR Systems

Synthetic Aperture Radar is mostly a space-borne or airborne side-looking radar system which utilizes the flight path of the platform to synthesize a long aperture. SAR is the only practical technique to achieve high spatial resolution remote sensing imagery even from space platforms. In this research, airborne UAVSAR data and space-borne TerraSAR-X data has been used which is discussed in detail below.

### 3.5.1 Airborne Radar – UAVSAR

UAVSAR is a quad-polarized L-band ($\lambda = 25$ cm) airborne radar, was developed by NASA's Jet Propulsion Laboratory (JPL) for acquiring repeat track SAR data. The L-band quad-polarized data from UAVSAR describes the complete polarimetric signature of the objects in the target area, with a range bandwidth of 80 MHz, and support a 16 km range swath flown at a nominal altitude of 13,800 m. The exceptionally low noise equivalent sigma zero allows UAVSAR to detect targets with weak radar backscattering cross section and to improve the accuracy of geophysical measurements such as soil moisture and vegetation biomass. The key parameters of the UAVSAR instrument are given in Table 3.2 [8].

Table 3.2 UAVSAR Instrument Key Parameters

| Parameter | Value |
|---|---|
| Frequency | L- Band (1.26 GHz) |
| Bandwidth | 80 MHz |
| Range Resolution | 1.8 m |
| Polarization | Quad Polarization |
| Raw ADC Bits | 12 baseline |
| Range Swath | 16 km |
| Look Angle Range | 25° - 60° |
| Transmit Power | > 2.0 KW |
| Altitude Range | 2000 – 18000 m |

Using a precision real-time global positioning system and a sensor-controlled flight management system, the aircraft flies predefined paths with great precision. The radar is designed to be operable on a UAV, but for the flight used to collect data for this research it was flown on the NASA Gulfstream III aircraft. Figure 3.3 shows the NASA Gulfstream III aircraft with radar pod. For UAVSAR imagery, each pixel in the SLC file is a complex floating point data with 8 bytes / pixel. For example, each UAVSAR multi-look pixel is derived from averaging 3 single-look pixels in range and 12 pixels in azimuth [9]. Multi-look data saves only the cross-products of the elements of the scattering matrix. Three of the files are complex 8 bytes per pixel (ShhShv*, ShhSvv*, ShvSvv*, where * means complex conjugate) and the other three files are real floating point data with 4 bytes per pixel (ShhShh*, ShvShv*, SvvSvv*).

Figure 3.3 NASA Gulfstream III aircraft with a pod housing the UAVSAR

### 3.5.2 Space-borne Radar - TerraSAR-X

TerraSAR-X is a German radar satellite which carries a high frequency X-band synthetic aperture radar sensor and can be operated in different modes and polarizations [10]. It is a side-looking radar based on active phased array antenna technology. The SAR sensor operates in different operation modes as given in Table 3.3.

Table 3.3 TerraSAR-X operation modes with swath width and resolutions

| | Stripmap | Spotlight (HS & SL) | ScanSAR |
|---|---|---|---|
| Swath Width (range) | 30 km (single pol.)<br>15 km (dual pol.) | 10 km @ 150 MHz chirp BW<br>Azimuth: 5 / 10 km (HS / SL) | 100 km (only single pol.) |
| Full performance incidence angle range | 20° - 45° | 20° - 55° | 20° - 45° |
| Azimuth resolution | 3.3 m (single pol.)<br>6.6 m (dual pol.) | 1.1 m / 2.2 m (HS, single / dual pol.)<br>1.7 m / 3.4 m (SL, single / dual pol.) | 17 m<br>(1 look, 4 beams) |

The key parameters of this space-borne sensor are given in Table 3.4 [11].

Table 3.4 TerraSAR-X key parameters

| Parameter | Value |
|---|---|
| Radar Carrier Frequency | 9.65 GHz |
| Range Bandwidth | 150 MHz |
| Radiated RF Peak Power | 2 kW |
| Polarization | HH, HV, VH, VV |
| Incidence Angle Range | 20° - 55° full performance |
| Nominal Orbit Height at the Equator | 514 km |
| Revisit time | 11 days |
| Inclination | 97.44° |
| Normal Look Direction | Right |
| Pulse Repetition Frequency | 2.0 kHz – 6.5 kHz |

## 3.6 References

1. National Oceanic and Atmospheric Administration, http://www.crh.noaa.gov/dualpol/index.php?wfo=oax

2. Jong-Sen Lee and Eric Pottier, “Polarimetric Radar Imaging – From basics to applications”, CRC Press, Taylor & Francis Group, 2009.

3. Henri Maitre, “Processing of synthetic aperture radar images”, John Wiley & Sons, May 2013.

4. ESA Earthnet online, “ASAR documentation”, https://earth.esa.int/handbooks/asar/CNTR4.htm.

5. Christian Wolf, “Radar Tutorial,” http://www.radartutorial.eu/07.waves/Waves%20and%20Frequency%20Ranges.en.html

6. American Meteorological Society, “Radar frequency bands”, http://glossary.ametsoc.org/wiki/Radar_frequency_band

7. John R. Jensen, “Remote Sensing of the Environment”, Second Edition, ISBN: 0-13-188950-8.

8. Rosen, P.A., S. Hensley, K. Wheeler, G. Sadowy, T. Miller, S. Shaffer, R. Muellerschoen, C. Jones, H. Zebker, and S. Madsen, "UAVSAR: A New NASA Airborne SAR System for Science and Technology Research," IEEE Radar Conference, Verona, NY, 2006, pp. 8.

9. Uninhabited Aerial Synthetic Aperture Radar, UAVSAR, “Polarimetric (PolSAR) Data Format”, http://uavsar.jpl.nasa.gov/science/documents/polsar-format.html

10. A. Roth, J. Hoffmann, and T. Esch, “TerraSAR-X: How can high resolution SAR data support the observation of urban areas?”, In: Proceedings of the ISPRS WG VII/1 “Human Settlements and Impact Analysis” 3rd International Symposium Remote Sensing and Data Fusion Over Urban Areas (URBAN 2005) and 5th International Symposium Remote Sensing of Urban Areas (URS 2005), Tempe, AZ, USA, March 14–16, 2005.

11. TerraSAR-X ground segment basic product specification document, http://www.dlr.de/Portaldata/1/Resources/raumfahrt/weltraum/TX-GS-DD-3302_Basic-Product-Specification-Document_1.5.pdf.

# CHAPTER IV

# STUDY AREA AND DATA USED

## 4.1 Study Area

The Mississippi levee system represents one of the largest in the world, comprising over 3500 miles of levees. Detecting anomalies on the levee to identify problem areas is an important factor to consider to protect them from flooding. The study area for this research focuses on the mainline levee system of the Mississippi River along the eastern side of the river in Mississippi. The study area was selected based on the history of levee failure events occurring in the lower Mississippi valley. This history can facilitate the investigation of the use of remote sensing data to analyze physical factors that would indicate problems in levee conditions, whether they arise from moisture content, slope instability, hydraulic uplift, water seepage through levees, or underseepage resulting in sand boils.

## 4.2 Data Used

This study employed remote sensing data from multiple sources, primarily from polarimetric synthetic aperture radar data acquired by airborne and satellite-based sensors to characterize levee segments for variability, anomalies, changes in texture and other factors that would lend credible evidence to potential or actual problems with the levees in areas so identified.

### 4.2.1 UAVSAR L-band Data

JPL’s UAVSAR flew over levees in our study area where we expected to find anomalies. A total of five multi-temporal data collections were made: 1) June 16, 2009; 2) January 25, 2010, 3) April 28, 2011; 4) June 7, 2011; and 5) June 22, 2011. The UAVSAR 3-band color composite image is shown in Figure 4.1. The UAVSAR data acquired on June 16, 2009 and January 25, 2010 were used in this study as there were active slides during these two image acquisitions.

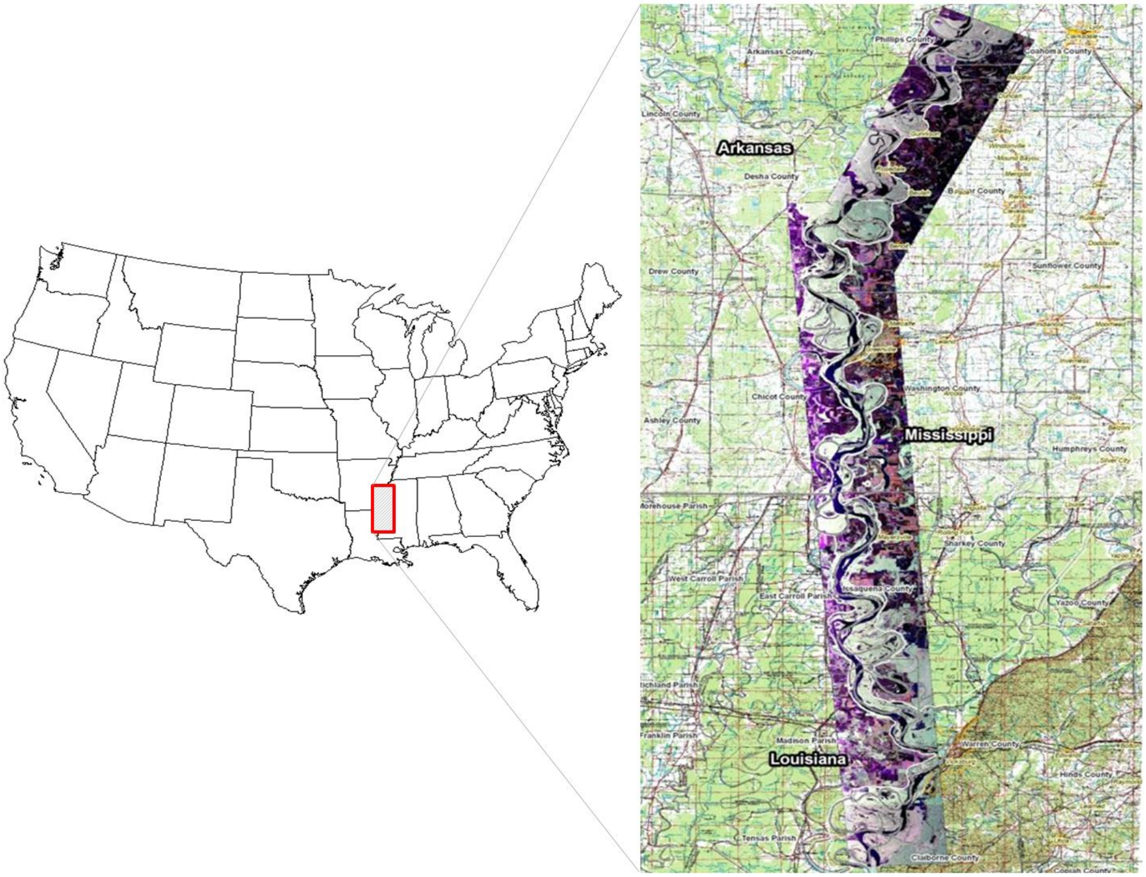

Figure 4.1 Polarimetric UAVSAR 3 band (HH, HV, and VV) data shown in color composite along the lower Mississippi River.

Image swath width is 20 km; total flight line length is 230 km.

### 4.2.2 TerraSAR-X X-band Data

In addition to the airborne UAVSAR data, satellite-based radar data from Germany's TerraSAR-X instrument have been investigated in this research. The SpotLight (SL) mode images provides a good balance between ground resolution and scene extent, and the majority of images were collected in this mode. All the images were right-looking from an ascending path as this gave maximum parallelism between the satellite orbit and the course of the Mississippi River in the study area. The SpotLight image shown in Figure 4.2, acquired on September 15, 2010 with an incidence angle of 33° was used in the study as there was one active slide at the time of image acquisition.

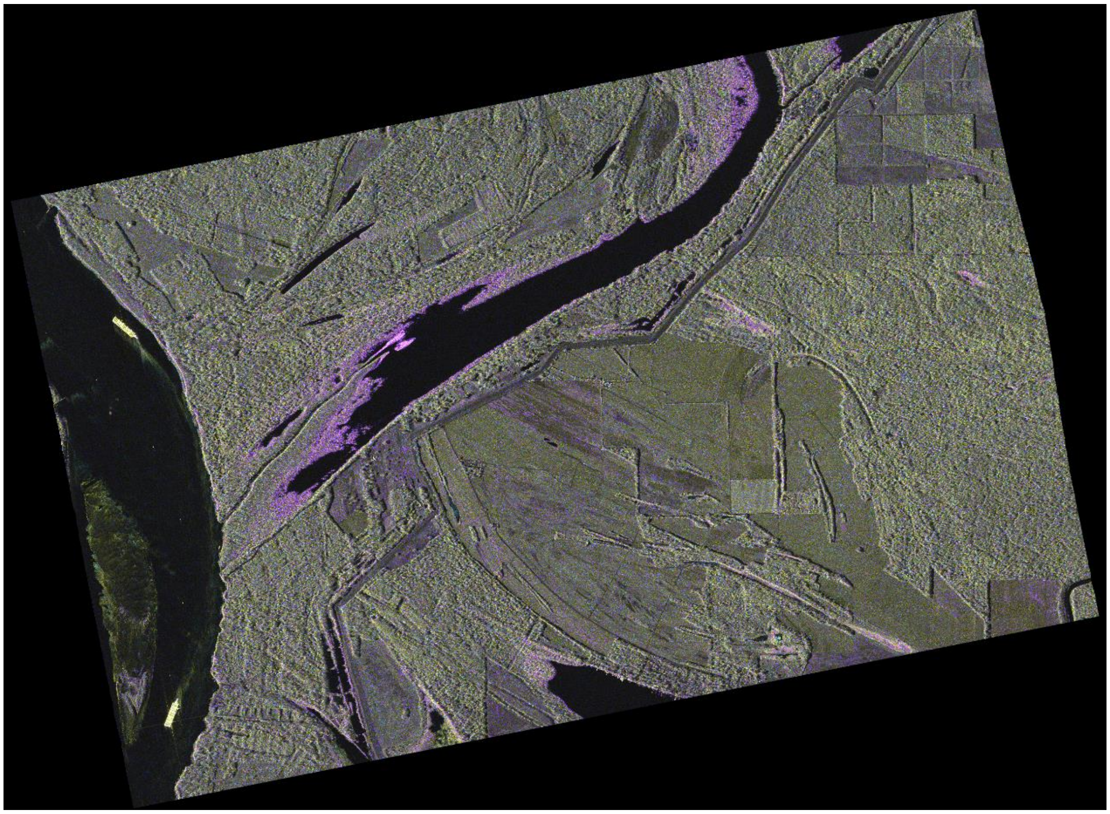

Figure 4.2 Color composite of dual-polarized (HH and VV) TerraSAR-X data of September 15, 2010.

## 4.3 Ground Truth (In Situ) Data

In addition to the remotely sensed data, we relied on ground truth data to train, test, and validate the machine learning classifiers. To provide detailed information on soils on the levees in the study area, ground truth data was collected by both U.S. Army Corp of Engineers (USACE) and our research team. This data included the exact location and timing of slump slides, photographs of the vicinity, and the notes on grass height.

USACE has a major responsibility for supporting flood risk management activities. The Corps of Engineers has constructed approximately 11,750 miles of riverine levees for shoreline protection, hundreds of locks and dams for navigation, and dams for multiple purposes including hydroelectric power generation and flood control [1]. The USACE maintains a national inventory of levee systems and makes the information available in the National Levee Database (NLD) [2]. It provides information about the location and condition of levees and floodwalls. USACE regularly inspects levees to monitor their condition, identify deficiencies, and verify that needed maintenance is taking place. The levee managers are responsible for the rehabilitation, evaluation, maintenance, and repair of the levees in a timely way to mitigate risk of catastrophic failures. Flood risks can be mitigated by protective structures and USACE builds berms or installs relief wells on levees to mitigate underseepage. The ground truth data which is used in this research was obtained from USACE Engineer Research and Development Center (ERDC) in Vicksburg, Mississippi.

In addition, we took samples of soil moisture and measured soil electrical conductivity. GPS polygons were taken using a Trimble GPS on several slide and nonslide (healthy) parts of levees which were used as training masks in the classification tasks (Figure 4.3).

Figure 4.3 Field data collection on Mississippi River levees near Albemarle Lake, MS.

Levee vegetation consists mostly of grasses and weeds. Three types of grasses predominate on the levees in the study area are: Bermuda, Rye, and Johnson grass. In the field campaign we observed that grasses grown over areas with cracks and fractures are stressed for moisture compared to the grasses grown over healthy areas of the levee. It was also observed that grasses growing in repaired slide areas were either of different type or had different vigor compared to the healthy levee [3]. The differences in vegetation growth (sparse or dense) and vegetation type (Bermuda grass, weeds etc.) influence the radar backscatter and are distinguishable in the imagery. The ground truth was supplemented by high resolution aerial photography from National Agriculture Imagery Program (NAIP) shown in Figure 4.4. The ground truth data from the Mississippi Levee Board with active slough slides during 2009 and 2010 radar imagery acquisitions and their repair status is given in Table 4.1.

Table 4.1 Levee Slides Data from Mississippi Levee Board

| From Mississippi Levee Board (08 April 2011) | | |
|---|---|---|
| Slide # (ArcGIS FID) | Date Slide Appeared | Date Slide Repaired |
| 17 | October 2009 | November 2009 |
| 18 | October 2009 | November 2009 |
| 20 | August 2008 | November 2009 |
| 21 | Not Available | September 2010 |
| 22 | September 2009 | April 2010 |
| 25 | February 2009 | September 2010 |

Figure 4.4 National Agriculture Imagery Program (NAIP) imagery of August, 2008. The red dots on the image show the slide locations with slide numbers (ArcGIS FID).

## 4.4 References

1. Corps of Engineers Water Resources Infrastructure, National Research Council, National Academies Press, ISBN 978-0-309-26476-1, 2012.

2. US Army Corps of Engineers, National Levee Database (NLD) http://www.usace.army.mil/Missions/CivilWorks/LeveeSafetyProgram/NationalLeveeDatabase.aspx.

3. Khaled Hasan, James V. Aanstoos, and Majid Mahrooghy, " Stressed Vegetation Identification by SAR Time Series as an Indicator of Slope Instability in Mississippi River Levee Segments," IEEE Applied Imagery Pattern Recognition Workshop, DOI:10.1109/AIPR.2013.6749307.

# CHAPTER V

# METHODOLOGY

## 5.1 Automated Levee Target Recognition System

The goal of the earthen levee classification is to develop machine learning algorithms and a set of features that could be used to identify areas on levees that have an increased likelihood of being vulnerable to failure under high water conditions. In this study, the focus is on the detection of slump slides using L-band and X-band SAR data. Several supervised and unsupervised classification algorithms have been applied to the SAR data for efficient levee classification with different set of features (DWT and GLCM).

The unsupervised and supervised classification block diagrams are shown in Figure 5.1 and Figure 5.2. The UAVSAR multi-polarized, multi-look radar image and TerraSAR-X dual polarization data are used in the classification tasks. For unsupervised classification, the levee is segmented into a 40 meter buffer and the texture features are extracted from the original SAR data. Not all of the components of the feature set useful, so only the useful features were selected and used in the classification tasks. In the supervised approach, the training masks were drawn based on the ground truth data and the classifiers were run on the extracted feature set.

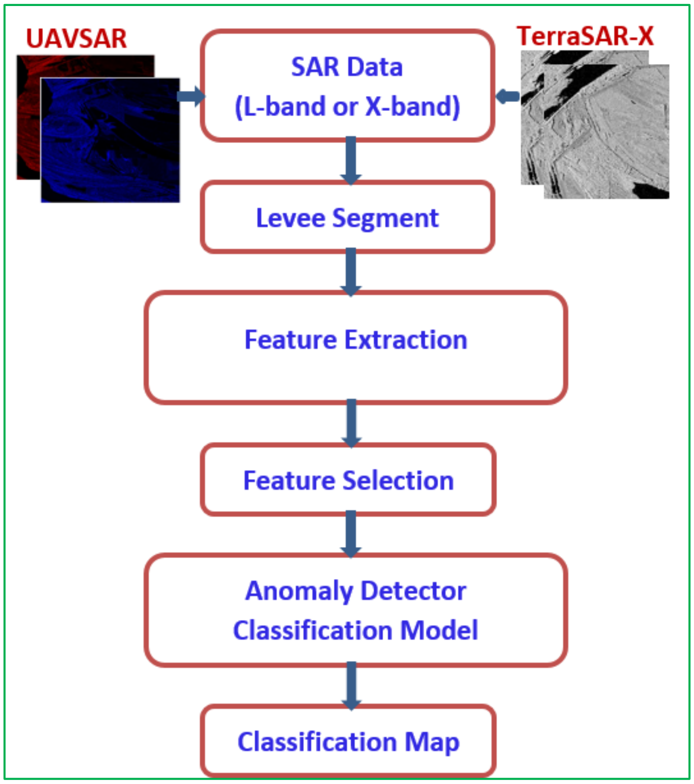

Figure 5.1 Block diagram of Unsupervised Classification approach

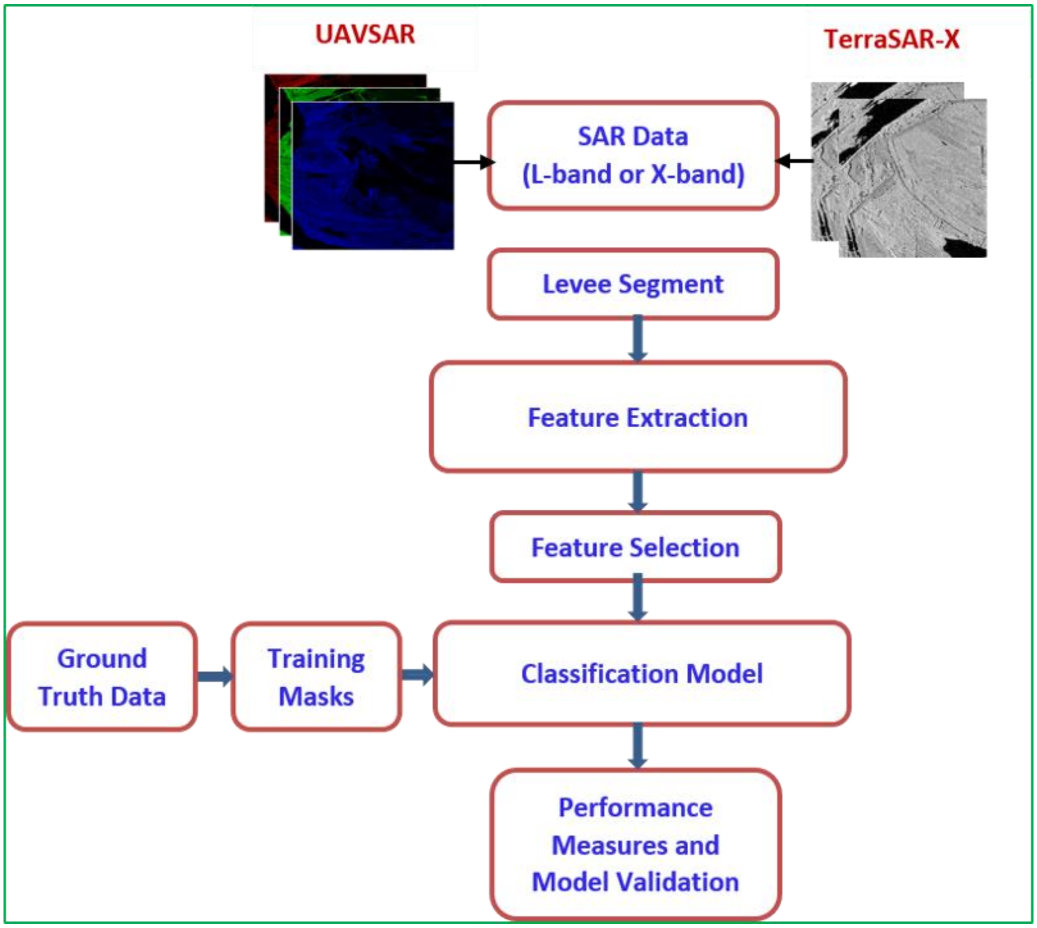

Figure 5.2 Block diagram of Supervised Classification approach

## 5.2 Feature Extraction

In general, feature extraction is a two-step process, the first step being feature construction and the second step feature selection. Feature construction is the process where a feature set is extracted from the original dataset. In this research, polarimetric and texture features are extracted from the SAR data. The polarimetric features are pixel-based and the texture features are window-based. Not all the components of the feature set are useful, so only the useful features were selected and used in the classification tasks.

### 5.2.1 Polarimetric Decomposition Features: Entropy (H), Anisotropy (A), Scattering Angle (Alpha)

#### 5.2.1.1 Polarimetric Decomposition

In Polarimetric SAR (PolSAR), the transmitted signal is polarized and different polarizations of the backscatter signal are detected. Polarimetric SAR measurements can be used to retrieve different types of land use and land cover information. PolSAR data can also be used to estimate soil moisture. The backscattering properties of the target are described by a 2x2 complex backscattering matrix S [1] which represents the reflectivity of the area and can be expressed as:

$$\text{Scattering Matrix S} = \begin{bmatrix} \mathrm{S_{hh}} & \mathrm{S_{hv}} \\ \mathrm{S_{vh}} & \mathrm{S_{vv}} \end{bmatrix} \quad (5.1)$$

where h indicates horizontal polarization and v indicates vertical polarization.

In order to relate the polarimetric backscatter to the physical properties of the scatterer, the target vector $K_p$ is represented in the 3-D Pauli basis as shown below [2].

$$\text{Scattering Matrix } \bar{\mathrm{K}}_{\mathrm{p}} = \frac{1}{\sqrt{2}} \begin{bmatrix} S_{hh} + S_{vv} \\ S_{hh} - S_{vv} \\ 2S_{hv} \end{bmatrix} \quad (5.2)$$

($S_{hv} = S_{vh}$ due to symmetry)

The coherency matrix [T] contains the second order statistical information about the polarization and is defined as the product of the target vector $K_p$ with its complex conjugate transpose and is given by:

$$\text{Coherency Matrix [T]} = \bar{\mathrm{K}}_{\mathrm{p}} \, . \, \bar{\mathrm{K}}_{\mathrm{p}}^{*\mathrm{T}} \quad (5.3)$$

where * and T represent complex conjugate and transpose, respectively.

For single look or multi-look processed data, the coherency matrix is defined as:

$$T = \langle \overline{K_p} . \overline{K_p^{*T}} \rangle =$$

$$\frac{1}{2}\begin{bmatrix} \langle |S_{HH} + S_{VV}|^2 \rangle & \langle (S_{HH} + S_{VV})(S_{HH} - S_{VV})^* \rangle & 2\langle (S_{HH} + S_{VV})S_{HV}^* \rangle \\ \langle (S_{HH} - S_{VV})(S_{HH} + S_{VV})^* \rangle & |S_{HH} - S_{VV}|^2 & 2\langle (S_{HH} - S_{VV})S_{HV}^* \rangle \\ 2\langle S_{HV}(S_{HH} + S_{VV})^* \rangle & 2\langle S_{HV}(S_{HH} - S_{VV})^* \rangle & 4\langle |S_{HV}|^2 \rangle \end{bmatrix} \quad (5.4)$$

The diagonal elements T11, T22, and T33 give the surface, double-bounce, and volume scattering information about the target. The VV backscatter ($\sigma^0{}_{vv}$) dominates at the surface scattering areas, HV backscatter ($\sigma^0{}_{hv}$) dominates in the volume scattering, and HH ($\sigma^0{}_{hh}$) dominates in double bounce areas.

#### 5.2.1.2 Polarimetric Features

Cloude and Pottier [2] [3] developed a polarimetric decomposition theorem based on eigenvector analysis of the 3x3 coherency matrix T3. The decomposition parameters entropy (H), scattering angle (α), and anisotropy (A) are extracted from the coherency matrix [2] [3].

##### 5.2.1.2.1 Entropy (H)

The parameter entropy (H) is a measure of randomness in the distributed scatterer and is defined as the logarithmic sum of the eigenvalues as [4]

$$Entropy\ H = -\sum_{i=1}^{3} p_i \, log_3(p_i) \qquad (5.5)$$

$$where\ p_i = \frac{\lambda_i}{\sum_{k=1}^{3} \lambda_k} \qquad (5.6)$$

with $p_i$ corresponding to the probability of the eigenvalue $\lambda_i$.

For smooth surfaces, H becomes zero, implying a non-depolarizing scattering and increases with surface roughness. Low entropy ($H < 0.3$) indicates single scattering and $H > 0.7$ indicates random scattering.

#### 5.2.1.2.2 Anisotropy (A)

The anisotropy parameter is used to distinguish different types of scattering mechanisms with different eigenvalue distributions. This parameter measures the importance of the second and third eigenvalues of the Eigen decomposition and is given by:

$$\text{Anisotropy } A = \frac{\lambda_2 - \lambda_3}{\lambda_2 + \lambda_3} \tag{5.7}$$

Anisotropy can be considered a measure of the lack of azimuth symmetry or as an indication of the small-scale surface roughness. For azimuthally symmetric surfaces, $\lambda_2 = \lambda_3$ and A becomes zero. The anisotropy can be employed as a source of discrimination mainly when the entropy values are greater than 0.7 [4]. For low entropy values, the second and third eigenvalues are affected by noise and consequently anisotropy is also very noisy. Anisotropy is highly affected by noise [5]; therefore UAVSAR provides better anisotropy evaluations because UAVSAR has higher signal-to-noise ratio (SNR).

#### 5.2.1.2.3 Mean Alpha Angle (α)

The parameter $\alpha$ is an indicator of the type of scattering mechanism occurring, which ranges from 0 to 90° and is defined as:

$$\alpha = \sum_{i=1}^{3}(p_i\,\alpha_i) \tag{5.8}$$

α = 0° if the target has a dominant surface or single-bounce scattering component, the value of α = 45° indicates volume scattering, and α = 90° corresponds to double-bounce scattering.

By interpreting the analysis as a measure of entropy and scattering angle, the classification of the scene can be separated into nine scattering zones and is shown in Figure 5.3 [2] [7].

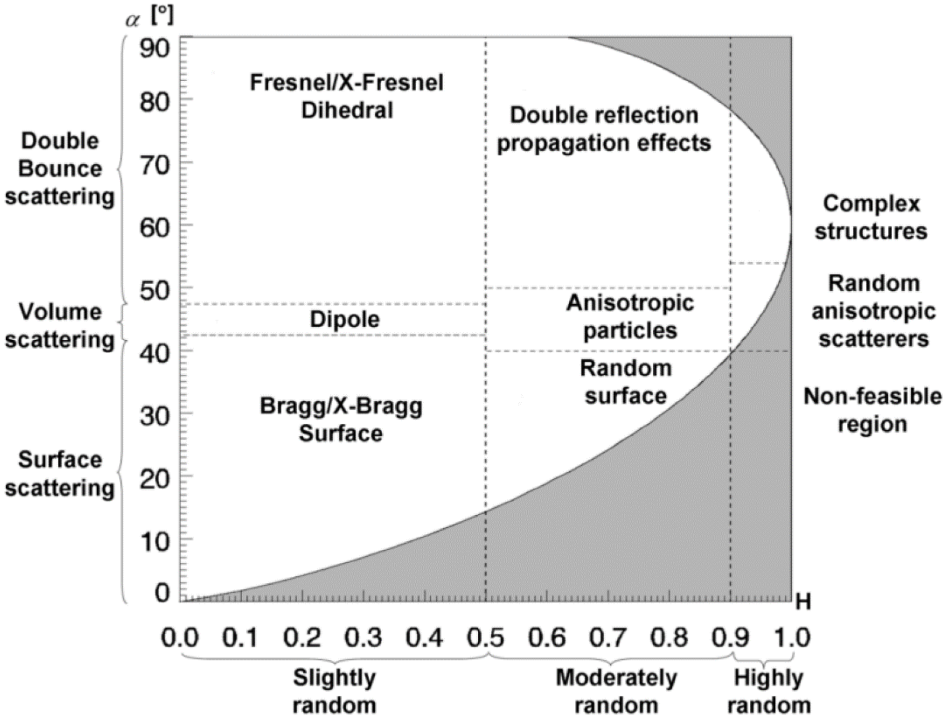

Figure 5.3 Entropy – Alpha (H - α) plane showing different scattering mechanisms

### 5.2.2 Feature Extraction using Discrete Wavelet Transform (DWT)

Texture is an important feature to the classification of land cover in radar images because it has the ability to examine the signal at different scales. In this research, a wavelet-based texture feature set is computed for the polarimetric multi-band radar imagery and utilized in the classification tasks.

As shown in Figure 5.4, the wavelet decomposition of an image generates four sub-images: 3 detail images and 1 approximation image. In each decomposition level, the approximation image is passed through low pass and high pass filters to generate the next level of coefficients. The detail images contain the high frequency components, whereas the approximation image contains the low frequency components.

The DWT is used to decompose an original signal $x[n]$ into approximation $A_j(k)$ and detail $D_j(k)$ coefficients by passing $x[n]$ through a series of high-pass filters $g[n]$ to analyze the high frequencies and low-pass filters $h[n]$ to analyze the low frequencies [8] [9]. Filtering a signal corresponds to the mathematical operation of convolution of the signal with the impulse response $h[n]$ of the filter.

$$x[n] * h[n] = \sum_{k=-\infty}^{\infty} x[k].h[n-k] \tag{5.9}$$

After filtering, half of the samples can be eliminated according to the Nyquist rule. Therefore, the output of HPF and LPF would be:

$$y_{high}[k] = \sum_n x[n].g[2k-n] \tag{5.10}$$

$$y_{low}[k] = \sum_n x[n].h[2k-n] \tag{5.11}$$

After all the decompositions, the DWT of the input signal $x[n]$ is obtained by concatenating all coefficients from the last level of decomposition. The prominent frequencies in the original signal will appear as high amplitudes in that region of DWT. If the main information of the signal is in the high frequencies, narrower windows are appropriate, which results better time (or space) resolution. If the main information of the signal is in the low frequencies, wider windows are appropriate to result better frequency resolution.

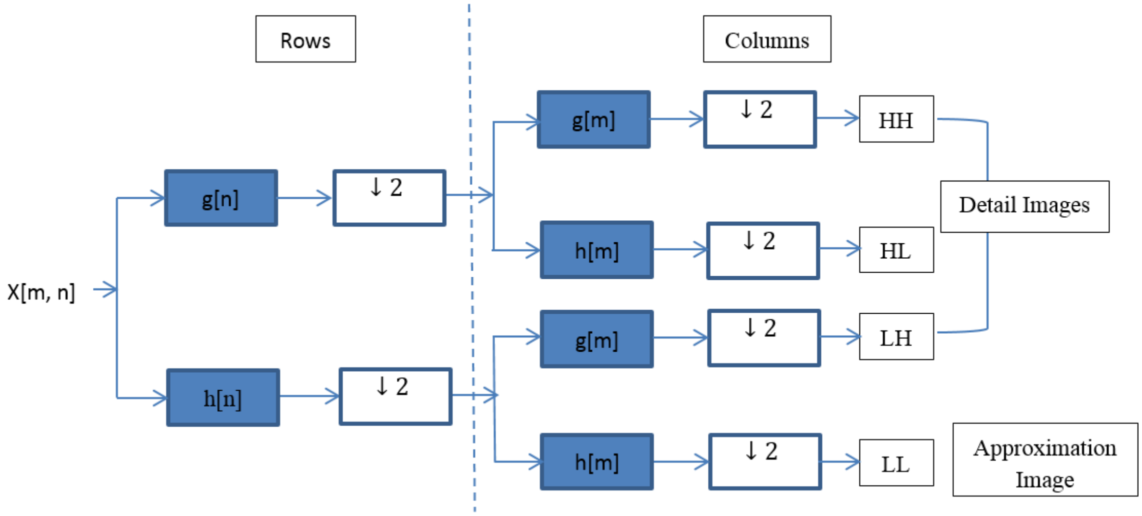

Figure 5.4 Schematic diagram of one-level 2-Dimensional DWT image decomposition process

### 5.2.3 Grey Level Co-Occurrence Matrix (GLCM) Features

GLCM is a classical second order statistical tool and is very useful for characterizing the texture features. GLCM-based texture feature extraction has been a popular method in remotely sensed images. It describes the texture of images based on how frequently two grey levels appear according to a position operator within an image. This technique is very effective because it compares the joint probability of the grey levels from pairs of pixels along a given distance and direction. . Because of this, GLCM is able to measure positional information as well as standard statistics such as mean and variance. The combination of these two types of information enables GLCM to distinguish a very wide variety of textures. The standard algorithm for GLCM is

(1) quantize the image (this reduces the number of gray levels in the image, which allows a smaller co-occurrence matrix to be used later); (2) extract a region of interest from the image to get a local texture measurement; (3) compute the co-occurrence matrix on the region of interest by using the given position operator; and (4) compute the feature with a mathematical formula that uses the co-occurrence matrix as input. The GLCM features are extracted from four spatial orientations: horizontal, left diagonal, vertical, and right diagonal corresponding to 0°, 45°, 90°, and 135°, and six features have been computed on each matrix. The features computed in this study are: energy, correlation, variance, homogeneity, entropy, and inertia which are tabulated in Table 5.1. Experiments were conducted with different block size windows (5x5, 7x7, 9x9, 11x11, and 13x13), and the classifiers are trained and tested with this extracted feature data, and the performance has been evaluated.

Table 5.1 GLCM Feature Calculation

| | |
|---|---|
| Contrast | $\sum_i \sum_j P_{ij}(i-j)^2$ |
| Entropy | $-\sum_i \sum_j P_{ij} \log P_{ij}$ |
| Correlation | $\sum_i \sum_j \frac{(i-\mu)(j-\mu)P_{ij}}{\sigma^2}$ |
| Energy | $\sum_i \sum_j P_{ij}^2$ |
| Homogeneity | $\sum_i \sum_j \frac{P_{ij}}{1+(i-j)^2}$ |
| Variance | $\sum_i (i-\mu^2) \sum_j P_{ij}$ |
| Here, $P_{i,j}$ represents the value of the element of GLCM at the coordinate$(i,j)$, $\mu = \sum_i \sum_j P_{i,j}$, and $\sigma^2$ is the variance. | |

## 5.3 Radar Data Classification

### 5.3.1 Unsupervised Classification - RX Anomaly Detector

Recently, anomaly detection has become an important application for target detection. Detecting anomalies in the radar imagery necessitates the task of locating pixels with spectral signatures that are significantly different from the background. Reed and Yu developed a method referred to as the RX detector [10], which has shown success in anomaly detection of multispectral and hyperspectral data [11]. The RX detector is often presented as a benchmark for anomaly detection by finding targets that have spectrally different signatures from their surroundings. RX Anomaly detector, a training–free unsupervised classification scheme, typically detects signatures that are distinct from the surroundings with no prior knowledge. These unsupervised techniques are very fast and do not depend on ground truth information, so these results can guide levee managers to investigate the areas shown as anomalies in the classification map.

Essentially, the algorithm uses the covariance matrix, which calculates the Mahalanobis distance from the test pixels to the mean of the background pixels. In multidimensional space, the well-known Mahalanobis distance is used to identify pixels that lie far from the mean. Suppose L is the number of spectral bands and r is an Lx1-column pixel spectral vector of the image, then the RX detector (RXD) implements a filter specified by:

$$\delta_{RXD}(r) = (r-\mu)^T K_{LxL}^{-1}(r-\mu) \tag{5.12}$$

where μ is the global sample mean of the image subset (the mean of each spectral band) and $K_{LxL}$ is the sample covariance matrix of the image.

### 5.3.2 Supervised Classification

#### 5.3.2.1 Support Vector Machine (SVM) Classification

Support vector machine (SVM) is a state-of-the-art classification method introduced by Vapnik [12] [13]. It is a powerful supervised learning method for analyzing and recognizing patterns. SVMs discriminate two classes by fitting an optimal separating hyperplane to the training data within a kernel-induced feature space. A nonlinear kernel function in the SVM framework helps to map nonlinear separation in the original space to a linear separation in the kernel-induced feature space. A classification problem with n classes will be divided into several binary sub-problems. The basic concept of support vector machines for a linearly non-separable case aims at the definition of a separating hyperplane in a multi-dimensional feature space that maximizes the marginal distance from the nearest support vector of each class. The multi-dimensional feature space is mapped by a kernel function, in which all the computations are done in the original feature space [14] [15] [16]. The redistributed data enable the fitting of a linear hyperplane between the training samples of two classes. The SVM training requires the estimation of the kernel parameter and the regularization parameter. These parameters are usually determined by a grid search by testing possible combinations. Suppose we have *l* observations, and each observation consist of a pair: a vector $x_i \in R^n$, $i = 1, \ldots, l$ and the associated truth is $y_i$.

Figure 5.5 shows the linear separating hyperplane for the separable case, and the solid circle and squares on the margin are called support vectors.

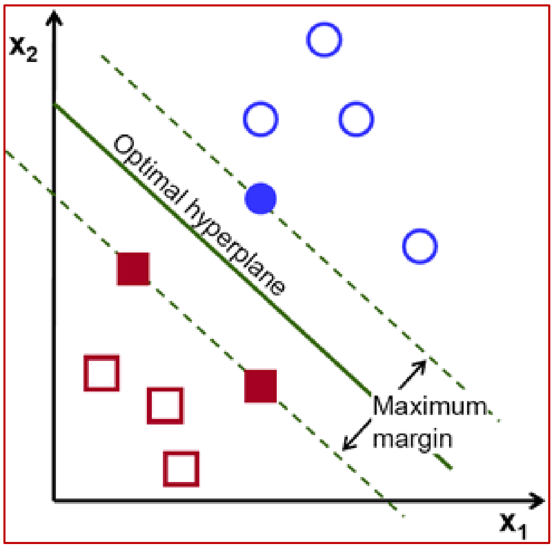

Figure 5.5 SVM hyperplane with samples from two classes

The advantage of SVM is that it works well with small training datasets. The kernel function plays a critical role in the SVM training and classification [17]. The idea of a kernel function is to enable operations to be performed in the input space rather than the high dimensional feature space. Some commonly implemented kernel functions are the linear kernel, polynomial kernel, and the Gaussian radial basis function (RBF) kernel. The SVM has another set of parameters called hyperparameters and these are soft margin constant 'C' and the width of the Gaussian kernel γ ($1/2\sigma^2$) or degree of the polynomial kernel.

The RBF with a Gaussian form is given as

$$K(x_i, x_j) = \exp\left(-\frac{\| x_i - x_j \|^2}{2\sigma^2}\right) \tag{5.13}$$

where σ is a width parameter characterizing the RBF. The value of σ has an impact on the generalization ability in the kernel induced space. Therefore, as the value of σ increases, the generalization ability in the kernel based system increases.

In this method, the input data are first transformed into a feature space (possibly with a higher dimension than the original data) either linearly or non-linearly based on a kernel function. Next, a hyperplane that separates the classes is computed by applying an optimization method.

#### 5.3.2.2 k-Nearest Neighbor (k-NN) Classifier

*k*-NN is one of the simplest but widely used machine learning algorithms. This algorithm is a straight forward extension of nearest the neighbor (NN) classifier. Instead of using one sample closest to the testing point, the *k*-NN classifier chooses the *k* nearest samples from training data X. The *k*-nearest neighbor query starts at the test point $x_o$ and grows a spherical region until it encloses *k* training samples. The classifier finds the set of *k* nearest neighbors in the training set to $x_o$ and then classifies $x_o$ as the most frequent class among the *k* neighbors. Consider a dataset with training samples $X = \{x_i\}_{i=1}^{n}$ in *d*-dimensional feature space $R^d$ and class labels $\omega_i \in \{1, 2, \ldots, C\}$, where *C* is the number of classes, and *n* is the total number of training samples. Commonly, Euclidean distance is used to compute the distance measure between training sample $x_i$ and given testing sample.

Consider the outcome of *k*-NN based on 1 nearest neighbor for the example shown in Figure 5.6. In this case, *k*-NN will predict the test sample (red circle) with '+' as it is closer to it. The Euclidean distance is used to compute the distance between training sample and the given testing sample. When $k = 2$, *k*-NN will not be able to classify the outcome of the testing sample since the second closest sample is a '-', and both the plus and minus signs achieve the same score. If $k = 5$, the test sample is classified as '-' as there are 3 minus signs closest to the testing sample.

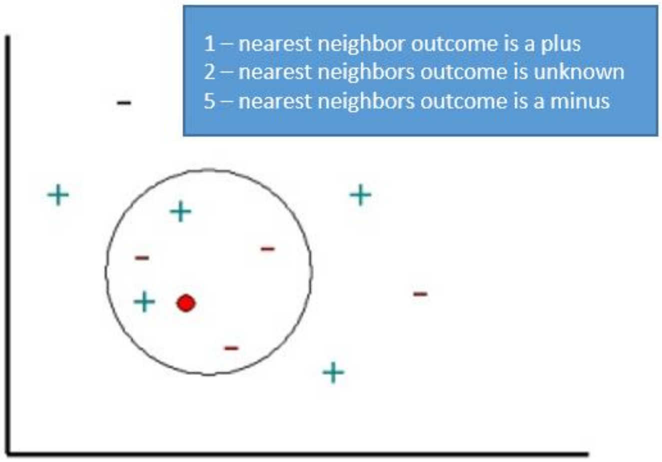

Figure 5.6 k-NN classification approach

In this research the k-NN algorithm was tested with multiple *k* values and the results were compared with SVM classifier.

## 5.4 References

1. J. J. Van Zyl, Howard A. Zebker, and Charles Elachi, “Imaging radar polarization signatures: Theory and observation”, Radio Science, vol. 22, no. 4, pp. 529 -543, 1987.

2. Shane Robert Cloude and Eric Pottier, “An entropy based classification scheme for land applications of polarimetric SAR”, IEEE Transactions on Geoscience and Remote Sensing, vol. 35, No. 1, 1997.

3. Shane Robert Cloude and Eric Pottier, “A review of target decomposition theorems in radar polarimetry”, IEEE Transactions on Geoscience and Remote Sensing, vol. 34, No. 2, 1996.

4. Polsarpro manual, “Single vs multi-polarization descriptors,“ http://earth.eo.esa.int/polsarpro/Manuals/3_Single_vs_multi-polarization_descriptors.pdf

5. Jong-Sen Lee and Eric Pottier, “Polarimetric radar imaging from basics to applications”, CRC press, 2009, pp 238.

6. J.S. Lee, M.R. Grunes, T.L. Ainsworth, L. Du, D.L. Schuler, and S.R. Cloude, “Unsupervised classification using polarimetric decomposition and complex Wishart classifier”, IEEE, 1998.

7. Thomas Jagdhuber, Julia Stockamp, Irena Hajnsek, and Ralf Ludwig, “Identification of soil freezing and thawing states using SAR polarimetry at C-band,” Remote Sensing, 6(3), 2008 – 2023, doi: 10.3390/rs6032008, 2014.

8. S. C. Burrus, R. A. Gopinath, and H. Guo, Introduction to wavelets and wavelet transforms: A primer, Prentice-Hall, 1997.

9. Chun-Lin, and Liu, “A tutorial of the wavelet transform,” 2010.

10. X. Yu, L. E. Hoff, I. S. Reed, A. M. Chen, and L. B. Stotts, “Automatic target detection and recognition in multispectral imagery,” IEEE Transactions Image Processing, Vol. 6, pp. 143 – 156, January 1997.

11. Chein-I Chang, and Shao-Shan Chiang, “Anomaly detection and classification for hyperspectral imagery”, IEEE Transactions on Geoscience and Remote Sensing, Vol. 40, No. 6, June 2002.

12. V. Vapnik. The Nature of Statistical Learning Theory. Springer-Verlag, New York, 1995.

13. V. Vapnik. Statistical Learning Theory. John Wiley and Sons, Inc., New York, 1998.

14. Gustavo Camps-Valls, and Lorenzo Bruzzone, “Kernel-Based methods for hyperspectral image classification”, IEEE Transactions on Geoscience and Remote Sensing, vol. 43, no. 6, 2005.

15. Bjorn Waske, Jon Atli Benediktsson, Kolbeinn Arnason, and Johannes R. Sveinsson, “Mapping of hyperspectral AVIRIS data using machine-learning algorithms,” Can. J. Remote Sensing, vol. 35, suppl. 1, pp. S106 – S116, 2009.

16. C. Huang, L. S. Davis, and J. R. G. Townshend, “An assessment of support vector machines for land cover classification,” Int. J. Remote Sensing, 2002, no.4, vol. 23, pp. 725-749.

17. Christopher J.C. Burges, A Tutorial on Support Vector Machines for Pattern Recognition, Data Mining and Knowledge Discovery 2, 121-167, 1998.

## CHAPTER VI

## EXPERIMENTAL RESULTS AND ANALYSIS

### 6.1 RX Anomaly Detector Classification Results

RX Anomaly detector, a training–free unsupervised classification scheme typically detects signatures that are distinct from the surroundings with no prior knowledge. These unsupervised techniques are very fast and do not depend on ground truth information, so these results guide levee managers to investigate the areas shown as anomalies in the classification map.

Surface roughness is an important property that can be used to distinguish slump slides as the radar backscatter is strongly influenced by the surface roughness. Therefore, textural features derived from Synthetic Aperture Radar imagery using the discrete wavelet transform (DWT) technique have been used in the classification tasks. The main parameters to be considered in DWT feature extraction include the choice of mother wavelet function, and the neighborhood window size. For the levee application, the classification algorithms were tested with different mother wavelets and window sizes. The Daubechies mother wavelet with a window size of 4 and one decomposition level from each of the radar polarization channels gave the best performance, so these features were used as inputs to the classifiers.

### 6.1.1 UAVSAR June 2009 Image Classification

In this study, a 7.7 km length subset of UAVSAR image acquired on June 16, 2009 was used in the analysis and the georeferenced layers used in the analyses have been masked by a 40 meter buffer from the crown of the levee on the river side. The important factors that affect the radar backscatter intensity are the radar frequency, polarization, and incidence angle. The incidence angle of the UAVSAR data varies from 25° - 60° across the image swath. The variations in incidence angle affect the radar backscatter, so the study area with constant levee orientation was analyzed in this work. In this study area, a total of 10 slump slides and 2 stability berms were present and labeled with numbers 14 to 25. The geographic locations of these are marked as black and green circles overlaid on the NAIP optical image as shown in Figure 6.1. The area located to the south of slide 24, marked with a solid green circle, was identified as a slide in 2013 by the Mississippi Levee Board. At the time of image acquisition, five of these slides were active: slide 20, 21, 23, 24, and 25. These are highlighted in red in the ground truth Table 6.1, created from data obtained from the levee board.

The RX Detector (RXD) unsupervised classification algorithm was implemented on the extracted features of the SAR data. The output generated by RXD is a grayscale image; the larger the value of the pixels, the more anomalous the pixels would be. For visualization purposes, the range of values of the output are color-coded. Based on the available field data and field visits, the location of the slides were known before the classifier detected as an anomaly. The results show that the classifier was able to identify the slide locations since the pixels in that area had higher values of the normalized Mahalanobis distance.

The scatter plot in Figure 6.2 shows the classifier output which is the normalized Mahalanobis distance values to see the distribution. There were some outliers which have very high Mahalanobis distance values, and from the NAIP image it is clear that these are due to trees on the levee as shown in Figure 6.3. To find a threshold value to detect the slump slides, a histogram for a narrower range of Mahalanobis distance values (within a range of 0.001 – 0.002) was plotted as shown in Figure 6.4. Various threshold values were examined with the goal of maximizing the percentage of true positives (slide pixels) and minimizing the percentage of false positives. The threshold is used to identify the true positives which are the slide pixels. The threshold value depends on the length of the levee segment and the width of the levee buffer. A threshold of 0.0019 was chosen and the pixel values greater than this threshold were considered to be classified as slide pixels and the rest as healthy levee pixels. This resulted in over 90% true positives and less than 30% false positives. The classification map of RX Detector output is color-coded with a range of values as shown in Figure 6.1. The pixels with values greater than the threshold are color coded in blue. The slide dimensions were provided by the Mississippi Levee Board and from the results, it is obvious that the shape of the slides were clearly distinguishable from the healthy levee area. The results also show that there were some false positives to the north of Slide 16, which could be due to the radar shadows of the trees on the toe of the levee. Figure 6.5 shows the enlarged view of the classification output for the area around active slides 20 and 21. From this output, we see some false positives located where a new slide (slide 17) later appeared (in October 2009). The cluster of false positives shown in Figure 6.6 near slide 22 also later became a slump slide in September 2009. In addition, some false positive pixels seen to the south of slide 24 and showed new slide activity in 2013. This location is marked with a solid green circle in Figure 6.7.

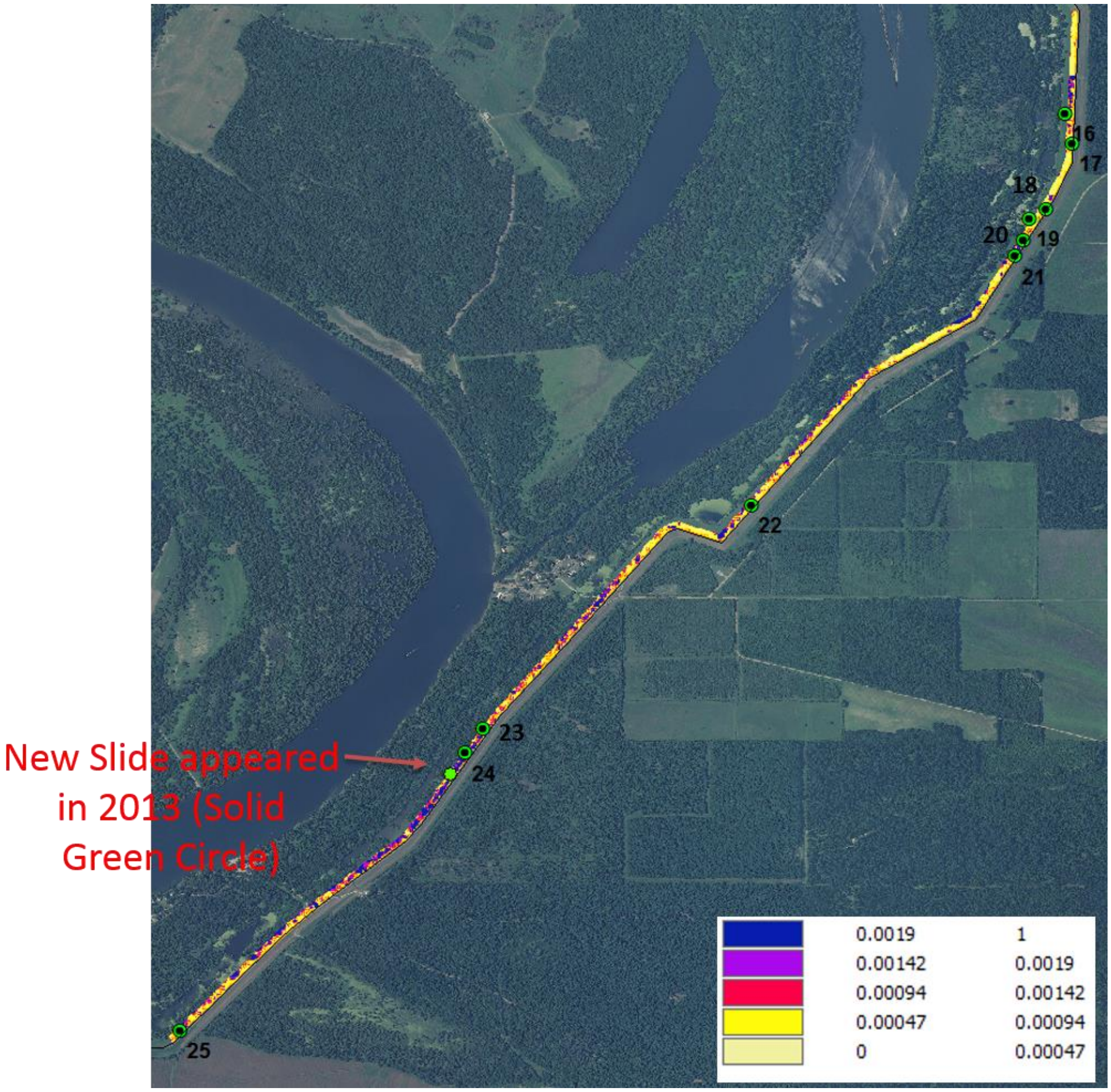

Figure 6.1 2009 NAIP optical imagery with locations of known slump slides 16 – 25 and the anomaly detector output on the foreground.

Table 6.1 Slide Ground Truth Data from Mississippi Levee Board, with slides active at the time of the 2009 radar image highlighted in red

| Slide # (arcGIS FID) | | | From Levee Board (08Apr2011) | | Slide Measurements | | | |
|---|---|---|---|---|---|---|---|---|
| | Latitude (North) | Longitude (West) | Date Slide Appeared | Date Slide Repaired | Length | Vert. Face | Distance from crown | Notes |
| 14 | N32-37'-37.2" | W90-59'-56.2" | Oct-09 | Nov-09 | 230' | 7' | 9' | |
| 15 | N32-37'-28.2" | W90-59'-49.8" | 21-Oct-09 | Apr-10 | 190' | 1.5' | 120' | |
| 16 | N32-36'-55.4" | W90-59'-38.8" | Stability Berm | | 110' | 2' | 135' | RS Stability Berm |
| 17 | N32-36'-49.9" | W90-59'-37.3" | 21-Oct-09 | Nov-09 | 165' | 2' | 15' | |
| 18 | N32-36'-37.7" | W90-59'-42.3" | 21-Oct-09 | Nov-09 | 80' | 2' | 30' | |
| 19 | N32-36'-36.0" | W90-59'-45.2" | Stability Berm | | 90' | 2' | 140' | RS Stability Berm |
| 20 | N32-36'-32.0" | W90-59'-46.3" | Aug-08 | Nov-09 | 120' | 3' | 15' | |
| 21 | N32-36'-29.1" | W90-59'-48.0" | | Sep-10 | 200' | 8' | 8' | |
| 22 | N32-35'-43.4" | W91-00'-36.5" | Sep-09 | Apr-10 | 50' | 1' | 94' | Riverside Ramp |
| 23 | N32-35'-02.4" | W91-01'-25.7" | | Sep-10 | 70' | 1' | 100' | |
| 24 | N32-34'-57.9" | W91-01'-29.0" | | Sep-10 | 80' | 2' | 100' | |
| 25 | N32-34'-06.9" | W91-02'-21.6" | Feb-09 | Sep-10 | 125' | 3' | 20' | |

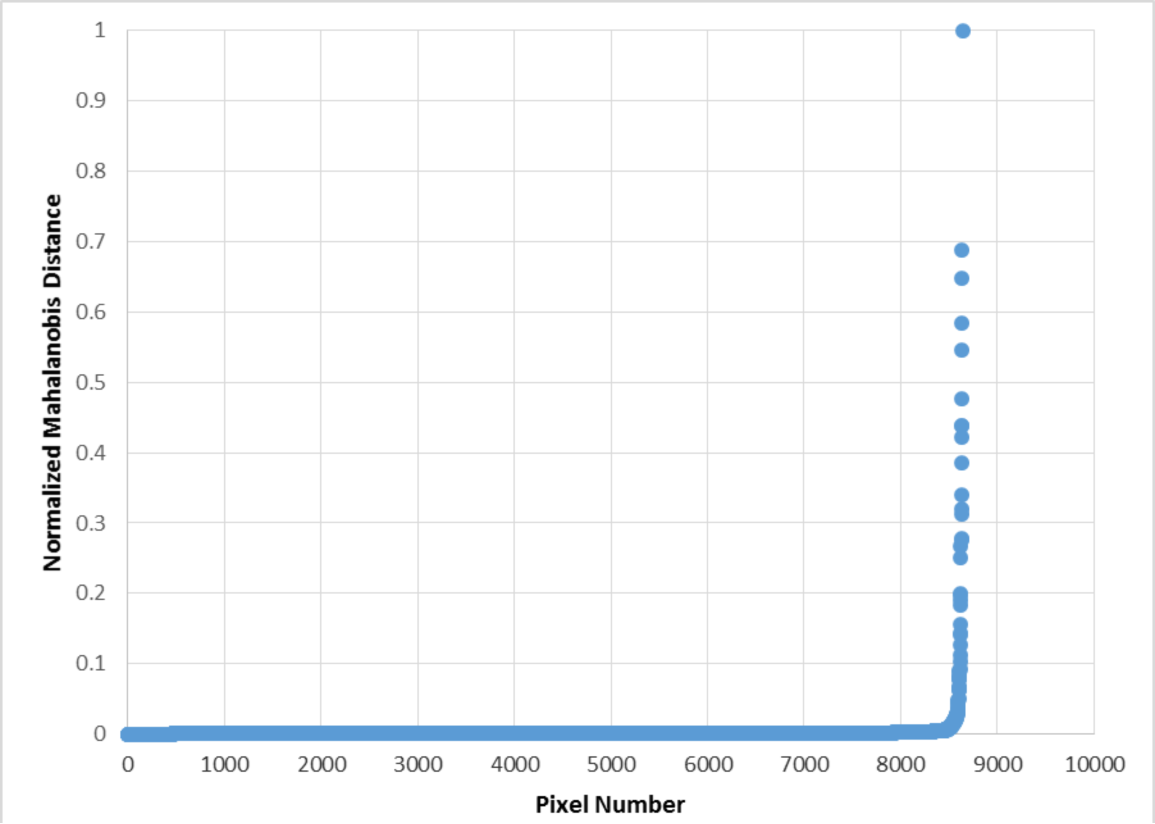

Figure 6.2 Scatter plot of the RX anomaly detector output, which is the normalized Mahalanobis distance, for UAVSAR 2009 image.

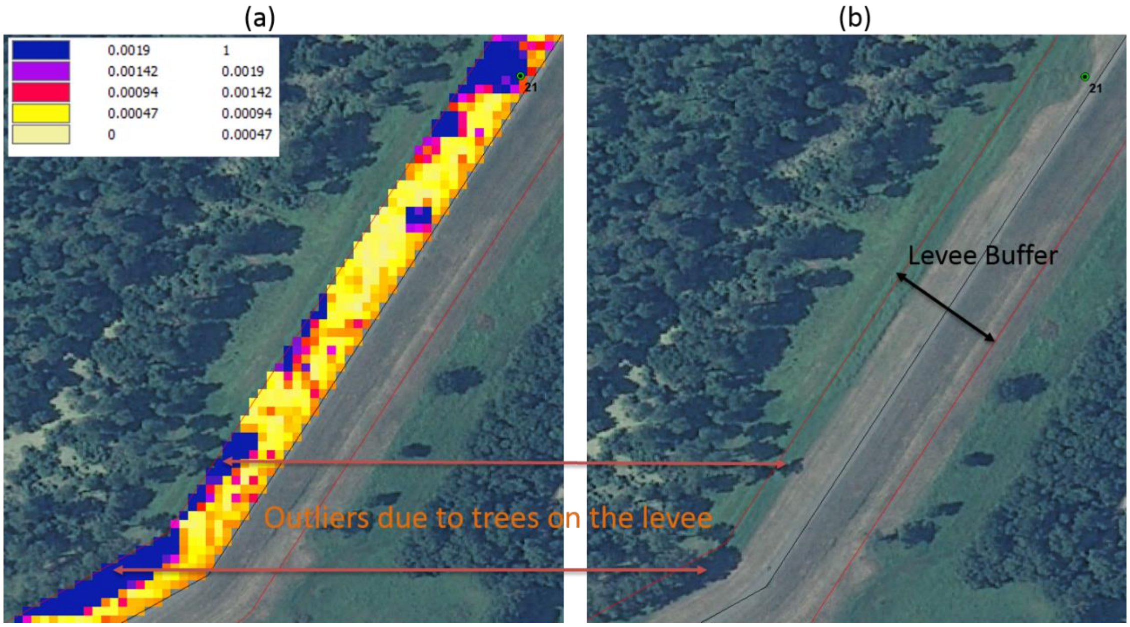

Figure 6.3 (a) Outliers in the RX Detector output due to trees on the levee, which have higher Mahalanobis distance values that are very different from the rest of the levee (b) NAIP optical image of the study area subset.

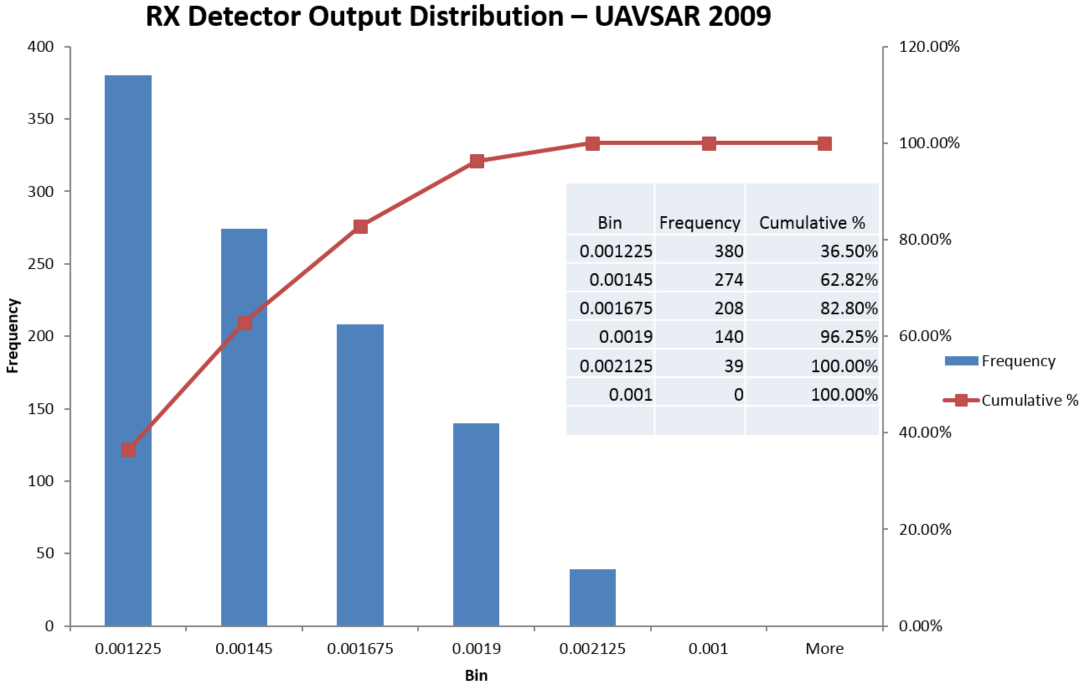

| Bin | Frequency | Cumulative % |
|---|---|---|
| 0.001225 | 380 | 36.50% |
| 0.00145 | 274 | 62.82% |
| 0.001675 | 208 | 82.80% |
| 0.0019 | 140 | 96.25% |
| 0.002125 | 39 | 100.00% |
| 0.001 | 0 | 100.00% |

Figure 6.4 Histogram of the normalized RX Detector classification output for UAVSAR 2009 image

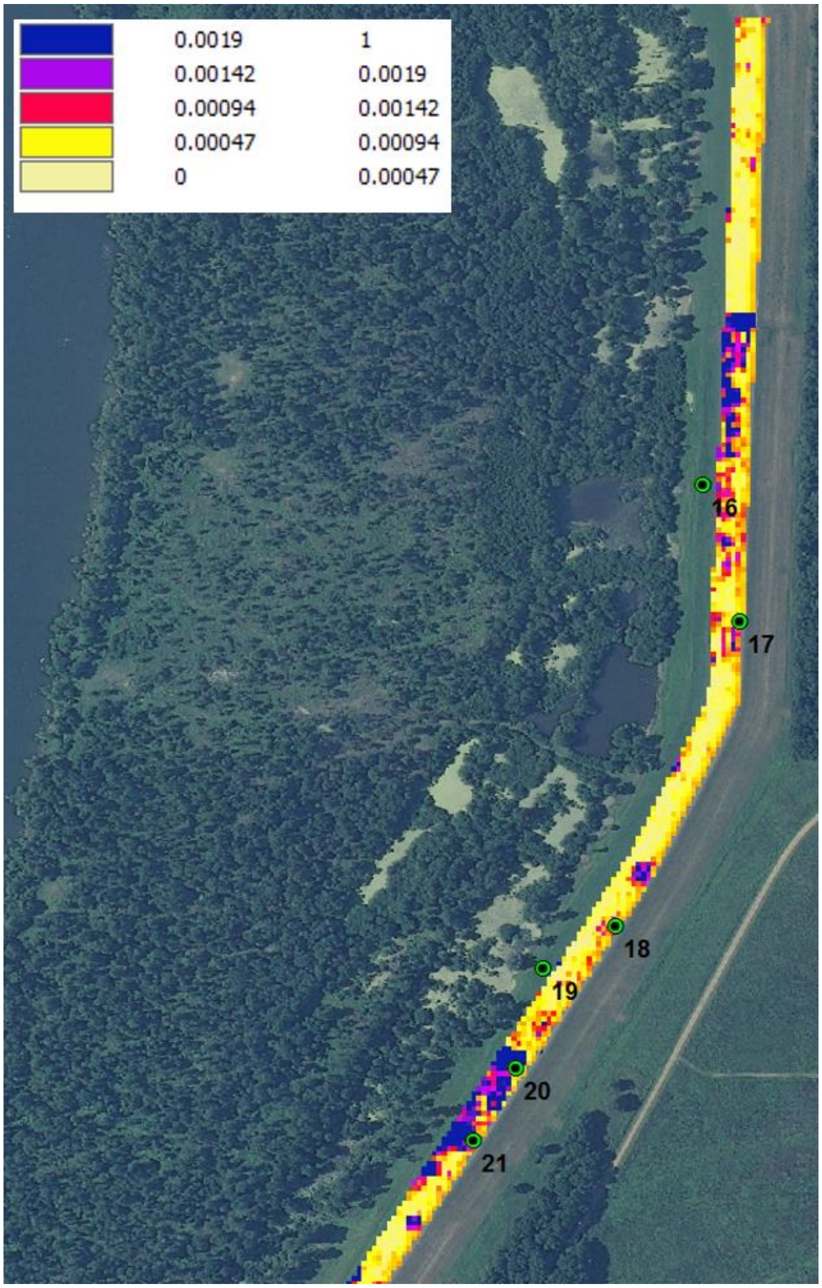

Figure 6.5 RX Anomaly detector classification output for active slides 20 – 21 at the time of UAVSAR image acquisition on 16 June 2009.

The pixels labeled as slides based on the selected threshold are blue in color. Slides 17 and 18 were appeared in October 2009, after the image date.

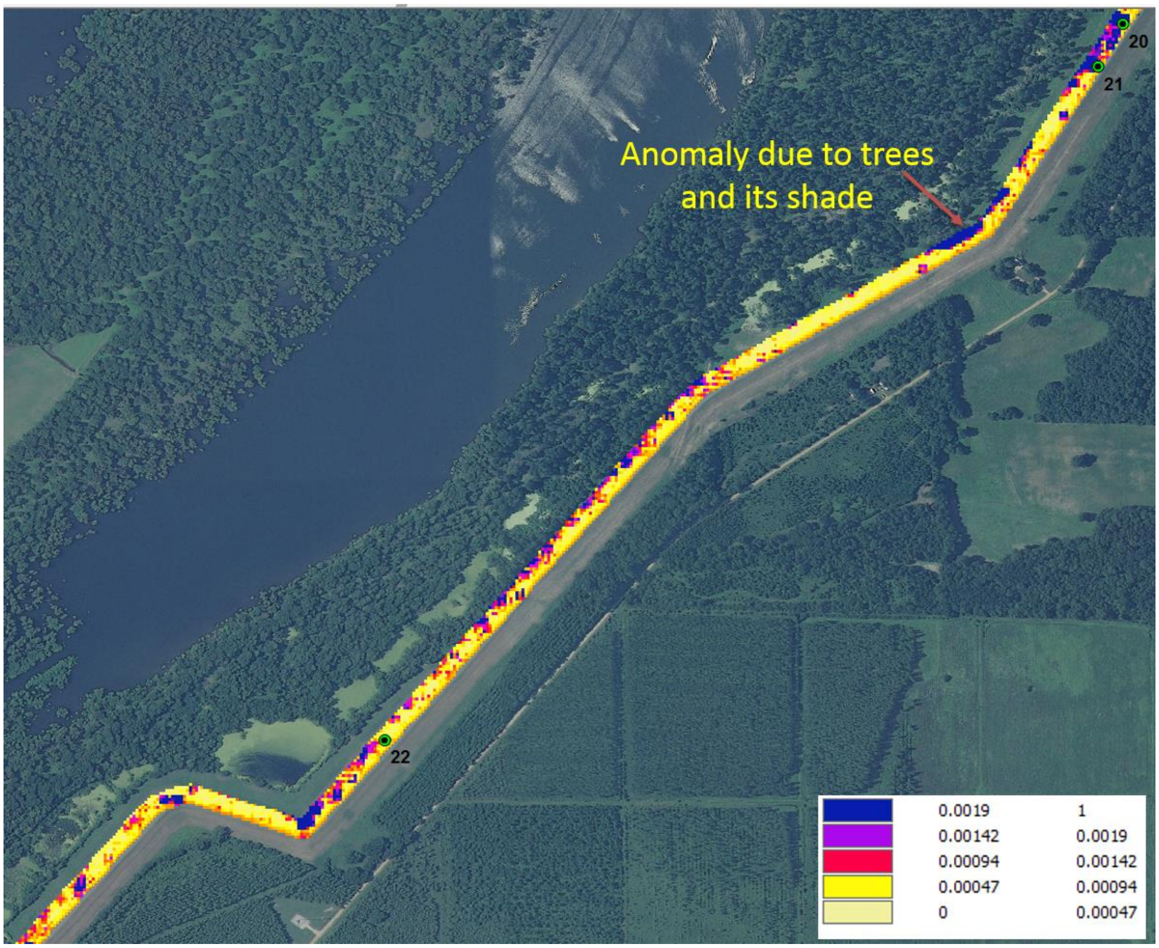

Figure 6.6 RX Anomaly detector classification output for middle part of the levee segment which cover slides 20 -22.

Slide 22 appeared in September 2009, after the UAVSAR image date 16 June 2009.

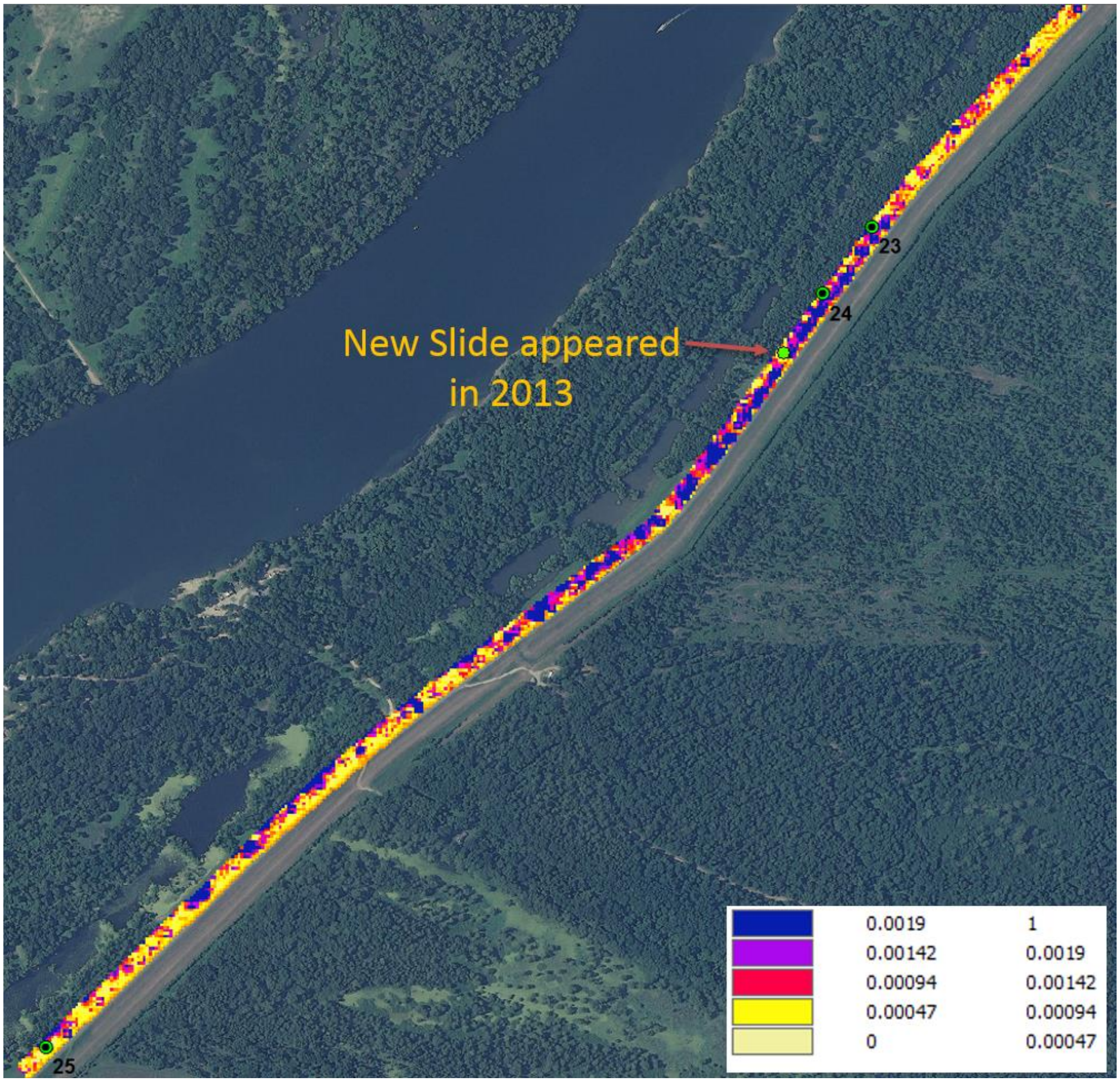

Figure 6.7 Lower part of the levee segment which contain three slides (23 – 25) active at the time of image acquisition on 16 June 2009.

A new slide appeared later at a location flagged as anomalous during the 2009 image analysis.

### 6.1.2 UAVSAR January 2010 Image Classification

After the 16 June 2009 radar image acquisition, UAVSAR flew over the Mississippi River levees on 25 January, 2010. To further analyze the performance of the anomaly detector algorithm, a 3.2 km length subset was used. Over this study area, a total of 6 slump slides and 2 stability berms were present and these were labeled with numbers 14 to 21. At the time of image acquisition there were two unrepaired slides, numbered 15 and 21, and all other slides were repaired. The RX detector unsupervised classifier algorithm was implemented and a histogram for the normalized Mahalanobis values was plotted to see the distribution. Based on the available ground truth data the location of the slides were known and a threshold has been chosen to identify the slide pixels from the classified output. A threshold of 0.004 was chosen which resulted in over 90% true positives and less than 20% false positives. The classifier output is shown in Figure 6.8. A small number of slide pixels were found at repaired slides -- especially at slides 20 and 14, and some other false positives north of slide 16. These false positives are associated with levee construction during the time of image acquisition as shown in Figure 6.9.

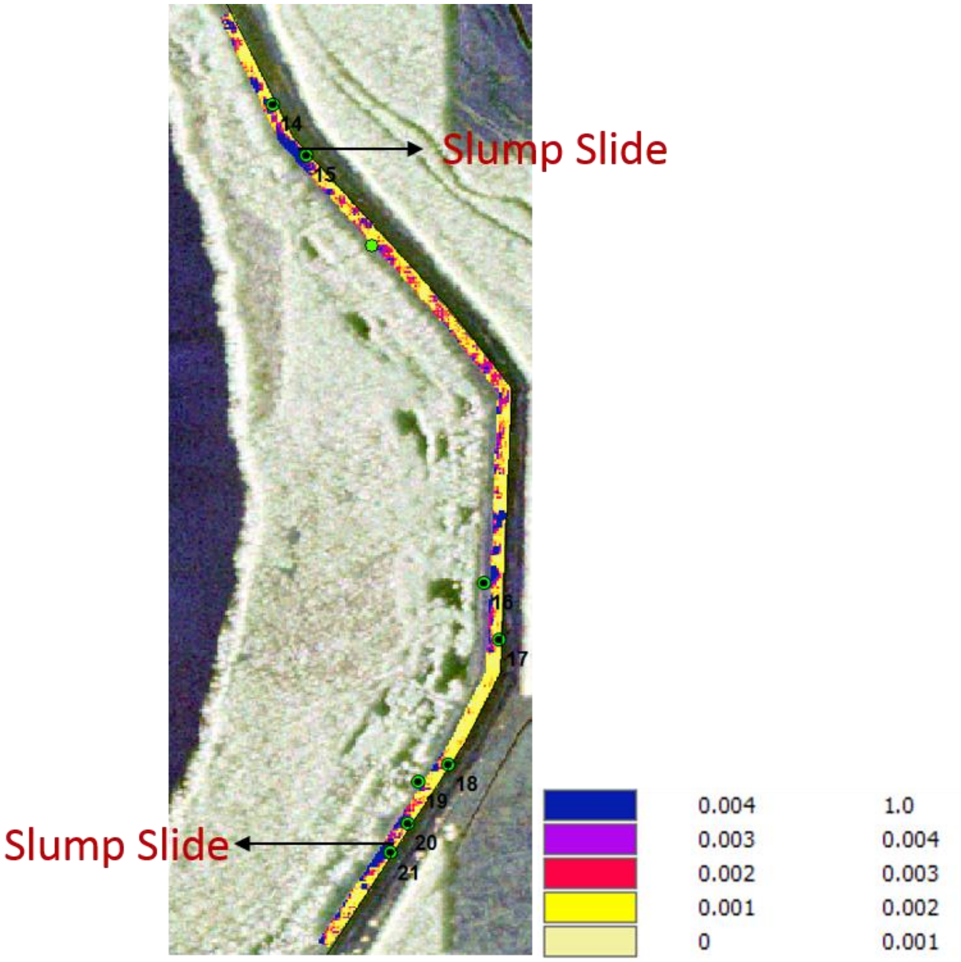

Figure 6.8 RX Anomaly detector classification map for 25 January 2010 UAVSAR image.

The two active slides were classified shown in bright blue color based on the threshold value.

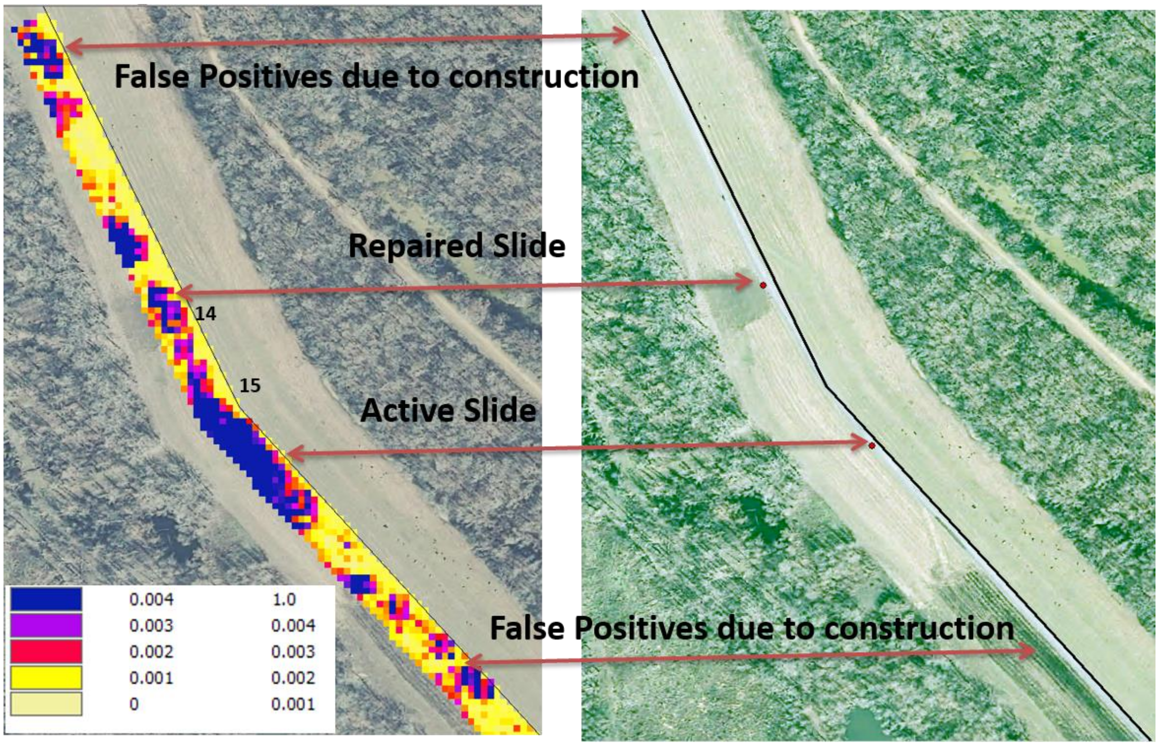

Figure 6.9 Classification output of 25th January 2010 UAVSAR image with NAIP optical imagery background which was used to confirm locations of active and repaired slides and also the construction areas on the levee

### 6.1.3 Impact of Polarization and Frequency on Anomaly Classification

In this study, the ability of each polarization channel in detecting the slump slides with different frequency bands of synthetic aperture radar data using the anomaly detection algorithm was investigated. The UAVSAR multi polarized, multi-look radar image acquired on 25 January, 2010 and the TerraSAR-X dual polarized high resolution spotlight imagery acquired on 15 September, 2010 were used in the analysis. By the time of both of these image acquisitions, there was one active slump slide (latitude: 32.5685, longitude: -91.0393) north of Vicksburg, Mississippi. A subset of 0.7 km long with this active slide was chosen as the area of analysis and the georeferenced layers used in the analyses were masked by a 40 meter buffer from the crown of the levee on the river side. The ground truth data was collected by the US Army Corp. of Engineers (USACE) and precise boundaries of the slump slide were mapped with polygons drawn using a GPS instrument during field data collection trips. The ground truth data contains the location and timing of slump slide appearance, dimensions of the slides, and their repair status. The spatial resolution for the UAVSAR and TerraSAR imagery are 5.5m and 1m respectively. In this study, the HH and VV backscattering behavior of the X-band and L-band radar backscatter in detecting the slump slide have been investigated.

The anomaly detection was performed by using each polarization channel of the SAR data separately and the performance was compared with that of using the stack of both polarizations. From the classifier output, which is the normalized Mahalanobis distance values, a threshold was chosen from histogram analysis to determine the slide pixels. There were some outliers which have very high Mahalanobis distance values, and from the NAIP image it is clear that these are due to trees on the levee. These outliers have distance values greater than 0.5 and were ignored in the plot of the histogram distribution shown in Figure 6.10. The threshold values within a range of 0.15 – 0.23 was chosen to identify the slump slide pixels and the distance values greater than 0.23 were identified as false positives. The classification map of the anomaly detector output for the UAVSAR image with each polarization channel data considered separately and together are shown in Figure 6.11 and the classification maps of the TerraSAR-X image are shown in Figure 6.12.

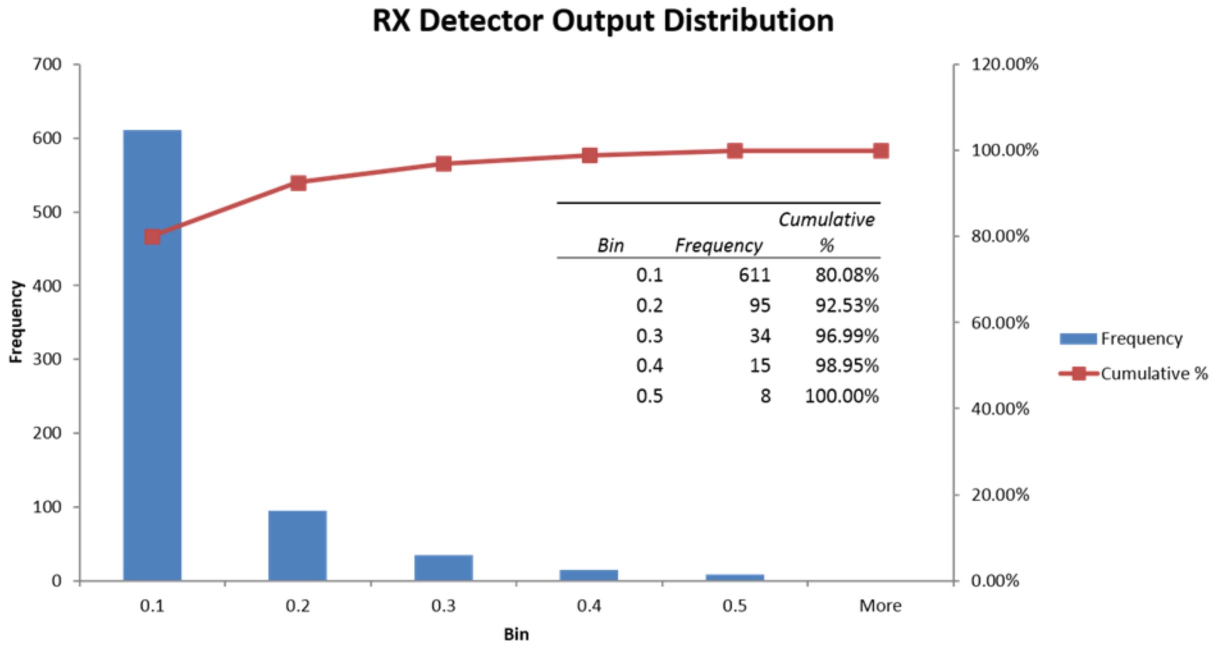

| Bin | Frequency | Cumulative % |
|---|---|---|
| 0.1 | 611 | 80.08% |
| 0.2 | 95 | 92.53% |
| 0.3 | 34 | 96.99% |
| 0.4 | 15 | 98.95% |
| 0.5 | 8 | 100.00% |

Figure 6.10 Histogram distribution of RX anomaly detector output for January 2010 L-band UAVSAR image subset.

The normalized Mahalanobis distance values greater than 0.5 were ignored due to outliers on the levee.

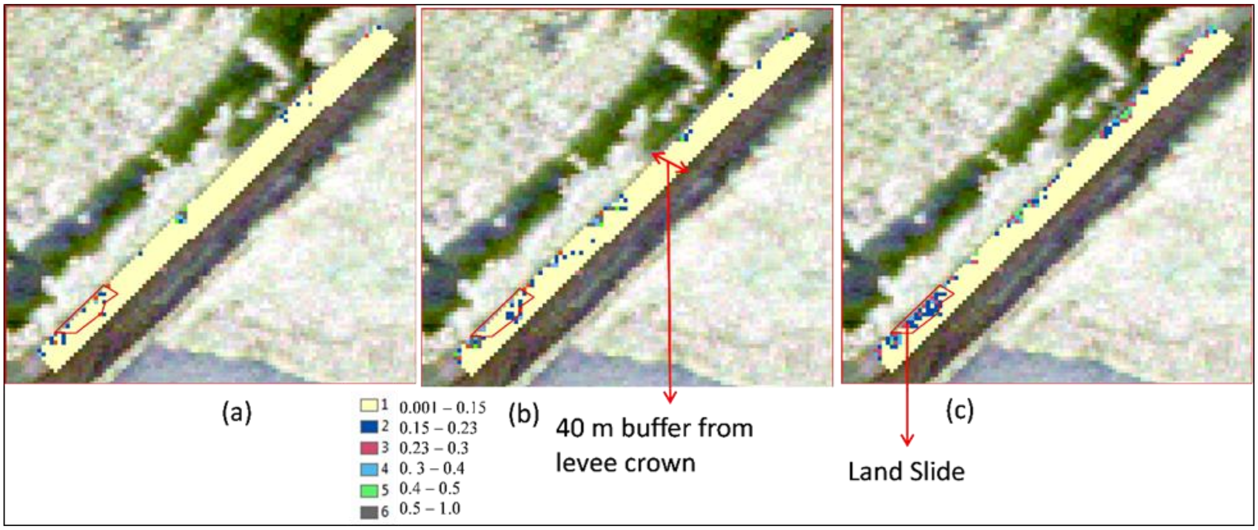

| | | |
|---|---|---|
| 🟨 | 1 | 0.001 – 0.15 |
| 🟦 | 2 | 0.15 – 0.23 |
| 🟥 | 3 | 0.23 – 0.3 |
| 🟦 | 4 | 0. 3 – 0.4 |
| 🟩 | 5 | 0.4 – 0.5 |
| ⬛ | 6 | 0.5 – 1.0 |

Figure 6.11 Classification map of RX anomaly detector results for L-band UAVSAR imagery:

(a) with HH polarization data, (b) with VV polarization data, and (c) with HH and VV polarization data

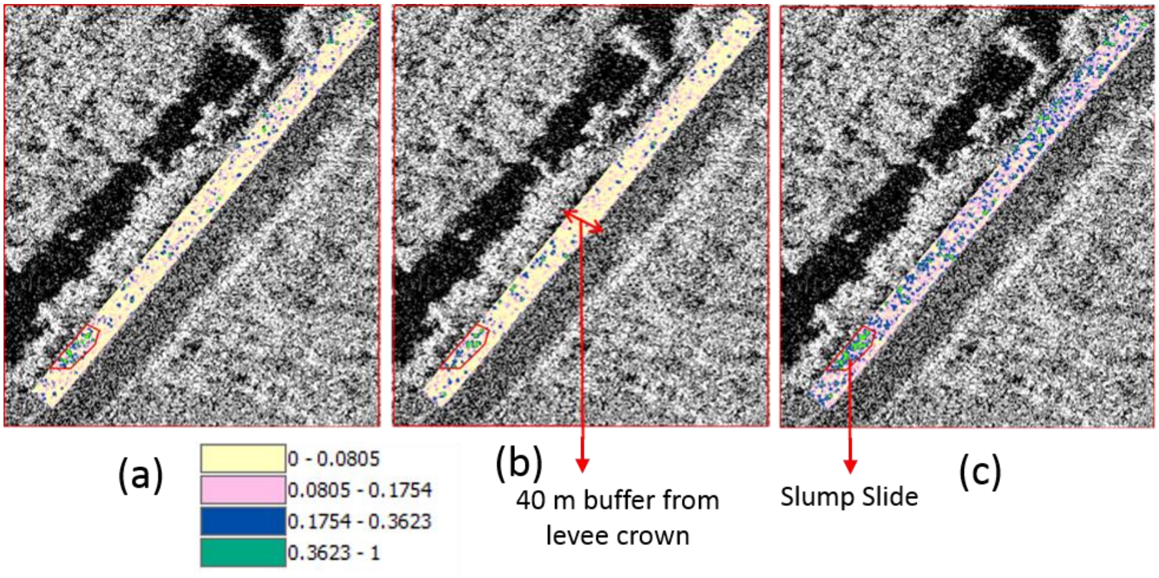

Figure 6.12 Classification map of RX anomaly detector results for X-band TerraSAR-X imagery:

(a) with HH polarization data, (b) with VV polarization data, and (c) with both HH and VV polarization data

The classification results show that the anomaly detector performed well when both polarizations were used in the classification analysis. The total number of slide pixels in the UAVSAR imagery is 44 with a pixel size of 5.5m x 5.5m. When both the HH and VV polarization data are used for the classification analysis, 21 pixels were classified as slump slide which gives an accuracy of 47.72%. However, when individual polarization data is considered in the analysis, the accuracy was 9% and 18% for the HH and VV polarizations respectively.

The total slump slide pixels in the TerraSAR-X subset are 1499 with a pixel size of 1m x 1m. As shown in Figure 6.12, a threshold of 0.3623 was chosen for the X-band anomaly output and the pixels greater than this threshold were considered as slide pixels. The anomaly output resulted in 337 pixels being classified as slide pixels when both HH and VV polarization data were used in the classification analysis which gives an accuracy of 22.4%. When the algorithm was implemented with individual polarization data, the accuracies were reduced to 11.27% and 8.33% for the HH and VV polarization data respectively.

The receiver operating characteristic (ROC) curves are generated by plotting the probability of detection (true positive rate) against the false positive rate to provide a quantitative performance comparison. The ROC curves are generated based on ground truth information about the slump slide location and dimensions. The precise boundaries of the slide were mapped with polygons drawn using a GPS instrument during filed data collection trips. Therefore, the number of slide pixels are known from the ground truth polygons. From the classifier’s output the true positives and the false positives are estimated and the ROC curves are generated based on this result. For example, if the classifier output is represented in terms of a confusion matrix as given in Table 6.2, the true positive rate and false positive rate will be computed as shown below.

Table 6.2 Confusion matrix for a binary classifier

| | Positive | Negative |
|---|---|---|
| Test Positive | TP (True Positive) | FP (False Positive) |
| Test Negative | FN (False Negative) | TN (True Negative) |

TP_rate (True Positive Rate) = Positives correctly classified (TP) / Total Positives

= TP / (TP + FN)

FP_rate (False Positive Rate) = False Positives (FP) / Total Negatives

= FP / (FP + TN)

The ROC curve is a metric used to check the quality of classifiers. It gives the probability of detection of slide pixels (True Positives Rate) against the false positive rate at various threshold values. The ground truth mask for the study area shown in Figure 6.13 has two classes: slump slide and healthy levee. The polygon in Figure 6.13 represents the slump slide area (mask value for this polygon = 1) and the area outside the polygon is the healthy levee area (mask value = 0). The normalized output of the RX anomaly detector (a row vector **r**) ranges in the interval [0, 1] and the threshold values ($\tau$) are applied across this interval to RX detector output. In this case, the anomaly map is defined as the area where mask = 1, and healthy levee map is defined as the area where mask = 0. For each threshold, FPR and TPR are calculated and plotted on x and y axis. The true positive rate and false positive rate are calculated as:

TP_rate = number of outputs greater than the threshold ($\mathbf{r} > \tau$) / number of 1 (slump slide) targets, and

FP_rate = number of outputs less than the threshold / number of 0 (healthy levee) targets

Figure 6.14 shows the ROC curve of the anomaly detector output for the UAVSAR image analysis, when both polarization channels (HH and VV) are considered together. Figure 6.15 shows the ROC curve of the anomaly detector output for the TerraSAR-X image analysis, when both the polarization channels (HH and VV) are used. The results show that the anomaly detector output from the dual-pol L-band UAVSAR outperformed the dual-pol X-band TerraSAR-X anomaly detection results.

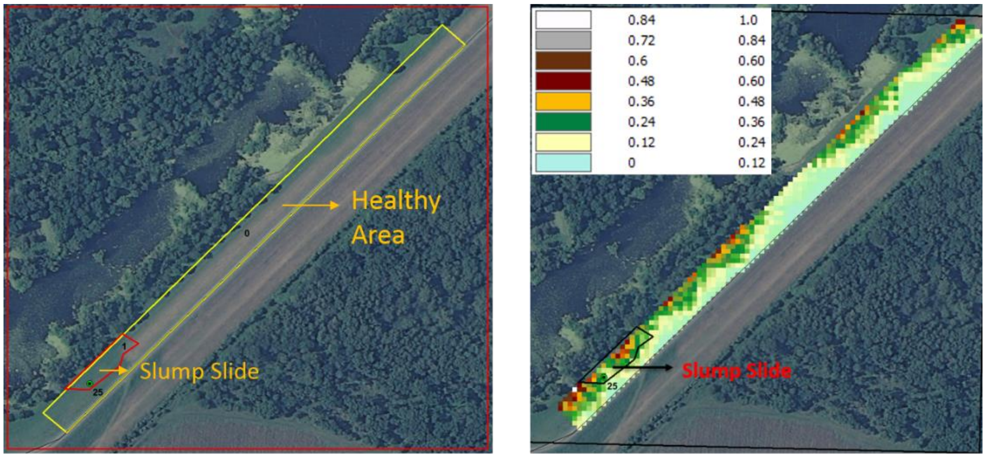

(a) (b)

Figure 6.13 (a) Ground truth mask with two classes: slump slide (mask = 1) and healthy levee (mask = 0) (b) RX Detector output for the image subset.

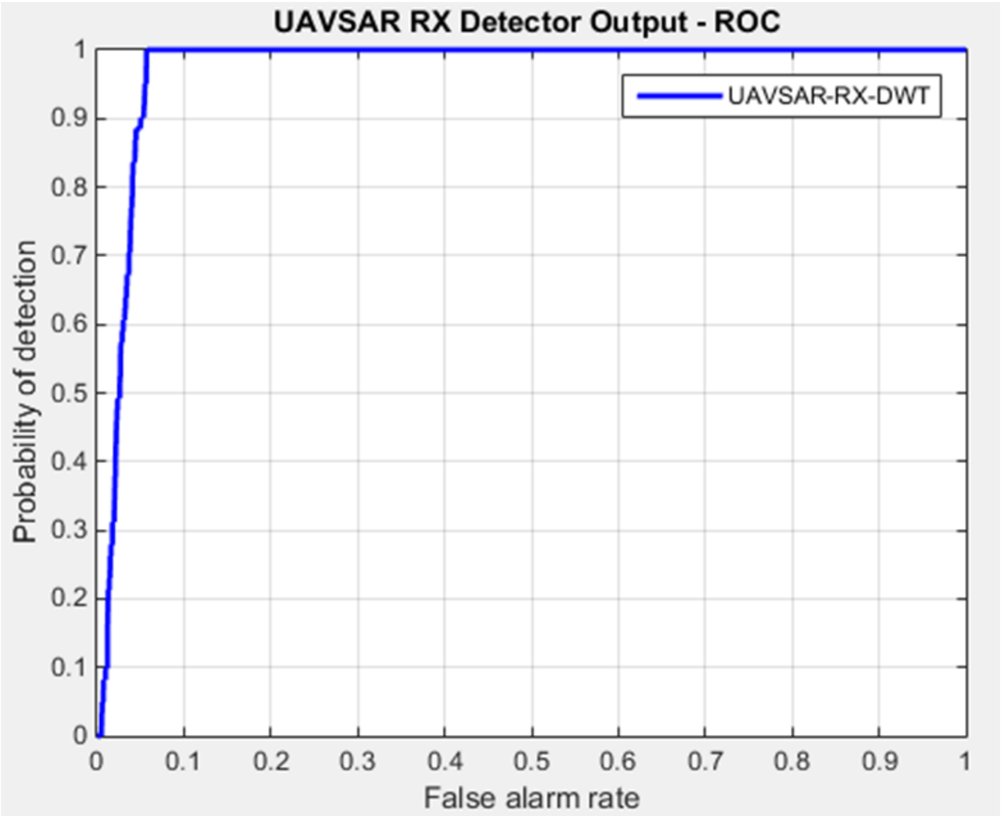

Figure 6.14 ROC curve of anomaly detector output for UAVSAR data for detecting the slump slide pixels.

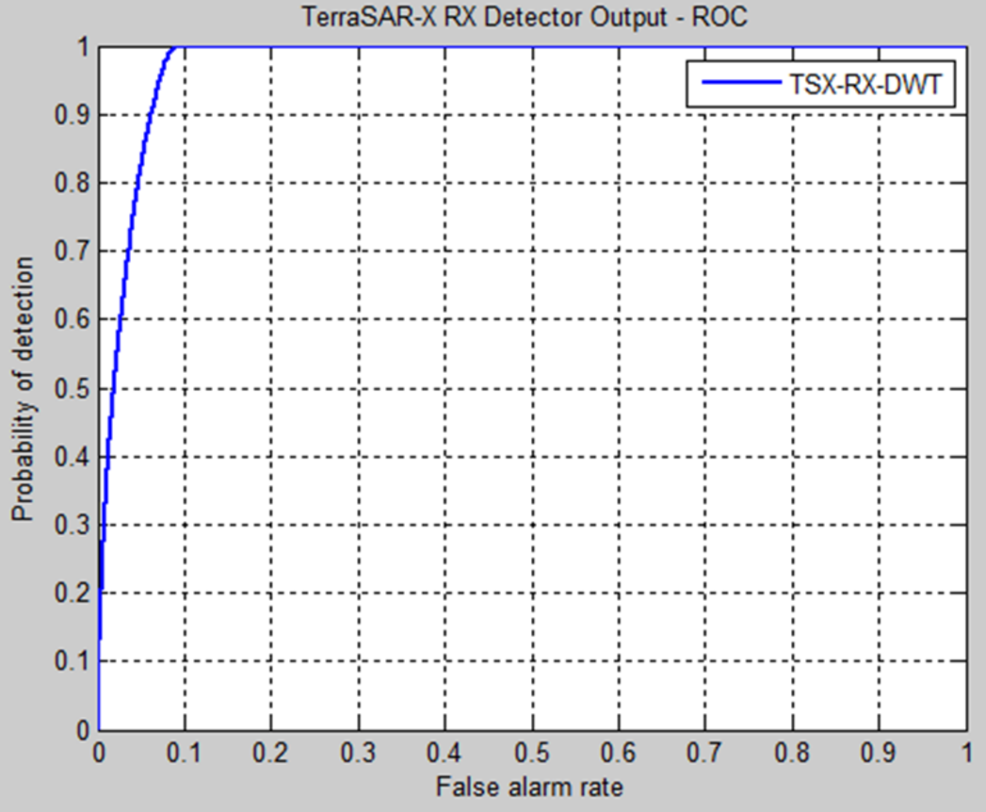

Figure 6.15 ROC curve of anomaly detector output for TERRASAR-X data for detecting the slump slide pixels.

## 6.2 Supervised Classification

This research analyzes the ability to detect slump slides on levees with Synthetic Aperture Radar (SAR) data using supervised machine learning algorithms. This study examines two of the most popular machine learning algorithms: k-nearest neighbor (k-NN) and support vector machines (SVM) to classify the radar imagery. In this study, a 1.1 km wide study area has been analyzed in detail with the described supervised learning methods. The discrete wavelet transform (DWT) and grey level co-occurrence matrix (GLCM) texture features extracted from the SAR backscattering coefficients HH, HV, and VV were used as feature data to the classifiers. For DWT based classification, the wavelet coefficients were computed from the SAR data with different window sizes. Other parameters considered include the choice of mother wavelet function and the neighborhood window size. The wavelet features, with one decomposition level from each of the radar polarization channels, were used in this study and the classifiers were tested with different wavelet window sizes. For GLCM based classification, the GLCM features are extracted from four spatial orientations: horizontal, left diagonal, vertical, and right diagonal corresponding to (0°, 45°, 90°, and 135°) and six features have been computed on each matrix. The features computed in this study are: energy, correlation, variance, homogeneity, entropy, and inertia. Experiments are done with different block / window sizes (5x5, 7x7, 9x9, 11x11, and 13x13), the classifiers were trained and tested with this extracted feature data, and the performance has been evaluated.

Our experimental results show that inclusion of textural features derived from the SAR data using discrete wavelet transform (DWT) features and grey level co-occurrence matrix (GLCM) features improved the overall classification accuracies.

### 6.2.1 Support Vector Machine (SVM) Classification with Discrete Wavelet Transform (DWT) features for UAVSAR 2-class subset

SVM, a nonparametric classification method, has been used successfully in remote sensing studies. The advantage of SVM is that it works well with small training datasets, which is very important for levee applications as the training data is very small. While training an SVM to give better accuracies, a number of factors need to be considered including: a) preprocessing the data; b) type of kernel; and c) setting the parameters of the SVM and the kernel. The kernel function plays a critical role in SVM training and classification. The other parameters considered are called hyper parameters and these are the soft margin constant 'C' and the width of the Gaussian kernel $\gamma = 1/(2\sigma^2)$.

The UAVSAR imagery acquired on 16 June 2009 was used in the analysis. Each pixel of multi-look UAVSAR imagery is 5.5 m x 5.5 m, and the size of the subset is 1.1 km along the levee (164 x 94 pixels), which had three reported slide events at the time of image acquisition. As shown in Figure 6.16 the levee is divided into two classes, healthy levee and slump slide, and the training masks were designed based on the ground truth data. This subset has a total of 102 slump slide pixels and 549 healthy levee pixels.

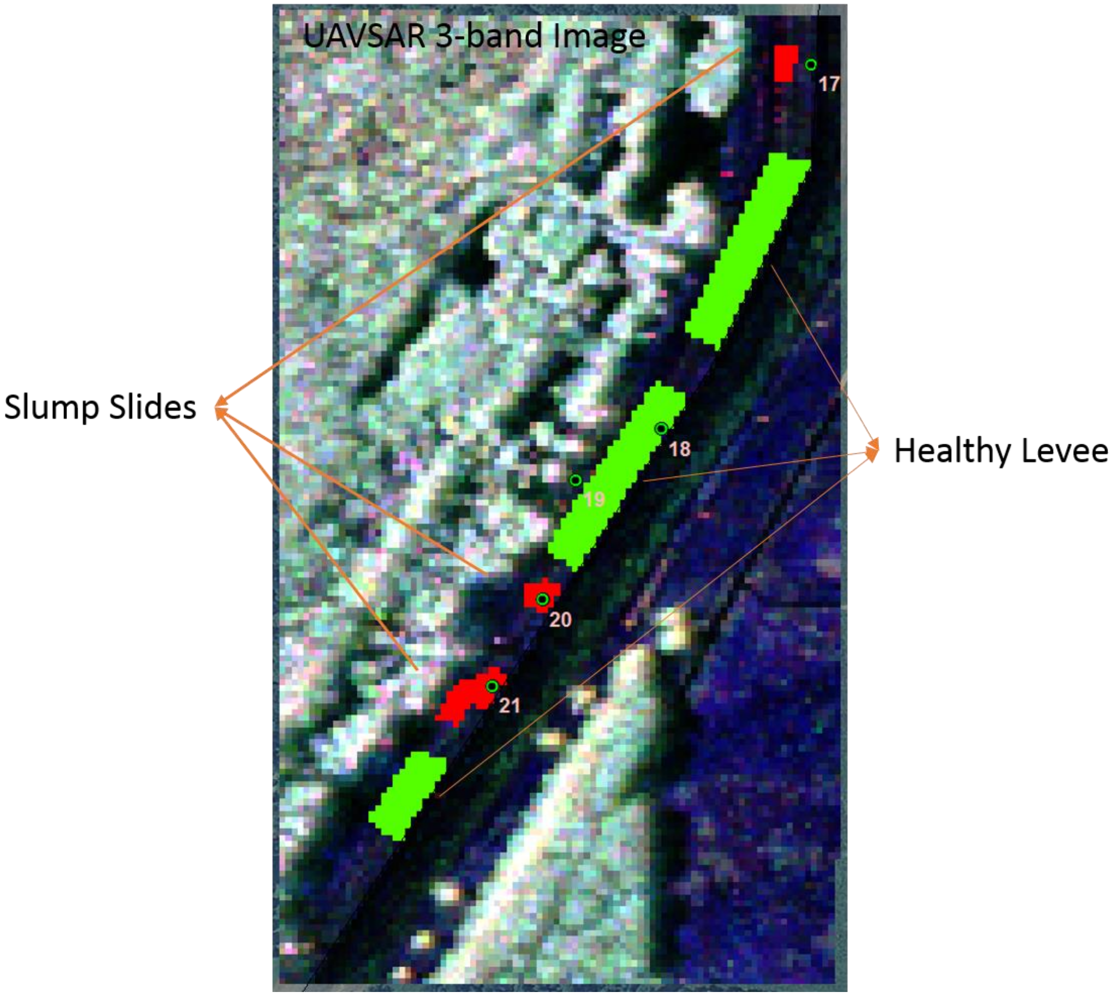

Figure 6.16 Training mask for UAVSAR subset with two ground truth classes: 1. Slump slide and 2. Healthy Levee with 3-band UAVSAR (HH, HV, and VV) image at the background.

Wavelet features were extracted with different window (block) sizes: 4, 8, and 16. The Daubechies mother wavelet was used. The SVM algorithm was implemented on the extracted texture features of the SAR dataset using a Gaussian radial basis function (RBF) kernel and the performance of the classification was tested with different values of the kernel parameter σ. Figure 6.17 shows the overall classification accuracies of the SVM classifier with varying sigma parameter for the RBF kernel and different window size values. This is a two-class problem with uneven pixel counts in these two classes; the slump slide class has less pixels than the healthy levee class. In this case, 10% of the labeled samples were used as training and the rest of the pixels were predicted by the classifier. The results showed that the SVM classifier performed well with DWT window size 8 x 8 with the highest accuracies of 94.5% for the slide class and 95.6% for the healthy levee class. The performance of the classifier was also compared by using only the three radar polarization channel data, HH, HV, and VV (without wavelet features), which resulted in lower classification accuracies. The accuracy assessment was conducted five times, and the experimental results were averaged. The confusion matrix with $\sigma = 0.08$ and wavelet block size B = 8 is given in Table 6.3, and the classification map with $\sigma = 0.08$ and B = 8 is shown in Figure 6.18.

The classifier performance was also estimated with different sets of training samples and the results are tabulated. Figure 6.19 and Figure 6.20 show the accuracies of the classifier when 5% and 30% of the labeled samples were used to train the classifier. The accuracies of slide and healthy classes are 91.7% and 95.1%, respectively, when 5% of the labeled samples were used to train the classifier, and with 30% of the labeled training samples, the highest accuracies achieved were 95.8% and 98.6% with DWT window size 8 and $\sigma = 0.08$. The results showed that the classifier performed better with higher number of labeled samples used to train the classifier.

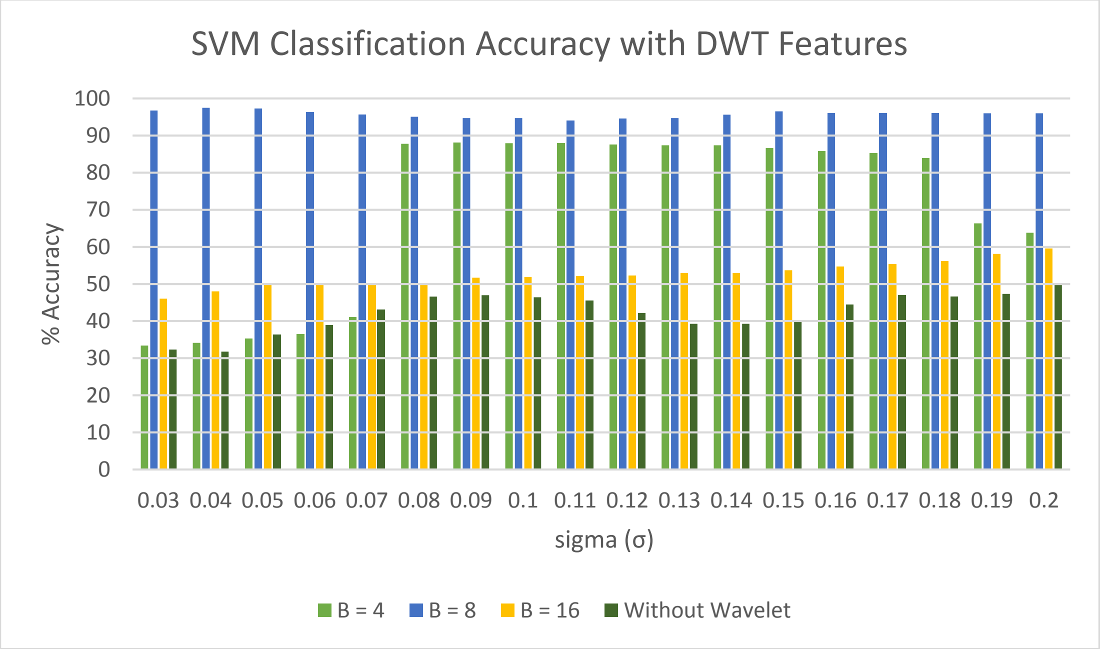

Figure 6.17 Classification accuracy (%) of SVM classifier with DWT features and with different block / window size (B).

10% of the labeled samples were used to train the classifier and Daubechies mother wavelet with one decomposition level was used.

Table 6.3 Confusion Matrix of SVM Classifier output for UAVSAR dataset with σ = 0.08 and wavelet block size B = 8. PA is Producer's Accuracy; UA is User's Accuracy

| | Slump Slide | Healthy Levee | PA |
|---|---|---|---|
| Slump Slide | 87 | 4 | 95.6 |
| Healthy Levee | 20 | 474 | 95.9 |
| UA | 81.3 | 99.2 | 93.0 |

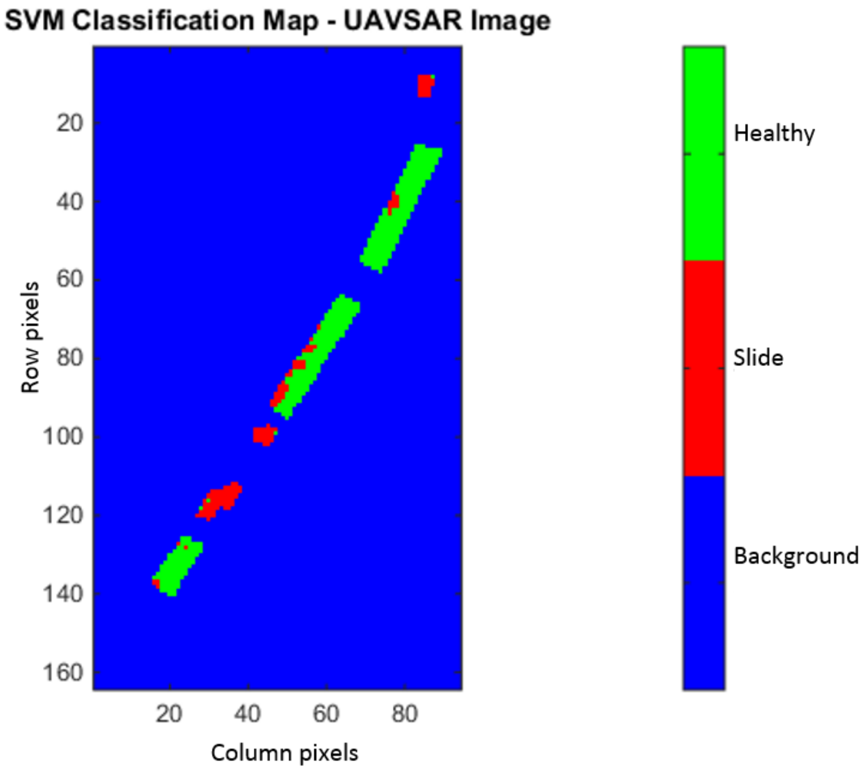

Figure 6.18 SVM Classification map for UAVSAR dataset with σ = 0.08 and wavelet block size B = 8

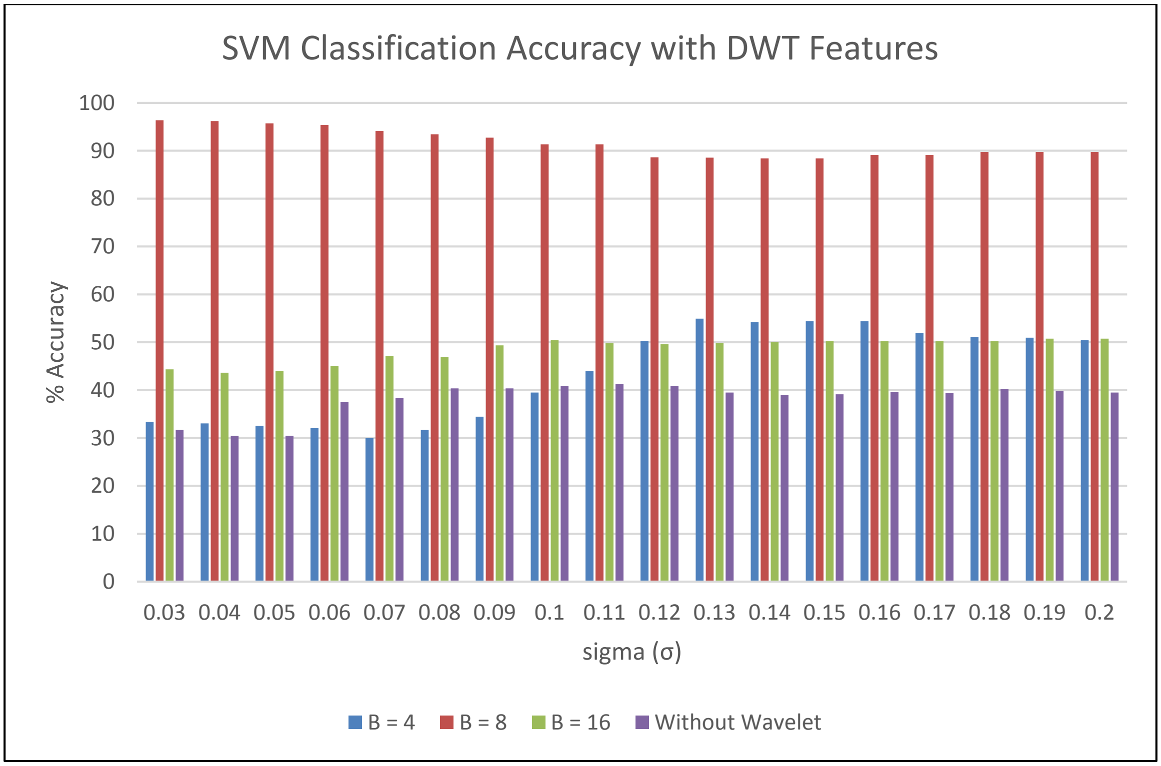

Figure 6.19 Classification accuracy (%) of SVM classifier with 5% of the labeled samples used to train the classifier.

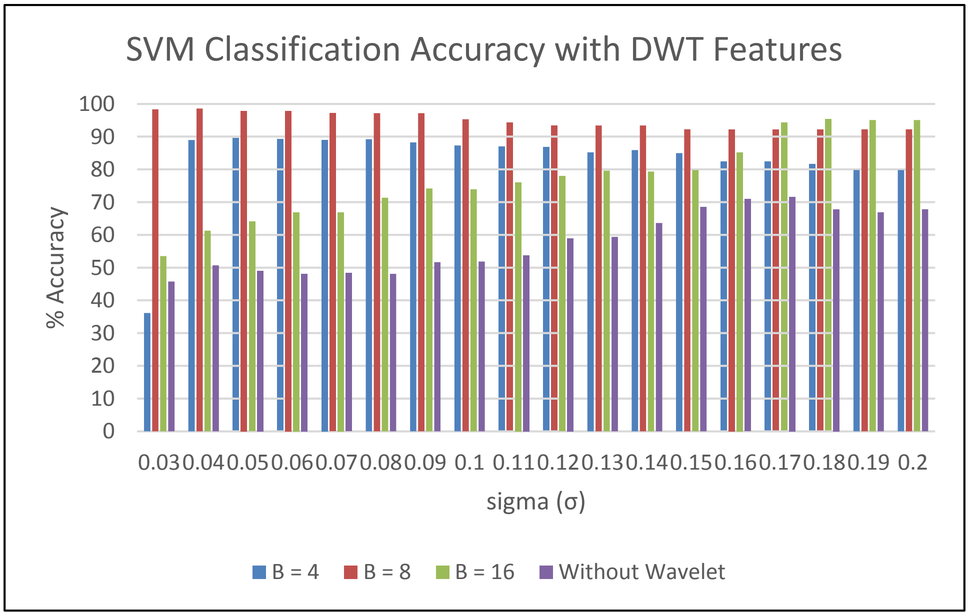

Figure 6.20 Classification accuracy (%) of SVM classifier with DWT features and with different block / window size (B). 30% of the labeled samples were used to train the classifier.

### 6.2.2 Performance comparison of k-Nearest Neighbor (k-NN) and Support Vector Machine (SVM) classifiers with GLCM and DWT features for UAVSAR 4-class subset

In this study, the subset which was used in the previous analysis was used with a different set of ground truth classes. Four classes were considered in this analysis based on the ground truth information and these classes were labeled as: slump slide, healthy levee, stressed vegetation, and the levee road. The UAVSAR subset and the ground truth mask are shown in Figure 6.21 (a) and (b), respectively. Vegetation type and growth rate differences were observed during the field visits between cracked surfaces and stable soil segments on earthen levees in the lower Mississippi River valley. Therefore the stressed vegetation growing over unstable levee segments was taken as a labeled class in this subset. Each pixel of multi-look UAVSAR imagery is 5.5 m x 5.5 m and the size of the subset is 1.1 km along the levee (164 x 94 pixels) which had three reported slide events at the time of image acquisition. The number of pixels in each of these classes are: 76 slide pixels, 86 healthy levee pixels, 58 stressed vegetation pixels, and 43 levee road pixels. DWT and GLCM texture features were extracted and applied to SVM classifier as well as k-NN classifier. The classifiers were trained with 30% and 50% of the randomly selected labeled samples. The accuracy assessment was conducted ten times, and the experimental results were averaged.

The results showed that both k-NN and SVM classifiers performed well with GLCM features. The classifier performance with GLCM features outperformed DWT features when fewer labeled samples (30%) were used to train the classifier. Between both the classifiers, the SVM outperformed the k-NN by attaining highest classification accuracies. With DWT features, the k-NN classifier gave overall accuracy of 62%

whereas the GLCM features outperformed with an accuracy of 82% by using 30% of the labeled samples. The SVM classifier gave highest accuracies of 50% and 86.8% with DWT and GLCM features, respectively, when 30% of the labeled samples were used to train the classifier. Therefore for levee applications, where training data is usually small in number, the SVM classification with GLCM features gives the best performance in identifying various objects on the levee.

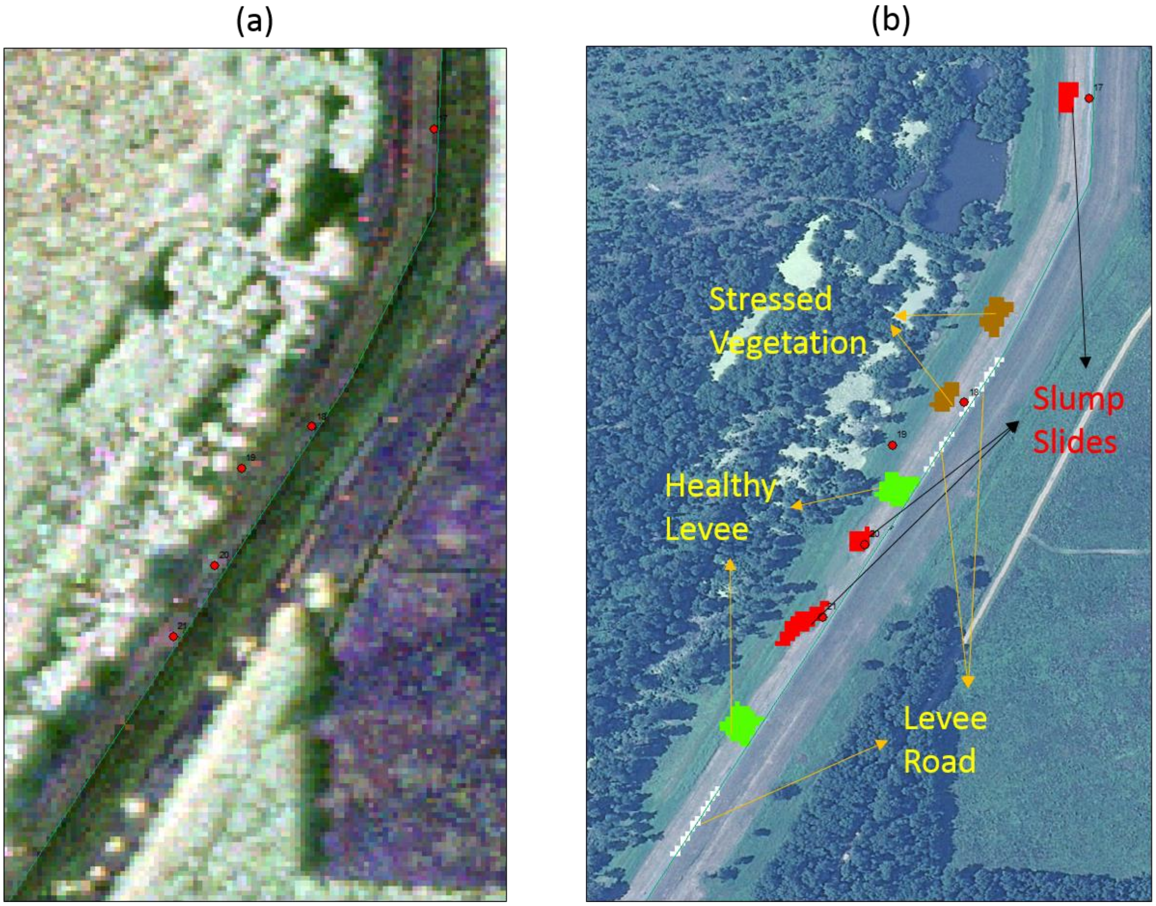

Figure 6.21 (a) UAVSAR 3-band (HH, HV, and VV) color composite of the study area (b) Training mask with four ground truth classes

#### 6.2.2.1 *k*-NN Classification with DWT features

*k*-NN is one of the simplest but most widely used machine learning algorithms. The *k*-NN algorithm classifies $\boldsymbol{x_o}$ by assigning it the label most frequently represented among the *k* nearest samples; in other words, a decision is made by examining the labels on the *k* nearest neighbors and taking a vote. We find the set of *k* nearest neighbors in the training set to $x_o$ and then classify $x_o$ as the most frequent class among the *k* neighbors. Euclidean distance was used to compute the distance measure between training sample and the given testing sample. In this research, we test the algorithm with multiple *k* values, and with DWT and GLCM texture features.

The *k*-NN classifier was implemented on a UAVSAR subset with the extracted DWT coefficients. The algorithm was tested with multiple nearest neighbors *k* with $k = 1$, $k = 2$, *and* $k = 3$ and with multiple DWT block sizes. The classifier was also implemented without the texture features i.e. only with HH, HV, and VV polarimetric features. In this case, 30% of the labeled samples were randomly selected as training and the rest as testing. The accuracy assessment has been conducted ten times, and the experimental results were averaged. The classification accuracies chart with different wavelet block sizes and different *k* values is shown in Figure 6.22. The results show that the classifier performed well with DWT block size B = 8, with one nearest neighbor i.e. $k = 1$. The confusion matrix of *k*-NN classifier with DWT features with block size 8, $k = 1$ and trained with 30% of labeled samples is given in Table 6.4, and Table 6.5 shows the confusion matrix of the classifier trained with 50% of labeled samples.

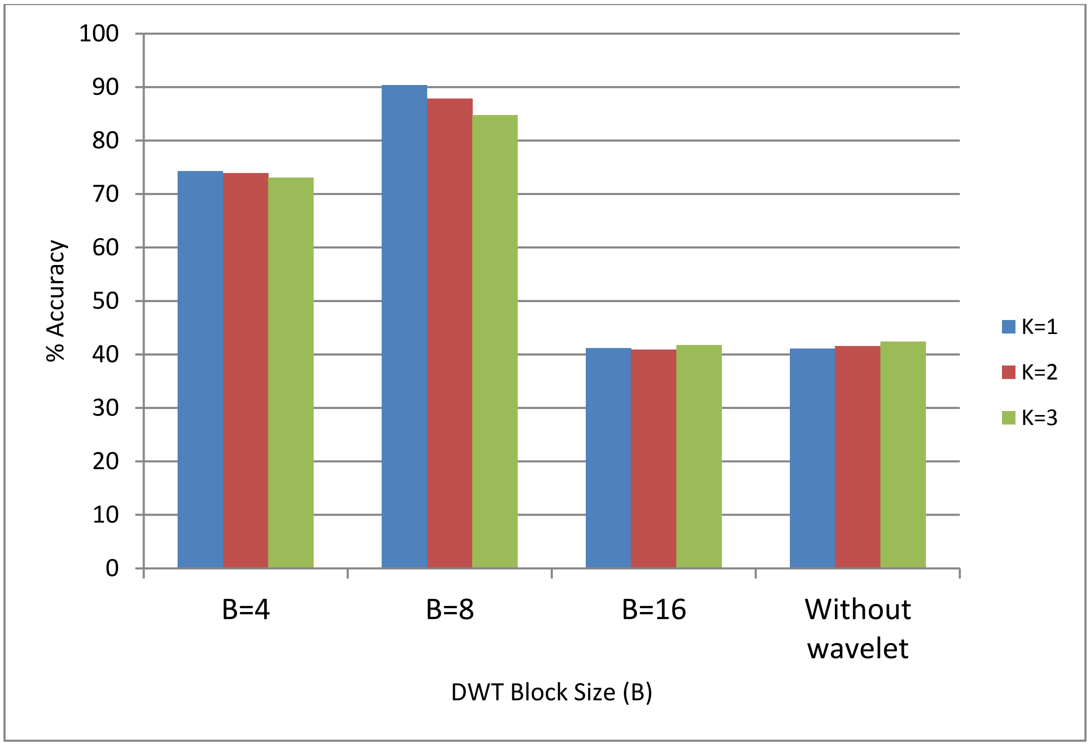

Figure 6.22 Classification accuracy (%) of k-NN classifier with DWT features and with different block size (represented as B) for UAVSAR subset with 50% training samples.

Daubechies mother wavelet with one decomposition level was used.

Table 6.4 Confusion Matrix of k-NN classifier output with DWT features, Block Size = 8, k = 1 with 30% training and 70% testing samples

| | Slump Slide | Healthy Levee | Stressed Vegetation | Levee Road | PA |
|---|---|---|---|---|---|
| Slump Slide | 48 | 4 | 0 | 1 | 90.6 |
| Healthy Levee | 1 | 23 | 33 | 3 | 38.3 |
| Stressed Vegetation | 1 | 11 | 28 | 0 | 70.0 |
| Levee Road | 1 | 17 | 0 | 12 | 40.0 |
| UA | 94.1 | 41.8 | 45.9 | 75.0 | 61.9 |

Table 6.5 Confusion Matrix of k-NN classifier output with DWT features - Block Size = 8, k = 1 with 50% training samples

| | Slump Slide | Healthy Levee | Stressed Vegetation | Levee Road | PA |
|---|---|---|---|---|---|
| Slump Slide | 36 | 1 | 1 | 0 | 94.7 |
| Healthy Levee | 2 | 40 | 0 | 1 | 93.0 |
| Stressed Vegetation | 0 | 1 | 26 | 2 | 89.7 |
| Levee Road | 0 | 0 | 1 | 21 | 95.4 |
| UA | 94.7 | 95.2 | 92.8 | 87.5 | 92.9 |

#### 6.2.2.2 SVM classification with DWT features

The classification accuracies for the SVM classifier using DWT features with different wavelet block sizes and with different RBF kernel parameter (represented as sigma) for the UAVSAR subset is shown in Figure 6.23. The results show that the classifier performed well with DWT block size B = 8, with sigma value 0.04. The confusion matrix of SVM classifier with DWT features with block size 8, σ = 0.04 trained with 30% of labeled samples is given in Table 6.6, and Table 6.7 shows the confusion matrix of the classifier trained with 50% of labeled samples.

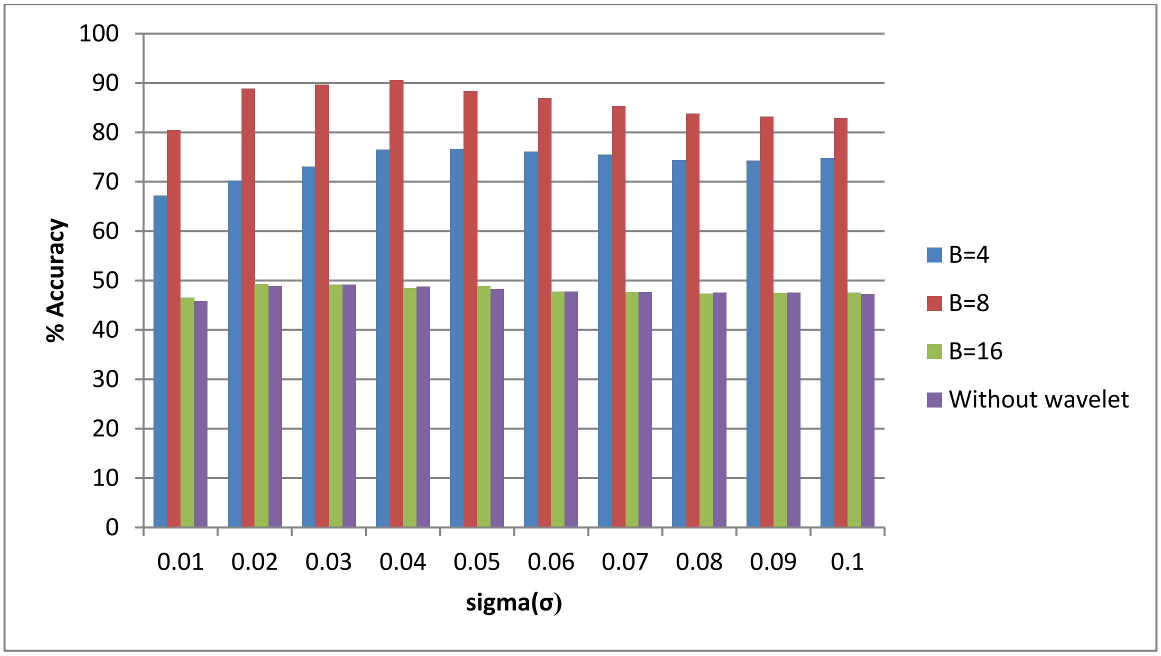

Figure 6.23 Classification accuracy (%) of SVM classifier with DWT features and with different block size (represented as B) as well as RBF kernel parameter (represented as sigma) for UAVSAR subset with 50% training samples.

Daubechies mother wavelet with one decomposition level was used.

Table 6.6 Confusion Matrix of SVM classifier output with DWT features, block Size = 8, σ= 0.04 with 30% training and 70% testing samples

| | Slump Slide | Healthy Levee | Stressed Vegetation | Levee Road | PA |
|---|---|---|---|---|---|
| Slump Slide | 26 | 27 | 0 | 0 | 49.1 |
| Healthy Levee | 11 | 21 | 26 | 2 | 35.0 |
| Stressed Vegetation | 2 | 17 | 19 | 2 | 47.5 |
| Levee Road | 0 | 14 | 0 | 16 | 53.3 |
| UA | 66.7 | 26.6 | 42.2 | 80.0 | 50.0 |

Table 6.7 Confusion Matrix of SVM classifier output with DWT features, block Size = 8, σ= 0.04 with 50% training samples

| | Slump Slide | Healthy Levee | Stressed Vegetation | Levee Road | PA |
|---|---|---|---|---|---|
| Slump Slide | 38 | 0 | 0 | 0 | 100.0 |
| Healthy Levee | 2 | 37 | 1 | 2 | 88.1 |
| Stressed Vegetation | 0 | 0 | 29 | 0 | 100.0 |
| Levee Road | 0 | 5 | 0 | 17 | 77.3 |
| UA | 95.0 | 88.1 | 96.7 | 89.5 | 91.8 |

#### 6.2.2.3 *k*-NN classification with GLCM features

The GLCM features are extracted from four spatial orientations: horizontal, left diagonal, vertical, and right diagonal corresponding to 0°, 45°, 90°, and 135°, and six features have been computed on each matrix. The features computed in this study are: energy, correlation, variance, homogeneity, entropy, and inertia. Experiments were conducted with different block size windows (5x5, 7x7, 9x9, 11x11, and 13x13), and the *k*-NN classifier was trained and tested with this extracted feature data. The performance has been evaluated with multiple *k* values. With DWT features, the classes healthy levee and stressed vegetation were confused, and about half of the healthy levee pixels were classified as stressed vegetation pixels and vice versa, when the classifier was trained with 30% of labeled samples. Also, the road pixels were classified as healthy levee pixels. However, with GLCM features, the classifier performed very well by distinguishing the classes properly. When the classifier trained with 50% of labeled samples, it performed fairly well with a highest accuracy of 90% (Figure 6.24). The confusion matrix of *k*NN classifier output with GLCM features, trained with 30% of labeled samples is given in Table 6.8.

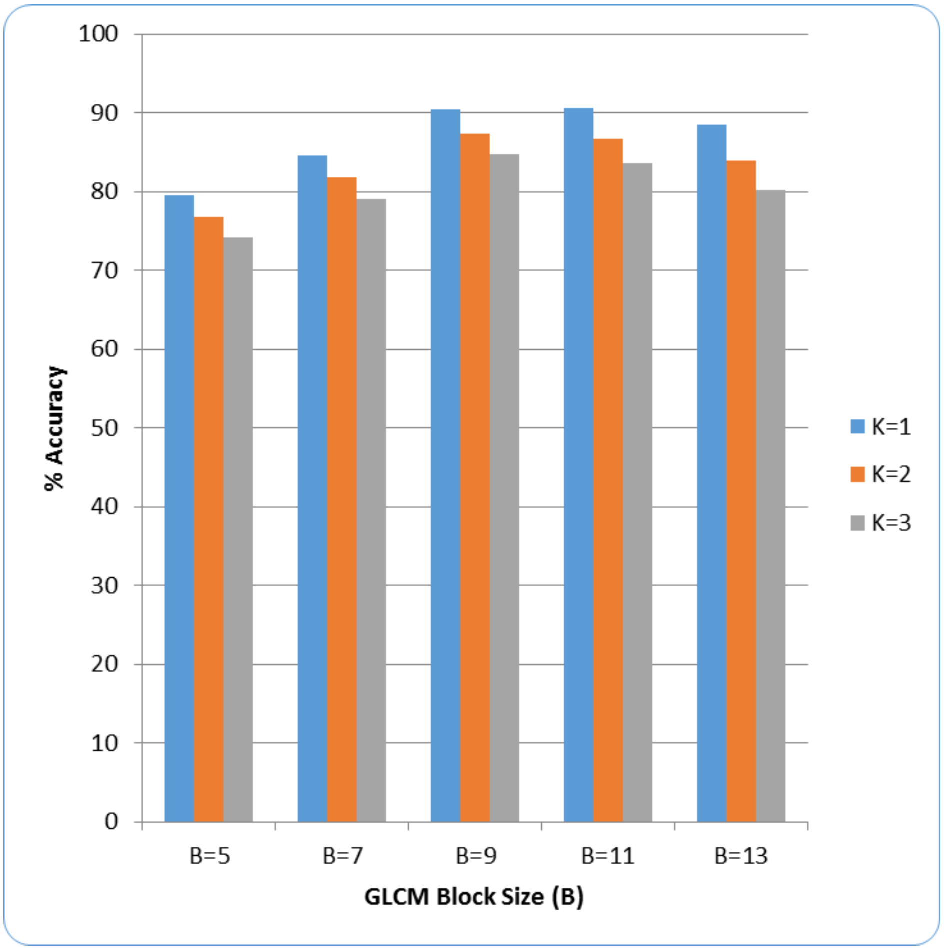

Figure 6.24 Classification accuracy (%) of k-NN classifier with GLCM features for UAVSAR subset for different block sizes and with 50% training samples

Table 6.8 Confusion Matrix of k-NN classifier output with GLCM features, Block Size = 11, k=1 with 30% training and 70% testing samples

| | Slump Slide | Healthy Levee | Stressed Vegetation | Levee Road | PA |
|---|---|---|---|---|---|
| Slump Slide | 40 | 8 | 6 | 0 | 74.1 |
| Healthy Levee | 7 | 53 | 1 | 0 | 86.9 |
| Stressed Vegetation | 2 | 1 | 35 | 3 | 85.4 |
| Levee Road | 1 | 0 | 5 | 25 | 80.6 |
| UA | 80.0 | 85.5 | 74.5 | 89.3 | 82.0 |

#### 6.2.2.4 SVM classification with GLCM features

The GLCM features are extracted from four spatial orientations: horizontal, left diagonal, vertical, and right diagonal corresponding to (0°, 45°, 90°, and 135°) and six features have been computed on each matrix. The features computed in this study are: energy, correlation, variance, homogeneity, entropy, and inertia. Experiments were conducted with different block size windows (5x5, 7x7, 9x9, 11x11, and 13x13), and the SVM classifier was trained and tested with this extracted feature data, and the performance has been evaluated. With DWT features, and 30% of the labeled sample data for training, the classifier performance was poor in distinguishing various objects / classes on the levee, resulting an overall accuracy of 50%. However, with GLCM features, and 30% training data, the classifier performed well and attained an overall accuracy of 86.8% (Table 6.9). When the classifier was trained with 50% of labeled samples, the accuracies obtained with GLCM features (Table 6.10) are the same as the accuracies obtained with DWT features. Figure 6.25 shows the classification accuracy of SVM classifier with GLCM features.

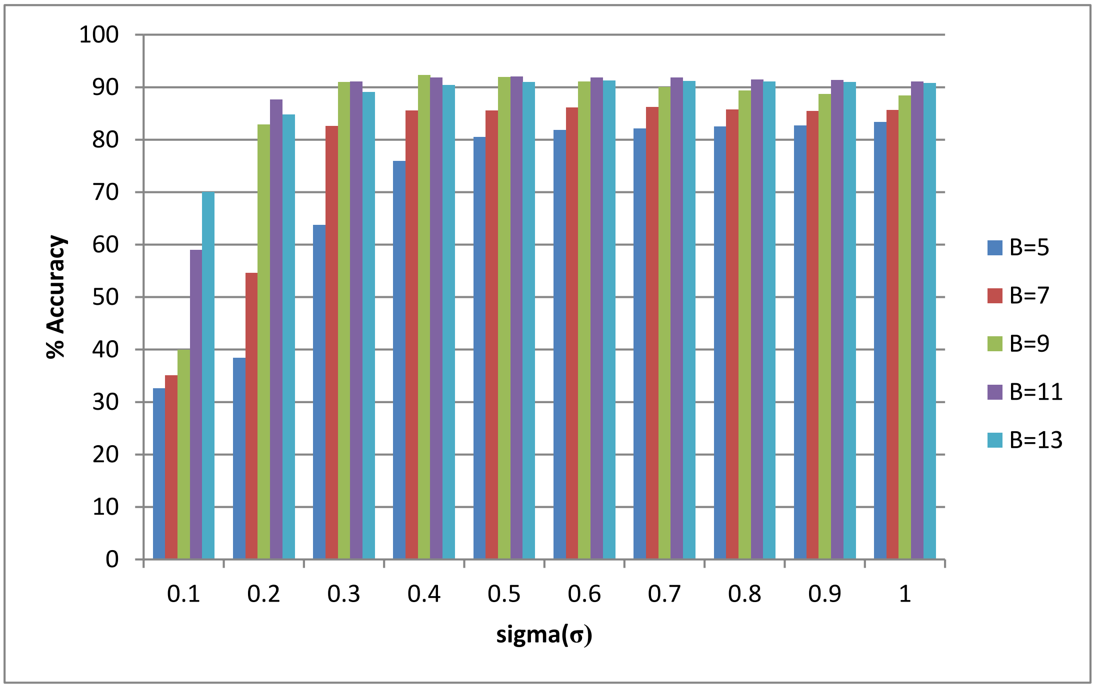

Figure 6.25 Classification accuracy (%) of SVM classifier with GLCM features for UAVSAR Subset for different block size and with 50% training samples

Table 6.9 Confusion Matrix of SVM classifier output with GLCM features, Block Size = 11, σ= 0.5 with 30% training samples

| | Slump Slide | Healthy Levee | Stressed Vegetation | Levee Road | PA |
|---|---|---|---|---|---|
| Slump Slide | 47 | 3 | 4 | 1 | 85.4 |
| Healthy Levee | 3 | 57 | 1 | 0 | 93.4 |
| Stressed Vegetation | 5 | 0 | 35 | 1 | 85.4 |
| Levee Road | 2 | 1 | 3 | 25 | 80.6 |
| UA | 82.5 | 93.4 | 81.4 | 92.6 | 86.8 |

Table 6.10 Confusion Matrix of SVM classifier output with GLCM features, Block Size = 11, σ= 0.5 with 50% training samples

| | Slump Slide | Healthy Levee | Stressed Vegetation | Levee Road | PA |
|---|---|---|---|---|---|
| Slump Slide | 35 | 2 | 1 | 0 | 92.1 |
| Healthy Levee | 1 | 41 | 1 | 0 | 95.3 |
| Stressed Vegetation | 2 | 0 | 25 | 2 | 86.2 |
| Levee Road | 1 | 0 | 1 | 21 | 91.3 |
| UA | 89.7 | 95.3 | 89.3 | 91.3 | 91.3 |

### 6.2.3 SVM Classification with L-band and X-band SAR data

This study uses the UAVSAR multi-polarized (HH, HV and VV), multi-look radar image acquired on 25th January 2010 and the TerraSAR-X dual polarization data (HH and VV) acquired on 15th September 2010 (unfortunately, closer acquisition dates were not available). The spatial resolutions for UAVSAR and TerraSAR-X imagery are 5.5 m and 1 m, respectively. At the time of image acquisition there was one active slump slide (Slide 25) located at (32.5685, -91.0393) north of Vicksburg, Mississippi. A subset of the study area which has this active slump slide was chosen as the area of analysis. Based on the ground truth data collected by US Army Corp. of Engineers (USACE), the training masks were created and utilized in the classification tasks, which is shown in Figure 6.26. The method first calculates the Discrete Wavelet Transform (DWT) of every pixel vector of L-band and X-band SAR imagery.

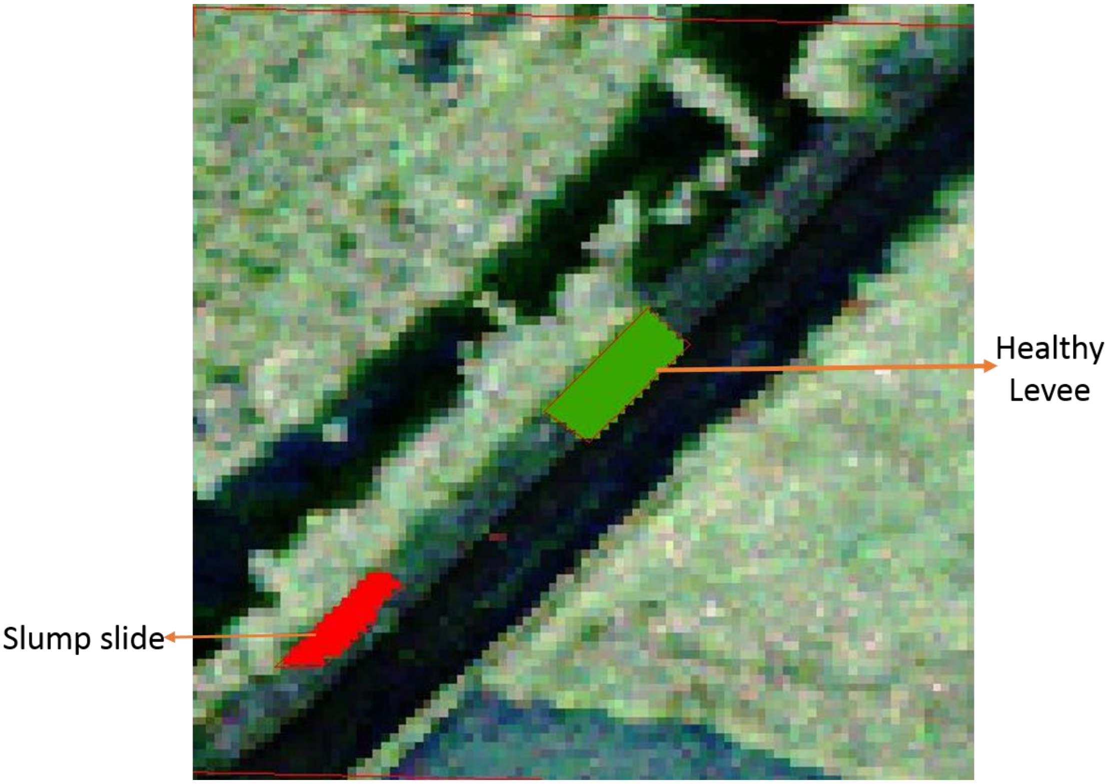

Figure 6.26 Training mask with two ground truth classes: 1. Slump slide, and 2. Healthy Levee

### 6.2.4 SVM Classification with L-band UAVSAR data

Each pixel of multi-look, multi-polarized UAVSAR imagery is 5.5m X 5.5m and the size of the subset is 98 x 94 pixels, out of which 58 are slump slide pixels and 121 are healthy levee pixels. For this subset, 30% of the labeled samples were randomly selected as training, and the rest as testing. The SVM classification algorithm was implemented on the extracted DWT texture features of the subset with a window size of 4. The results show that the SVM classifier performed well with a highest accuracy of 70% for slide detection and 82.6% for healthy levee at $\sigma = 0.2$. The classification accuracies for the UAVSAR subset with multiple $\sigma$ values are shown in Figure 6.27.

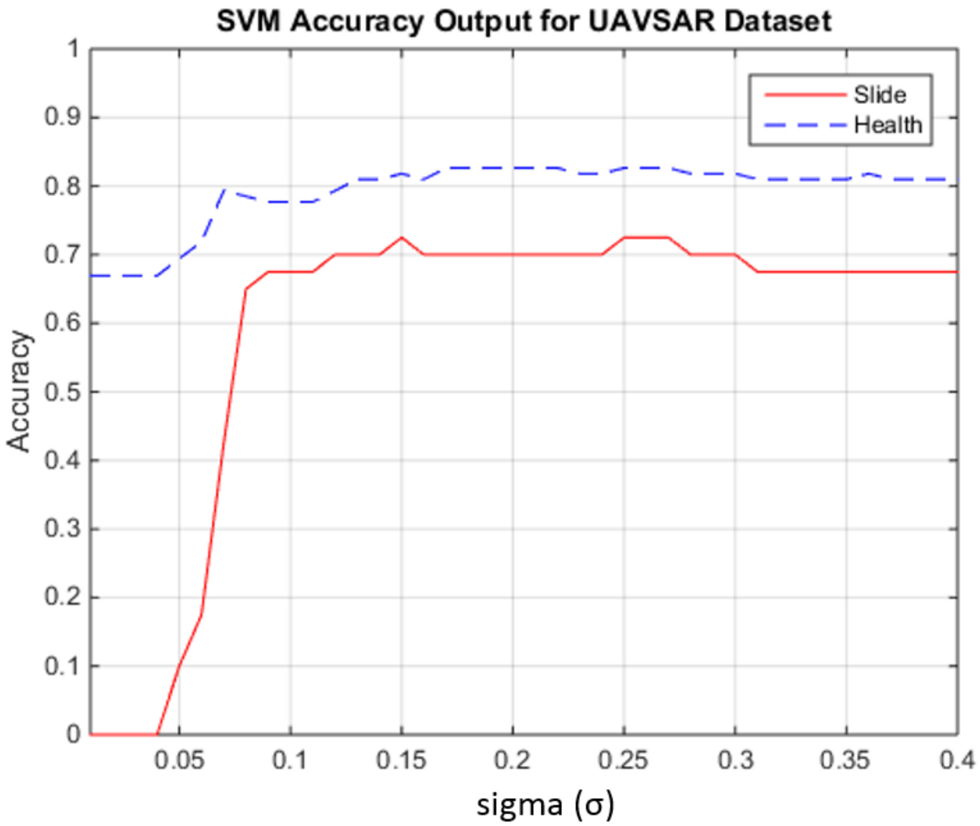

Figure 6.27 SVM tuning for UAVSAR dataset of 25 January, 2010. Relationship between classification accuracy and σ with a constant regularization parameter log C = 4.

### 6.2.5 SVM Classification with X-band TerraSAR-X data

Each pixel of dual-polarized TerraSAR-X imagery is 1m X 1m and the size of the subset is 500 x 562 pixels, out of which, 1984 are slump slide pixels and 3630 are healthy levee pixels. For this subset, 30% of the labeled samples were randomly selected as training and the rest as testing. The SVM classification algorithm was implemented and the results show a highest accuracy of 54.6% for slide and 65.9% for healthy levee detection at $\sigma = 0.06$. The classification accuracies for TerraSAR-X image are shown in Figure 6.28.

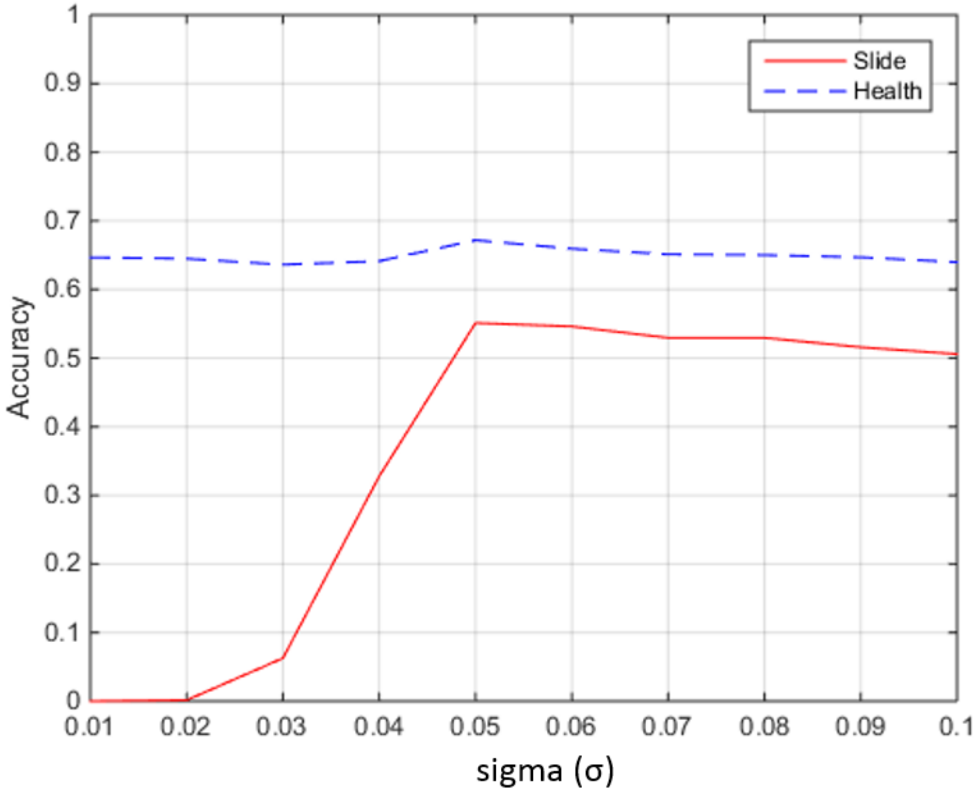

Figure 6.28 SVM tuning for TerraSAR-X dataset of 15 September, 2010. Relationship between classification accuracy and σ with a constant regularization parameter log C = 4.

Experimental results showed that higher accuracies were attained using L-band radar data compared to the X-band data. The slump slides are rough in texture at scales more compatible with the longer L-band wavelength. This factor, and also the greater penetration through vegetation and soil, likely explain the better performance. The performance of the X-band classifier was however still good enough that it should be considered for this application when a suitable L-band sensor is not available or practical.

### 6.2.6 Classification with polarimetric decomposition parameters Entropy (H), Anisotropy (A) and Alpha (H-A-Alpha)

The UAVSAR imagery acquired on 16 June 2009 was used in the analysis. Each pixel of multi-look UAVSAR imagery is 5.5 m x 5.5 m and the size of the subset is 1.1 km along the levee (164 x 94 pixels), which had three reported slide events at the time of image acquisition. Based on the *in situ* data, the slump slides are marked by polygons as shown in Figure 6.29.

From the radar polarimetric backscatter data, the coherency matrix was computed, which contains the second order statistical information about the polarization. The decomposition parameters entropy (H), anisotropy (A) and scattering angle ($\alpha$) are derived from the eigenvalue decomposition of the coherency matrix.

#### 6.2.6.1 Entropy (H)

The parameter entropy (H) indicates the degree of randomness of the scattering medium. The slump slides are usually rough in texture, which will result high entropy values. But the levees in our study area are covered with vegetation (different types of grass-- mostly Bermuda, Rye, Johnson grass and weeds at some areas), so the river side of the levee has moderate to high entropy values. From the entropy map shown in Figure 6.29 (a), it is clear that the slump slides have high entropy values ranging from 0.48 - 0.72.

#### 6.2.6.2 Anisotropy (A)

The anisotropy values are also very high due to vegetation on the levee. The values of anisotropy within the slump slide areas range from 0.95 to 0.98 (Figure 6.29 (b)).

### 6.2.6.3 Scattering Angle (α)

The α angle corresponds to the variation in scattering mechanism, with α = 0° corresponding to surface scattering; α = 45°, dipole scattering; and α = 90°, double bounce scattering. For smooth surfaces, surface scattering dominates and the entropy is close to 0. As shown in Figure 6.29 (c), the alpha values are very high due to double-bounce scattering. The slump slides are rough in texture with certain depth, so these areas resulted in double-bounce scattering. Also, the vegetation on the levee also causes double-bounce scattering, resulting in high values of scattering angles all through the levee. The alpha values within the slump slide range from 89.5° to 89.8° degrees.

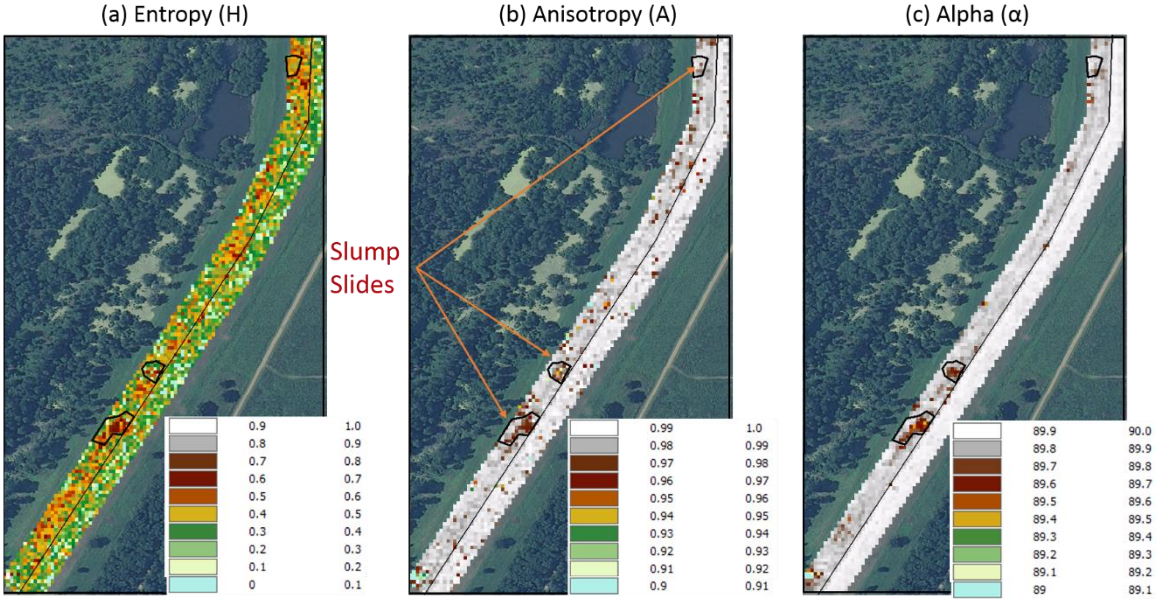

Figure 6.29 Polarimetric features from 16 June 2009 UAVSAR subset. (a) Entropy, (b) Anisotropy, and (c) Scattering angle (α).

### 6.2.7 Classification with H-A-Alpha polarimetric decomposition features

The Support Vector Machine (SVM) and Maximum Likelihood Classifiers (MLC) were implemented based on the polarimetric target decomposition parameters entropy (H), anisotropy (A), and scattering angle (α) derived from the eigenvalue decomposition of the coherency matrix. The training mask for these classifiers is shown in Figure 6.30. This subset has a total of 102 slump slide pixels and 549 healthy levee pixels.

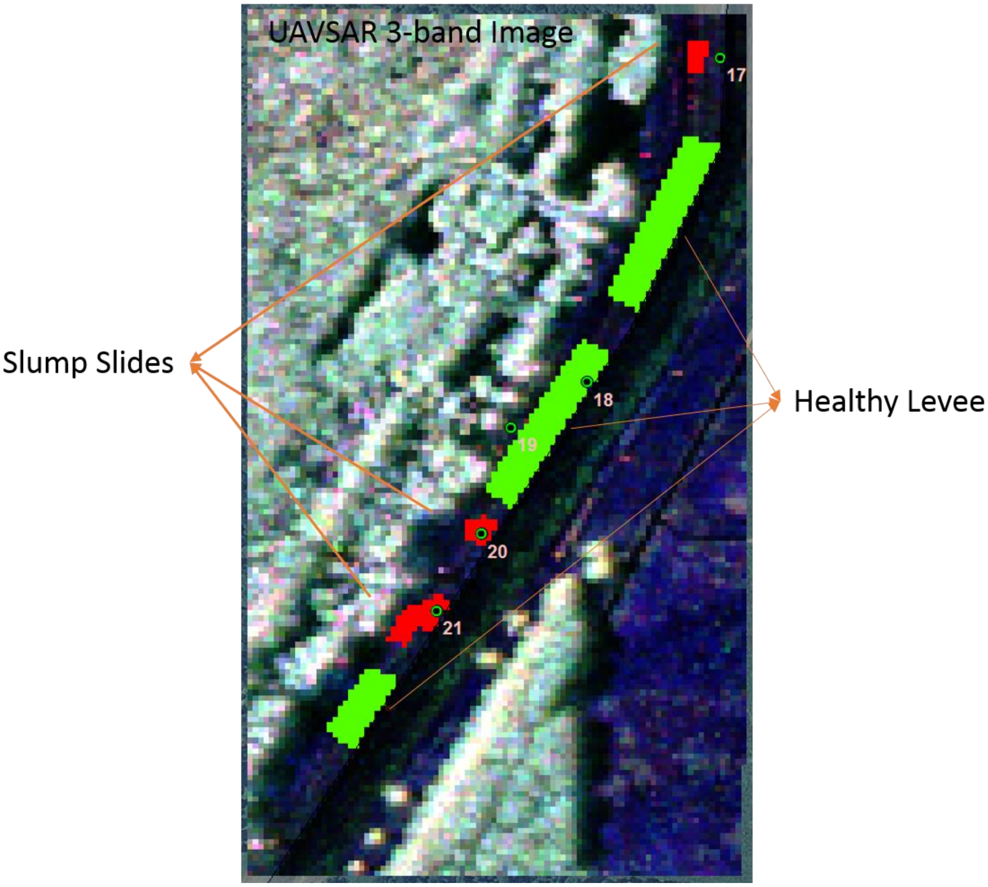

Figure 6.30 Training mask for UAVSAR subset with two ground truth classes: 1. Slump slide and 2. Healthy Levee with 3-band UAVSAR (HH, HV, and VV) image at the background.

The polarimetric decomposition features H, A, and Alpha were applied to a maximum likelihood classifier (MLC) with leave-one-out cross validation technique. There are more "healthy levee" pixels than the "slump slide" pixels in this subset, and the classifier predicted the healthy levee pixels with a highest accuracy of 95% but performed poorly in identifying the slump slide pixels with an accuracy of 47% as given in Table 6.11. The classifiers were trained with 30% of the labeled data. The SVM classifier performed better than MLC with slump slide and healthy levee accuracies of 64% and 85% at σ = 0.35 as shown in Figure 6.31.

Table 6.11 Confusion Matrix of Maximum Likelihood Classifier output for UAVSAR dataset with leave-one-out cross validation. PA is Producer's Accuracy; UA is User's Accuracy

| | Slump Slide | Healthy Levee | PA |
|---|---|---|---|
| Slump Slide | 48 | 54 | 47.1 |
| Healthy Levee | 27 | 522 | 95.1 |
| UA | 64 | 90.6 | 87.6 |

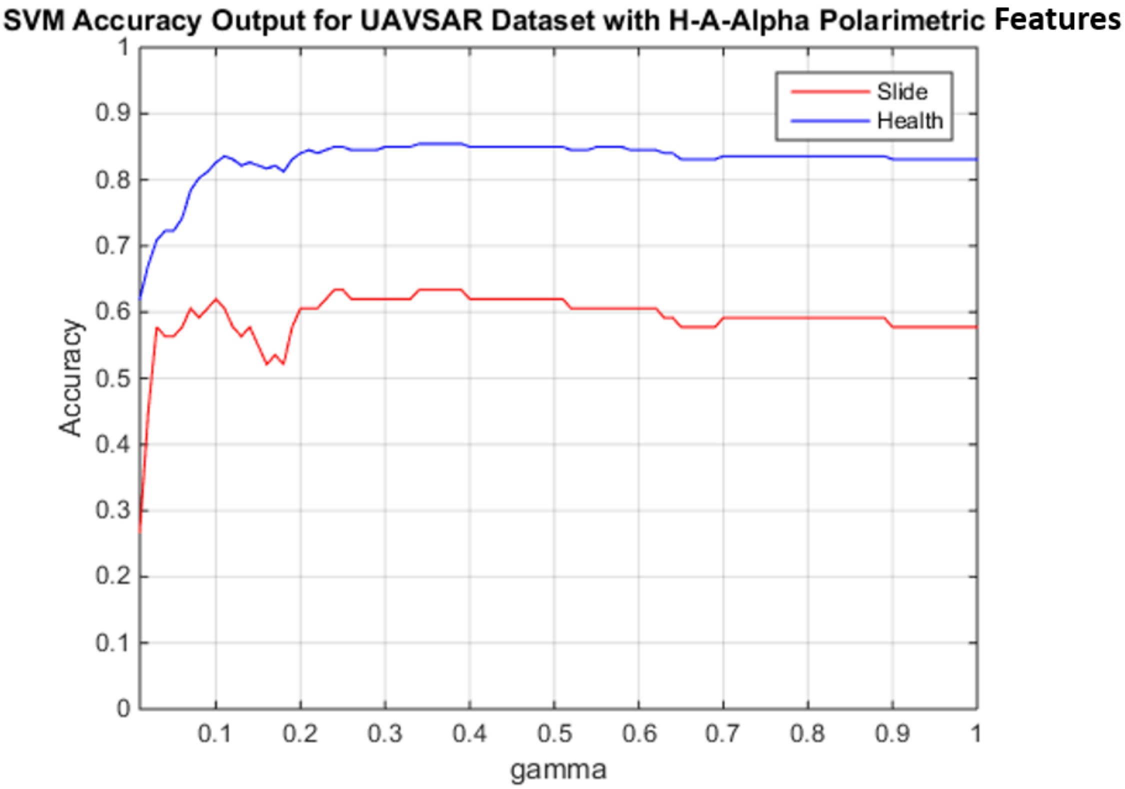

Figure 6.31 SVM classifier accuracies with polarimetric decomposition feature set (H, A, and Alpha) for UAVSAR subset of 16 June 2009.

# CHAPTER VII

# CONCLUSION AND FUTURE WORK

This research developed a machine learning framework for levee slide detection through automated analysis of remotely sensed synthetic aperture radar imagery. SAR data from airborne L-band UAVSAR, and space-based TerraSAR-X X-band sensors were used in this study to detect anomalies on the levee. The important factors that affect the radar backscatter intensity are the radar frequency, polarization, and incidence angle. The results showed that the 3- channel L-band radar performed better than the 2-channel X-band radar. This is most likely due to its ability to penetrate vegetation on the levee and thus provide more information about soil properties. However, the lower availability and higher acquisition costs of L-band radar data are important to consider, and make it useful to consider X-band data. The performance accuracies of target detection showed that X-band data is a good alternative when L-band data is not an option. The constant incidence angle throughout the image swath is an advantage of space-based TerraSAR-X sensor, which minimizes the backscatter variations due to varied incidence angles. The airborne UAVSAR sensor has the limitation of varied incidence angles across the image swath, so the study area with constant levee orientation was analyzed in this work.

Surface roughness is an important property to distinguish slump slides as the radar backscatter is strongly influenced by irregularities on the levee. Polarimetric and textural features were computed and utilized in the classification tasks to achieve efficient levee classification. The polarimetric and texture features extracted in this study are pixel-based and window-based respectively. Per-pixel features include radar backscatter intensity in each of the polarization channels (HH, HV, and VV) and polarimetric decomposition parameters - entropy, anisotropy, and scattering angle. Two types of textural features examined in this study are: DWT, and GLCM features. The classification algorithms were tested with texture features extracted using different window sizes.

Supervised and unsupervised classification algorithms were applied to the SAR data for characterizing vulnerability of levee segments. The supervised algorithms studied in this research are the SVM, kNN, and maximum likelihood classifiers and the unsupervised classifier implemented was the RX anomaly detector algorithm. The RX detector algorithm was able to identify the active slump slides at the time of radar image acquisition. The classification output also consists of some false positives in addition to the true positives, which are slump slides. Based on the slide ground truth data from the Mississippi Levee Board, it was confirmed that some areas which were flagged as “anomalous” in the classifier output became new slump slides at a later date. Other false positives in the output need further investigation to check whether these are vulnerable areas, but such study will require extensive soil measurements. The conclusion is that the unsupervised anomaly detection algorithms are very fast in implementation and do not need ground truth information, so the classifier results can guide levee managers to investigate the areas shown as anomalies in the classification map.

The supervised classifiers were tested with different training sample size and the classification accuracy was evaluated. The support vector machine supervised learning algorithm with GLCM features provided excellent classification accuracies in identifying slump slides on the levee. The results showed that inclusion of textural features derived from the SAR data using DWT and GLCM features improved the overall classification accuracies.

## 7.1 Future Work

A major recommendation for further study is to undertake more extensive testing of the interferometric features to detect small-scale deformations along the levee by using large numbers of repeat pass radar imagery. From the field campaign, we observed that grasses grown over areas with cracks and fractures on the levee are stressed for moisture compared to the grasses grown over healthy areas of the levee. This research can be extended by incorporating multispectral or hyperspectral imagery to the SAR data using data fusion techniques. The radar data can identify the soil properties which can lead to vegetation stress, and fusing the multispectral or hyperspectral data enables the detection of subtle differences in vegetation stress. While implementing the machine learning algorithms to detect anomalies on the levee, some areas on the levee were excluded due to small shrubs on the levee. Incorporating multispectral or hyperspectral data along with radar data would benefit the analysis by not requiring the exclusion of those areas. A majority filter can be applied to the classifier output to remove the outliers and decrease the false positives, thereby improving the classifier performance. Alternate approaches for levee characterization could include object-based or region-based analysis, which might improve the overall accuracies for detecting slump slides.

In this study, the SAR data correction for local incidence angle variation was not considered, so future work is needed for correcting the SAR data for terrain slope and levee orientation variations.